

# **Time resolved Kerr microscopy of materials and devices for magnetic data storage applications**

Submitted by **Wei Yu** to the University of Exeter as a thesis for the degree of  
Doctor of Philosophy in Physics, May 2014.

This thesis is available for Library use on the understanding that it is copyright material and that no quotation from the thesis may be published without proper acknowledgement.

I certify that all material in this thesis which is not my own work has been identified and that no material has previously been submitted and approved for the award of a degree by this or any other University.

A handwritten signature in black ink, appearing to read "Wei Yu". It is written in a cursive style with a horizontal dotted line underneath for placement.



*To all the people I love...*



## Abstract

Time resolved scanning Kerr microscopy (TRSKM) has been used to study a number of different magnetic systems.

Firstly, partially built hard disk writer structures, with a multilayered yoke formed from 4 repeats of a NiFe(~1 nm)/CoFe(50 nm) bilayer, and with three coil windings underneath, were studied by TRSKM with unipolar driving pulses. Dynamic images of the in-plane magnetization suggest an underlying closure domain equilibrium state. This state is found to be modified by application of a bias magnetic field and also during pulse cycling, leading to different magnetization rotation and relaxation behaviour within the tip region. Studies of a further three yokes with the same stack structure, but with only one coil winding at different positions beneath the yoke, yielded dynamic images of “flux beaming” in a channel parallel to the driving field. The magnetic contrast was strongest when the active coil was located near the centre of the yoke, while relaxation after removal of the excitation was most complete when the active coil was located near the confluence region. These results confirm the need for a multi-turn coil to ensure effective flux propagation along the entire length of the yoke. Furthermore, a structure with a NiFe/CoFe/Ru/NiFe/CoFe synthetic antiferromagnetic (SAF) yoke was studied as a bipolar current pulse with 1MHz repetition rate was delivered to the coil. The component of magnetization parallel to the symmetry axis of the yoke was compared at the pole and above a coil winding in the centre of the yoke. The two responses are in phase as the pulse rises, but the pole piece lags the yoke as the pulse falls. The Kerr signal is smaller within the yoke than within the confluence region during pulse cycling. This suggests funneling of flux into the confluence region. Dynamic images

acquired at different time delays showed that the relaxation is faster in the centre of the yoke than in the confluence region, perhaps due to the different magnetic anisotropy in these regions. Although the SAF yoke is designed to support a single domain to aid flux conduction, no obvious flux beaming was observed, suggesting the presence of a more complicated domain structure. The SAF yoke writer hence provides relatively poor flux conduction but good control of rise time compared to single layer and multi-layered yokes studied previously.

Secondly, vortex dynamics within arrays of square ferromagnetic nano-elements have been studied using TRSKM with coherent microwave excitation. It is shown that TRSKM can be used to detect vortex gyration in square nanomagnets with a lateral size (250nm) that is smaller than the diameter (300nm) of the focused laser beam. In an array with large element separation and negligible dipolar interaction, TRSKM images acquired at a fixed point in the microwave cycle reveal differences in the phase of the dynamic response of individual nanomagnets. While some variation in phase can be attributed to dispersion in the size and shape of elements, the circulation and polarization of the vortex are also shown to influence the phase. In an array with element separation smaller than the optical spot size, strong magneto optical response was observed within small clusters of elements. Micromagnetic simulations performed for 2 x 2 arrays of elements show that a certain combination of circulation and polarization values is required to generate the observed magneto-optical contrast.

Thirdly, polar TRSKM has been used to directly observe magnetostatically coupled transverse domain walls (TDWs) in a pair of closely spaced, curved nanowires (NWs). Kerr images of the precessional response revealed a minimum in the Kerr signal due to the TDW in the region of closest NW separation. When the TDWs were ejected from the NW pair, the minimum in the Kerr signal was no longer observed. By imaging this transition, the static decoupling field was estimated to lie between 38 and 48 Oe, in good agreement with a simple micromagnetic model. This work provides a novel technique by which DC and microwave assisted decoupling fields of TDWs may be explored in NW pairs of different width, separation, and curvature.

Fourth, time resolved magneto-optical Kerr effect and phase modulated X-ray ferromagnetic resonance measurements have been performed on a CoO/Py bilayer for different temperatures, RF frequency, and CoO thickness. Kerr hysteresis loops did not show any evidence of exchange bias for temperatures between 200K and 330K for any thickness of CoO, but the coercivity was found to increase with increasing CoO thickness and decreasing temperature. Magneto-optical FMR and XFMR data showed some asymmetry with respect to the sign of the bias field, but the amplitude of the signals decreased rapidly with decreasing temperature. The results are consistent with the appearance of frustrated antiferromagnetic order within the CoO during field cooling.



## Acknowledgement

I had decided to write this part at the very end when I just started writing up this thesis, naively thinking it was probably the easiest part. However, along with some other mistakes I had made, I was wrong again.

The whole thesis is a collaborated work between many people in groups from many institutions, but the first one I would like to say thanks to is of course my supervisor Prof. Rob Hicken who gave me this fantastic opportunity to fulfil my goal and dream. What I learnt from Rob were not only just physics but also a lot of other valuable experience and knowledge in all aspects. Thanks Rob for sending me to Diamond Light Source to experience the word class synchrotron radiation experiments, from where I learnt knowledge which are much more vivid than from text books; Thanks Rob for sending me to visit Brown University in the US to broaden my experience; Thanks Rob for sending me to many international conferences to present my works...

The second I would like to thank is Dr. Paul Keatley, who patiently showed me how to operate the experiments and gave me lots of help while I was struggling in the lab.

Third, I would like to thank our collaborators from Seagate Technology. Particular thanks go to Dr. Peter Czoschke, who gave us many suggestions on the writer heads study and Dr. Mark Gubbins, who supervised me as a summer intern at Seagate in 2013.

I really appreciate the chance that Prof. Gang Xiao offered me to visit Brown University in 2012, and the warm help from his group--Michael, Shutong, Yuanjun and Qiang.

I would also like to thank other members in our group. Thanks Leigh for introducing me to the XFMR experiment at Diamond Light Source before his return, I also enjoyed the time we were driving in Colorado to appreciate the Pikes Peak; Thanks Prim for helping me getting started on my project; Thanks Uday for showing me how to use the office kits and having us for a great traditional dinner at his house; Thanks Shalini for sharing some relaxing time with me in the office when the experiment was stressing me up; Thanks Max for helping me on the grammar of my presentation; Thanks Chris for showing me all the gym techniques and the encouragement he gave me to do the training properly ; Thanks Tom for coding the delay generator into the system in lab G21 to help me increase the delay range as well as his interesting opinions on politics and cultures; Thanks Robert V for the office coffee machine which completed our office and his help on my demonstration while I was away; And thanks Haidar and Reem for exposing another totally different culture to me.

# Contents

Abstract .....	5
Acknowledgement .....	9
List of Publications .....	14
Declaration.....	17
Chapter 1: Introduction .....	19
Chapter 2 Background of Magnetism.....	23
2.1 Introduction .....	23
2.2 Physics units of magnetism.....	23
2.3 Magnetic dipoles in a uniform magnetic field.....	25
2.4 Paramagnetism .....	25
2.5 Magnetic properties of an electron gas .....	26
2.5.1 Review of the quantum mechanics of magnetism.....	26
2.5.2 Spin paramagnetism of electron gas.....	29
2.6 Ferromagnetism .....	31
2.6.1 The classical molecular field theory of ferromagnetism.....	32
2.6.2 Exchange interaction.....	32
2.7 Ferromagnetic materials .....	36
2.8 Magnetic anisotropy .....	36
2.8.1 Magnetocrystalline anisotropy .....	37
2.8.2 Shape anisotropy.....	37
2.9 Domain and domain walls .....	37
2.9.1 The formation of domains.....	38
2.9.2 Domain wall .....	39
2.10 Magnetic Vortex .....	40
2.11 Superparamagnetic limit.....	41
2.12 Magnetic hysteresis loop .....	42
2.13 Stoner-Wohlfarth model.....	44
2.14 Antiferromagnetism and interfacial exchange anisotropy .....	46
2.15 Magnetic Dynamics .....	48
2.15.1 Larmor precession.....	48
2.15.2 Landau-Lifshitz-Gilbert Equation.....	50
2.15.3 Spin Waves .....	51
2.15.4 Ferromagnetic Resonance.....	52

2.16 Spin Transfer Torque and Spin Pumping .....	56
Chapter 3 Experimental Techniques .....	59
3.1 Introduction .....	59
3.2 Magneto-Optical Kerr Effect .....	59
3.2.1 Different Geometries of MOKE .....	59
3.2.2 The Origin of the Magneto-optical Kerr Effect.....	61
3.2.3 A formalism to describe MOKE .....	62
3.2.4 The Detection of MOKE .....	64
3.2.5 Time resolved scanning Kerr microscopy .....	69
3.2.6 Time resolved low temperature MOKE .....	71
3.3 X-Ray magnetic circular dichroism (XMCD) and X-Ray magnetic linear dichroism (XMLD) measurements .....	73
3.3.1 XMCD .....	74
3.3.2 XMLD.....	74
Chapter 4 Time resolved scanning Kerr microscopy of hard disk writer yokes .....	76
4.1 Introduction .....	76
4.2 Principle of HDD operation.....	77
4.2.1 Writing Physics.....	78
4.2.2 Conduction of the flux .....	80
4.3 Study of the magnetization dynamics within a multi-layered yoke with three coils .....	84
4.4 The effect of the coil positions .....	93
4.5 Bipolar pulse excitation of a synthetic antiferromagnetic yoke .....	99
4.6 Conclusion and future work.....	106
Chapter 5 Observation of vortex dynamics in arrays of nanomagnets .....	107
5.1 Introduction .....	107
5.2 Experiment and sample details.....	109
5.3 Results and discussion .....	111
5.3.1 Static and dynamic measurements of single microscale elements .....	111
5.3.2 Dynamic measurements of arrays .....	115
5.4 Summary .....	128
Chapter 6 Time-resolved Kerr microscopy of coupled transverse domain walls in a pair of curved nanowires .....	129
6.1 Introduction .....	129
6.2 Sample and experimental set-up.....	130
6.3 Results and discussion .....	132

6.4 Conclusion .....	138
Chapter 7 Low temperature time resolved magneto optical Kerr effect study of a wedged CoO/Py bilayer .....	139
7.1 Introduction .....	139
7.2 Experimental set up.....	141
7.3 Results and discussion .....	142
7.4 Conclusion .....	152
7.5 Future works.....	153
Chapter 8 Conclusion .....	154
Appendix 1 Bi-Polar electrical impulse generation.....	157
Reference .....	161

## List of Publications

- 1, **W. Yu**, P. Gangmei, P. S. Keatley, R. J. Hicken, M. A. Gubbins, P. J. Czoschke, and R. Lopusnik, *Time resolved scanning Kerr microscopy of hard disk writer structures with a multilayered yoke*, Appl. Phys. Lett. **102**, 162407 (2013).
- 2, **W. Yu**, P. S. Keatley, R. J. Hicken, M. A. Gubbins, P. J. Czoschke, and R. Lopusnik, *Effect of coil position on magnetization dynamics of multilayered hard disk writer yokes*, IEEE Trans. Magn. **49**, 3741 (2013).
- 3, **W. Yu**, P. S Keatley, R. J. Hicken, M. A. Gubbins, P. J. Czoschke and R. Lopusnik, *Time resolved imaging of magnetization dynamics in hard disk writer yokes excited by bipolar current pulses*, J. Appl. Phys. **115**, 17B727 (2014).
- 4, P. S. Keatley, **W. Yu**, L. O'Brien, D. E. Read, R. P. Cowburn, and R. J. Hicken, *Time-resolved Kerr microscopy of coupled transverse domain walls in a pair of curved nanowires*, J. Appl. Phys. **115**, 17D507 (2014).
- 5, M. K. Marcham, **W. Yu**, P. S. Keatley, L. R. Shelford, P. Shafer, S. A. Cavill, H. Qing, A. Neudert, J. R. Childress, J. A. Katine, E. Arenholz, N. D. Telling, G. van der Laan and R. J. Hicken, *Influence of a Dy overlayer on the precessional dynamics of a ferromagnetic thin film*, Appl. Phys. Lett. **102**, 062418 (2013).

6, P. Gangmei, P. S. Keatley, **W. Yu**, R. J. Hicken, M. A. Gubbins, P. J. Czoschke, and R. Lopusnik, *Time- and vector-resolved Kerr microscopy of hard disk writers*, Appl. Phys. Lett. **99**, 232503 (2011).

7, M. K. Marcham, L. R. Shelford, S. A. Cavill, P. S. Keatley, **W. Yu**, P. Shafer, A. Neudert, J. R. Childress, J. A. Katine, E. Arenholz, N. D. Telling, G. van der Laan, and R. J. Hicken, *Phase-Resolved X-ray Ferromagnetic Resonance Measurements of Spin pumping in Spin Valve Structures*, Phys. Rev. B **87**, 180403(R) (2013).



## **Declaration**

The work presented in this thesis is the result of the joint effort of many people. Particular contributions to this work by my PhD supervisor, Prof. Rob Hicken, are difficult to describe as they permeate the whole of this thesis. I also would like to thank Dr. P. S. Keatley who contributed significantly in setting up our Kerr microscope.

In chapter 4, the samples studied were fabricated at Recording Heads Operation, Seagate Technology, MN, USA. The TRSKM studies were performed by myself at the University of Exeter. Particular thanks go to Dr. P. Czoschke at Seagate Technology, for his advice and suggestions that influenced the direction of this study. I also wish to thank Dr. M. A. Gubbins who supervised me as a summer intern at R&D, Seagate Technology, NI, UK, in 2013 where I gained a much deeper understanding of my project. All results in this chapter have already been published in Applied Physics Letters (Section 4.3), the IEEE Transactions on Magnetics (Section 4.4) and the Journal of Applied Physics (Section 4.5).

In chapter 5, the results were obtained through collaboration between three different institutions. The sample was fabricated in the laboratory of Dr. J. R. Childress at Hitachi Global Storage Technology. The TRSKM study was carried out at the University of Exeter by myself and Dr. P. Gangmei. The X-ray photo-emission electron microscopy (XPEEM) was performed at Beamline I06 of Diamond Light Source by Dr. S. A. Cavill, Professor G. van der Laan, Dr. M. K. Marcham and Dr. P. S. Keatley from the University of Exeter. The simulations and analysis were performed by Dr P. S. Keatley and myself. The Scanning

electron microscopy (SEM) was carried out at the University of Exeter by Mr. T. Loughran.

In chapter 6, the sample was fabricated by Dr. L. O'Brien at the University of Cambridge. The TRSKM study was carried out at the University of Exeter by myself and Dr. P. S. Keatley. The results were recently published in the Journal of Applied Physics, in a paper authored by P.S. Keatley, W. Yu, L. O'Brien, D. Read, R.P. Cowburn, and R.J. Hicken.

In chapter 7, the sample was fabricated in the laboratory of Professor Qiu at the University of California at Berkley. The low temperature MOKE study was carried out by myself at the University of Exeter. XFMR measurements were made by Dr. S. Cavill, Dr. M. K. Marcham, Dr. L. Shelford, and myself at Beamline I06, of the Diamond Light Source.

# Chapter 1: Introduction

Since Valdemar Poulsen first demonstrated a recorded signal from a magnetic wire around a drum<sup>1</sup> at Paris Expo. 1900, magnetic recording devices have been advancing with a profound effect upon other industries. For example, with the dawn of the digital era, the bistable nature of a small magnet means that it is also perfectly suited for application in binary calculation devices.

The most important magnetic recording technology today is the magnetic hard disk drive (HDD) that remains the principal type of data storage hardware for most computers and servers. With the need for more portable and smaller sized devices, the magnetic hard disk drive has moved from the original longitudinal magnetic recording (LMR) technique to the perpendicular magnetic recording (PMR) technique in order to increase the recording density (details will be introduced in chapter 4). Since the ability of PMR to increase the recording area density has almost come to an end, an enhanced version of PMR, heat-assisted magnetic recording (HAMR), which makes use of near field focusing of laser light to heat and soften the recording media, is expected to reach the market soon<sup>2</sup>. But, there are still some issues haven't been totally addressed in HAMR design, for example, the dispersed heat from the written bits on the disk would affect other parts of the system such as the reader. Solid state drive (SSD) technology consumes less power, writes and reads faster, and has higher recording density, also threatens to replace the HDD. However, the higher price of SSD means that it remains less competitive compared to HDD for many applications. Besides, the potential benefits of HAMR mean that is still worth understanding and optimizing HDD design since this would give us more knowledge of how to vary the HDD configurations such as writer and reader

designs. Chapter 4 of this thesis will be devoted to studying the magnetization dynamics of HDD writer heads by time resolved scanning magneto-optical Kerr microscopy.

At the same time, non-volatile memory, which requires no power to hold the data, is also in demand in order to increase the battery life of portable devices. Technologies such as magnetic random access memory (MRAM) have been proved to be a successful substitute. Therefore, understanding the magnetization dynamics within micron or sub-micron sized devices is essential to optimize the design. Chapter 5 of this thesis will discuss the dynamics within coupled magnetic vortex arrays. Furthermore, the dynamic dipolar interaction has the potential to phase lock the gyrotropic modes of large numbers of isolated spin transfer torque vortex oscillators (STVOs). Phase-locking, without the need for additional intricate interconnects, has the potential to deliver on-chip RF generators of increased power output.

Logic devices<sup>3</sup> based on magnetic domain wall motion have also been proposed. However, before designing complicated domain wall devices, a thorough understanding of domain wall dynamics is required. For example, the interactions between domain walls have been confirmed,<sup>4,5,6</sup> these interactions can be potentially used to modify domain wall propagations and correct device functions<sup>4</sup>, which is essential for the logic calculation process. In chapter 6 the dynamics of pairs of coupled domain walls will be discussed and their static coupling strength will be measured.

Since many magnetic multilayer devices, such as magnetic tunnel junctions require a pinned or fixed magnetic layer, an antiferromagnetic/ferromagnetic interface is necessary in order to supply exchange bias. Understanding the

exchange bias mechanism in both static and high frequency regimes is very important for device design. In chapter 7, we will present a preliminary study of the magnetization dynamics within the CoO/Py exchange biased system for different CoO thicknesses and different temperatures.



# Chapter 2 Background of Magnetism

## 2.1 Introduction

I will begin by reviewing the basic principles of magnetism relevant to this thesis. Detailed theoretical calculations will not be presented within this chapter. Instead specific extensions of the theory will be discussed within each of the experimental chapters.

## 2.2 Physics units of magnetism

When discussing magnetism, the quantities most commonly encountered are the magnetic field vector  $\mathbf{H}$ , the magnetization vector  $\mathbf{M}$  and sometimes the magnetic induction  $\mathbf{B}$ .

Similar to the Coulomb interaction within electrostatics, when two magnetic poles interact with each other, the force between them can be described by the following functional form:

$$\mathbf{F} = k \frac{m_1 m_2}{r^2} \mathbf{r}^0. \quad (2-1)$$

where  $\mathbf{F}$  is the interaction force between the two poles,  $m_1$  and  $m_2$  are the strength of the two poles,  $r$  is the distance between the two poles,  $\mathbf{r}_0$  is the unit vector between their centres and  $k$  is a constant. The magnetic field generated by  $m_2$  that can be ‘seen’ by  $m_1$  can be described by the following equation:

$$\mathbf{H} = k \frac{m_2}{r^2} \mathbf{r}^0. \quad (2-2)$$

If there were more than one pole, the magnetic field at a particular position would be the vector sum of the contributions from the individual poles. In the

cgs system (centimeter, gram and second), the unit of magnetic field  $\mathbf{H}$  is the Oe (Oersted).

So far, only magnetic dipoles have been observed and atomic theory shows that the magnetic dipole moment arises from two origins: the electron's orbital angular momentum and the electron's spin angular momentum. We use the magnetization vector  $\mathbf{M}$  to define the density of the magnetic moment within magnetic materials.

The magnetic induction vector  $\mathbf{B}$  is defined by the following constitutive equation:

$$\mathbf{B} = \mathbf{H} + 4\pi\mathbf{M}. \quad (2-3)$$

The unit of the magnetic induction in the cgs system is the G (Gauss). When a specimen is subject to a magnetic field,  $\mathbf{B}$ ,  $\mathbf{H}$  and  $\mathbf{M}$  have the following relationships :

$$\mathbf{B} = \tilde{\mu}\mathbf{H}, \quad (2-4)$$

where  $\tilde{\mu}$  is the permeability tensor, and

$$\mathbf{M} = \tilde{\chi}\mathbf{H}, \quad (2-5)$$

where  $\tilde{\chi}$  is the susceptibility tensor.

Another important quantity is the demagnetizing field, which tends to weaken the magnetic field within the specimen:

$$\mathbf{H}_D = -\tilde{N} \cdot \mathbf{M}, \quad (2-6)$$

where  $\tilde{N}$  is the demagnetizing tensor. Therefore, the internal magnetic field of a specimen is:

$$\mathbf{H}_{\text{Int}} = \mathbf{H} - \tilde{\mathbf{N}} \cdot \mathbf{M}. \quad (2-7)$$

### 2.3 Magnetic dipoles in a uniform magnetic field

As in a classical mechanical system, a magnetic dipole  $\mathbf{m}$  in a magnetic field experiences a torque  $\mathbf{L}$  which tries to rotate the magnetic dipole towards the direction parallel to the field. The torque can be defined as

$$\mathbf{L} = \mathbf{m} \times \mathbf{H}. \quad (2-8)$$

### 2.4 Paramagnetism

Although the studies within this PhD project relate to ferromagnetism, it is necessary to first discuss paramagnetism since the classical explanation of ferromagnetism is based on paramagnetism extended by the ‘Weiss molecular field’ theory.

When the susceptibility  $\chi > 0$ , a material is described as being paramagnetic, while for susceptibility  $\chi < 0$ , the material is said to be diamagnetic. From (2-5), we can see that by applying a magnetic field to a paramagnetic material, it will develop a magnetization vector in the same direction as the applied magnetic field. It can be understood that without an external magnetic field, the magnetic moments within the material are randomly oriented, yielding zero net magnetic moment for the whole specimen. After applying an external field  $\mathbf{H}$ , due to the torque  $\mathbf{L}$  from (2-8), the randomly oriented magnetic moments are all rotated towards the direction of the magnetic field. Therefore, the whole specimen becomes magnetized. It is also worth noting that the paramagnetic susceptibility is a function of temperature as described by the Curie law<sup>7</sup>:

$$\chi = \frac{C}{T}, \quad (2-9)$$

where  $C$  is the Curie constant and  $T$  is the absolute temperature.

## 2.5 Magnetic properties of an electron gas

I will briefly introduce a basic description of a paramagnetic electron gas since this will aid the following discussion of ferromagnetism.

### 2.5.1 Review of the quantum mechanics of magnetism<sup>8</sup>

Let us begin by considering an electron moving around the nucleus of a hydrogen atom. The wavefunction of the electron obeys the Schrödinger equation:

$$\left[ -\frac{\hbar^2}{2m} \left( \frac{\partial^2}{\partial x^2} + \frac{\partial^2}{\partial y^2} + \frac{\partial^2}{\partial z^2} \right) + V \right] \psi = E\psi, \quad (2-10)$$

where  $\left[ -\frac{\hbar^2}{2m} \left( \frac{\partial^2}{\partial x^2} + \frac{\partial^2}{\partial y^2} + \frac{\partial^2}{\partial z^2} \right) + V \right] \equiv \mathcal{H}$  is the Hamiltonian in which the  $V$  is the potential energy term and the other term describes the kinetic energy,  $E$  is the energy, and  $\psi$  is the wave function. Different eigenstates of the electron correspond to different solutions of the Schrödinger equation.

For the hydrogen atom, the solutions can be characterized by four quantum numbers, and according to Pauli's principle, only one electron can occupy a particular state defined by a certain combination of those four different quantum numbers. Those four different quantum numbers are the principle quantum number  $n$ , the orbital angular momentum quantum number  $l$ , the magnetic quantum number  $m_l$  and the spin quantum number  $m_s$ .

**Principle quantum  $n$ .** The value of  $n$  corresponds to a particular shell or orbit, and must be integer and nonzero. The K, L, M, N, O, P and Q shells correspond to  $n = 1, 2, 3, 4, 5, 6$  and 7.

**The orbital angular momentum quantum number  $l$ .** For a particular value of  $l$ , the total angular momentum of an electron due to its orbital motion is given by:

$$[l(l+1)]^{\frac{1}{2}}\hbar. \quad (2-11)$$

This quantum number is also an integer and is restricted to the values  $l=0, 1, 2\dots, (n-1)$ . Electrons associated with such values of  $l$  are called  $s, p, d, f$  and  $g$  electrons, respectively.

**The magnetic quantum number  $m_l$ .** This quantum number determines the component of the orbital angular momentum along a specified direction, usually that of an applied magnetic field. This number is also an integer and for a given value of  $l$  may have  $(2l+1)$  possible values:  $m_l = l, (l-1), \dots, 0, \dots, -(l-1), -l$ . This means that the electron's orbital angular momentum can only have certain possible orientations, and is spatially quantized, as shown in figure 2.1.

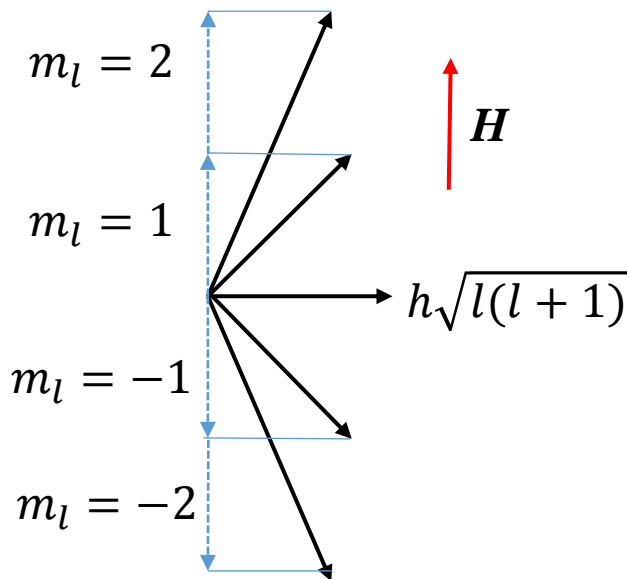


Figure 2.1. Vector model of the orbital angular momentum,  $\mathbf{H}$  is the external magnetic field and  $m_l$  is the magnetic quantum number.

**Spin quantum number  $m_s$ .** The spin is an intrinsic angular momentum of the electron. The quantum number  $m_s$  determines the component of the spin along

the direction of an applied field. The allowed values of  $m_s$  are  $\pm \frac{1}{2}$ , and thus the components of the spin angular momentum in the direction of the applied field are  $\pm \frac{\hbar}{2}$ , where  $\hbar = \frac{h}{2\pi}$  and  $h$  is the Planck constant.

As has been discussed before, the electron's angular momentum is the source of its magnetic moment, the magnetic moment generated by the orbital angular momentum being defined as:

$$|\mu| = \frac{|e|}{2mc} [l(l+1)]^{\frac{1}{2}} \hbar, \quad (2-12)$$

where  $c$  is the speed of the light,  $e$  is the charge of the electron and  $m$  is the mass of the electron. Its projection along the direction of an applied field is

$$\mu_z = \mu_H = \frac{e\hbar}{2mc} m_l. \quad (2-13)$$

The quantity  $\frac{e\hbar}{2mc}$  is known as the Bohr magneton  $\mu_B$ , and has the value  $0.927 \times 10^{-20}$  erg/Oe.

The magnetic moment associated with the spin angular momentum along the field direction is given by the following equation:

$$\mu_{sz} = g \left( \frac{e}{2mc} \right) \frac{\hbar}{2}, \quad (2-14)$$

where  $g$ , the spectroscopic splitting factor or  $g$  factor, is 2.0023 for a free electron.

In a very simple case, for example, when a magnetic field is applied, the energy gap between two opposite spin states is given by:

$$\Delta E = g |\mu_B| H. \quad (2-15)$$

## **Spin-Orbit interaction/Coupling and Hund's Rules**

So far we have addressed the orbital and spin angular momentum separately for a single electron. To obtain the atom's total angular momentum in a multi-electrons system, Hund's Rules are applied:

1, The lowest electronic term has the maximum spin  $S$ .

2, The lowest term has maximum angular momentum  $L$ .

3, The lowest term has the largest total angular momentum  $J$  if the shell is more than half full, and the smallest  $J$  if the shell is less than half full.

Rule 1 and 2 give the total spin and angular momentum respectively. Rule 3 describes the how spin and angular momentum couple. Therefore,  $J = L + S$  for a shell less than half full and  $J = L - S$  for shell more than half full.

### **2.5.2 Spin paramagnetism of electron gas**

Let us consider the case of a monovalent metal in which the conduction electrons, or free electrons, have a relatively high density. The electron gas obeys Fermi-Dirac statics and has distribution  $F(E)$ . The density of states is:

$$C(E) = KE^{\frac{1}{2}}, \quad (2-16)$$

where  $K$  is a constant, and the distribution function is:

$$F(E) = \frac{1}{e^{\frac{E-E_F}{k_B T}+1}} \quad (2-17)$$

where  $E_F$  is the Fermi energy,  $k_B$  is the Boltzmann constant, and  $T$  is the absolute temperature. The form of the Fermi function is shown below:

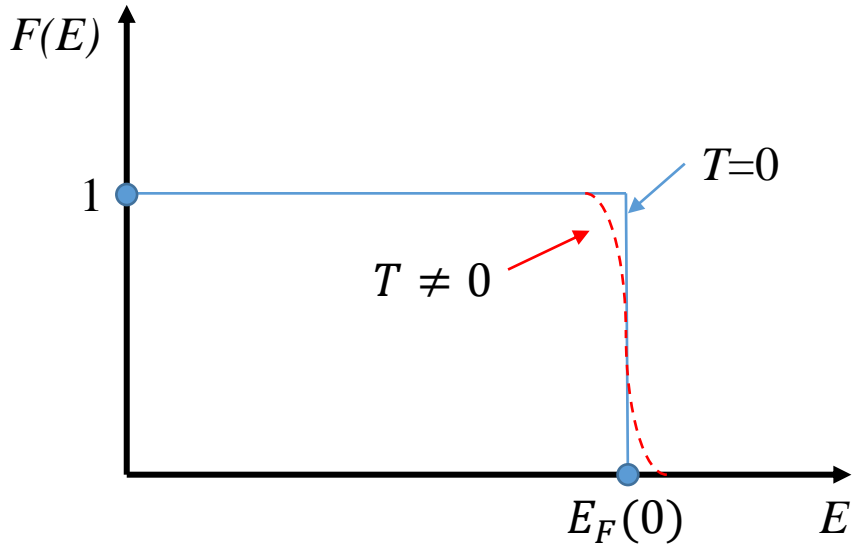


Figure 2.2. The Fermi function at  $T = 0$  K and  $T \neq 0$  K.  $E_F(0)$  is the Fermi energy. As the temperature increases, electrons begin to leave the states below and near  $E_F(0)$  and start to occupy the states above and near  $E_F(0)$ .

It is clearly that at  $T=0$  K,  $F(E)=1$  for  $E < E_F(0)$  and  $F(E)=0$  for  $E > E_F(0)$ . This means that all the states below  $E_F(0)$  are occupied and the ones above  $E_F(0)$  are empty; As the temperature increases, electrons begin to leave the states below and near  $E_F(0)$  and start to occupy the states above and near  $E_F(0)$ . The value of  $E_F(0)$  is the solution of  $F(E) = 0.5$ .

Now let's consider the magnetism that may occur under these circumstances. It is convenient to consider that the electrons are in two sub-systems, one with electrons with a given spin direction and another with electrons with spins in the opposite direction. If at 0 K without any external magnetic field all electrons occupy states below  $E_F(0)$ , so that the states above  $E_F(0)$  are empty, then the net magnetic moment due to spin angular momentum would be zero. However, if a field  $\mathbf{H}$  is applied, the energy of electrons with spin parallel and antiparallel to  $\mathbf{H}$  will become  $E - \mu_B H$  and  $E + \mu_B H$  respectively, where  $E$  is the energy

when  $H=0$ . Since the density of states from (2-14) is parabolic, if the number of electrons within each sub-system were to stay the same, the situation would be that shown in Figure 2.3(a). Obviously this is an unstable state, and the electrons with anti-parallel spin in higher energy states will try to reverse their spin in order to lower the energy of the system, leading to the equilibrium state shown in Figure 2.3(b). Thus, the net magnetic moment of the electron gas becomes non-zero.

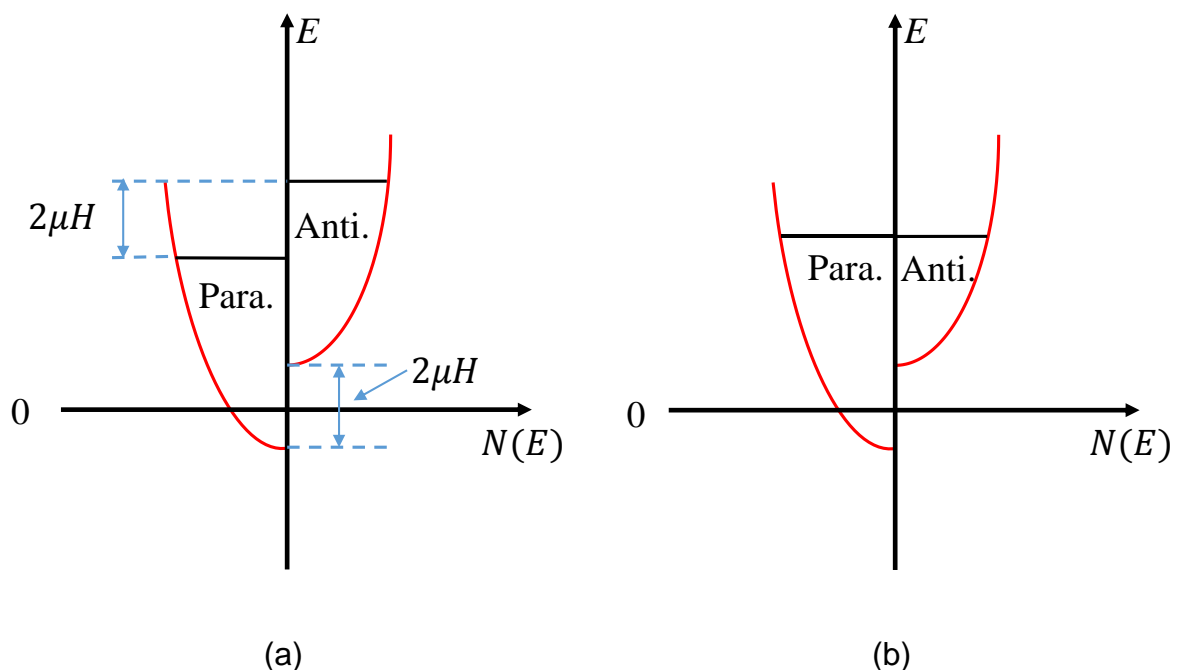


Figure 2.3. Electron spin sub-systems after application of an external magnetic field. Case (a) is unstable while (b) is the stable equilibrium state. Paral. and Anti. denote the spin parallel and antiparallel to the external magnetic field respectively.

## 2.6 Ferromagnetism

As discussed above, it is now clear that firstly, paramagnetic materials have no net magnet moment in the absence of an external field due to equal occupation of the “spin up” and “spin down states”, and secondly, the spin angular momentum is the main contributor of the magnetic moment.

In ferromagnetic materials, a net magnet moment exists even when there is no external magnetic field applied. This means that spin up and down states are not equally occupied, indicating the presence of another internal interaction that acts to align the spins. This spontaneous magnetization disappears above the Curie temperature.

### 2.6.1 The classical molecular field theory of ferromagnetism

The ‘molecular field’ theory was introduced by Weiss<sup>8</sup> before the foundation of quantum mechanics and atomic physics. Molecular field theory assumes the presence of an internal interaction or field inside the ferromagnetic material that aligns the magnetic moments or spins in the same direction. Since thermal agitation of the atoms opposes the orienting effect of this field, the Curie temperature must be the temperature above which the thermal agitation energy is sufficiently large as to destroy the spontaneous magnetization. This assumption allows us to estimate this internal field:

$$\mu_B H_m \approx k_B T_C, \quad (2-18)$$

where  $T_C$  is the Curie temperature. For  $T_C \sim 1000$  K, similar to the Curie temperature of Fe, then:

$$H_m \approx 10^7 \text{ Oe.} \quad (2-19)$$

The origin of this rather large field could not be explained until the foundation of quantum mechanics.

### 2.6.2 Exchange interaction

The molecular field theory phenomenologically explains the spontaneous magnetization within ferromagnetic materials, but it fails to explain the origin of

such a large internal field. Later on, Heisenberg<sup>9</sup> showed that this field is the result of the quantum mechanical exchange interaction. This theory is based on the Heitler-London theory developed for the hydrogen molecule.

Let's consider two electrons moving in similar potentials. The interaction between the electrons is neglected at the beginning and will be considered as perturbation later, the Schrödinger equation is:

$$\left[ -\frac{\hbar^2}{2m} (\nabla_1^2 + \nabla_2^2) + V(q_1) + V(q_2) \right] \psi = E\psi, \quad (2-20)$$

where labels 1 and 2 refer to the two electrons. The possible solutions are:

$$\psi_a(1)\psi_b(2) \text{ and } \psi_a(2)\psi_b(1), \quad (2-21)$$

with  $E = E_a + E_b$  in both cases.  $\psi_a(1)$  is the one-electron wave function when electron 1 is in state  $a$  and is the solution of the one-electron Schrödinger equation:

$$\left[ -\frac{\hbar^2}{2m} \nabla_1^2 + V(q_1) \right] \psi = E_a \psi. \quad (2-22)$$

Similarly  $\psi_b(2)$  is the one-electron wave function when electron 2 is in state  $b$ .

Since the electrons are indistinguishable, it is necessary that:

$$|\psi(1, 2)|^2 dq_1 dq_2 = |\psi(2, 1)|^2 dq_1 dq_2, \quad (2-23)$$

where  $\psi(1, 2)$  is the wave function that describes the two electron system,  $\psi(2, 1)$  is that when the two electrons are interchanged and  $dq_1$  and  $dq_2$  are the differential coordinates. From (2-23) we can see that  $\psi(1, 2) = \pm \psi(2, 1)$ , so the wave function of this two electron system is either symmetric or anti-symmetric with respect to exchange. Neither of the wave functions in (2-21) satisfies this

condition, so they are not acceptable solutions. Therefore, we have to introduce the linear combinations shown below:

$$\psi_{sym}(1, 2) = \frac{1}{\sqrt{2}} [\psi_a(1)\psi_b(2) + \psi_a(2)\psi_b(1)], \quad (2-24)$$

$$\psi_{anti}(1, 2) = \frac{1}{\sqrt{2}} [\psi_a(1)\psi_b(2) - \psi_a(2)\psi_b(1)]. \quad (2-25)$$

These forms now satisfy the symmetry conditions:  $\psi(1, 2) = \pm\psi(2, 1)$ .

From the Pauli Exclusion Principle, an electron state can only be occupied by one electron, so the electron wave function must be anti-symmetric. It is also very important to note that the electron wave function should contain not only the spatial coordinates, but also the spin coordinates. Therefore the one electron wave function can be written as:

$$\psi = \phi(\mathbf{r})\chi, \quad (2-26)$$

where  $\phi(\mathbf{r})$  is the spatial part of the wave function and  $\chi$  is the spin part of the wave function. Since the spin angular momentum parallel to the axis of an external field has only two values  $\pm \frac{\hbar}{2}$ , we can represent the spin wave functions by the following vectors:

$$\chi_\alpha = \begin{pmatrix} 1 \\ 0 \end{pmatrix} \quad (2-27)$$

$$\text{and } \chi_\beta = \begin{pmatrix} 0 \\ 1 \end{pmatrix}. \quad (2-28)$$

The anti-symmetric wave function can be written in the following possible ways:

$$\phi_{sym}(1, 2)\chi_{anti}(1, 2), \quad (2-29)$$

or

$$\phi_{anti}(1,2)\chi_{sym}(1,2). \quad (2-30)$$

From (2-29) and (2-30) we can see that whether the electron spin wave functions are symmetric or anti-symmetric depends upon the symmetry of the spatial wave function  $\phi$ .

Let us now introduce the interaction between the electrons to see how it affects  $\phi$ . The interaction of the two electron system can be described by the Hamiltonian:

$$\mathcal{H}_{12} = \frac{e^2}{r_{ab}} + \frac{e^2}{r_{12}} - \frac{e^2}{r_{1b}} - \frac{e^2}{r_{2a}}, \quad (2-31)$$

where  $r_{ab}$  is the distance between the nuclei,  $r_{12}$  is the distance between electrons and  $r_{1b}$  and  $r_{2a}$  are the distances between a given nucleus and the electron on the other atom. The values of the additional energy introduced by this interaction can be calculated from the equation

$$E = \int \psi^* \mathcal{H}_{12} \psi d\tau, \quad (2-32)$$

so that for the wave function in (2-29) the energy is

$$E_I = A^2(K_{12} + J_{12}), \quad (2-33)$$

while for the wave function in (2-30)

$$E_{II} = B^2(K_{12} - J_{12}), \quad (2-34)$$

where  $A$  and  $B$  are normalizing factors,

$$K_{12} = \int \phi_a^*(1) \phi_b^*(2) \mathcal{H}_{12} \phi_a(1) \phi_b(2) d\tau_1 d\tau_2, \quad (2-35)$$

is the average Coulomb interaction energy, and

$$J_{12} = \int \phi_a^*(1) \phi_b^*(2) \mathcal{H}_{12} \phi_a(2) \phi_b(1) d\tau_1 d\tau_2, \quad (2-36)$$

is called the exchange integral and occurs due to the indistinguishability of the electrons. Since the system tends to occupy the state of lower energy, ferromagnetism occurs when a positive value of  $J_{12}$  is obtained. The relationship between  $J$  and  $r_{ab}$  for the hydrogen molecule is shown below in figure 2.4:

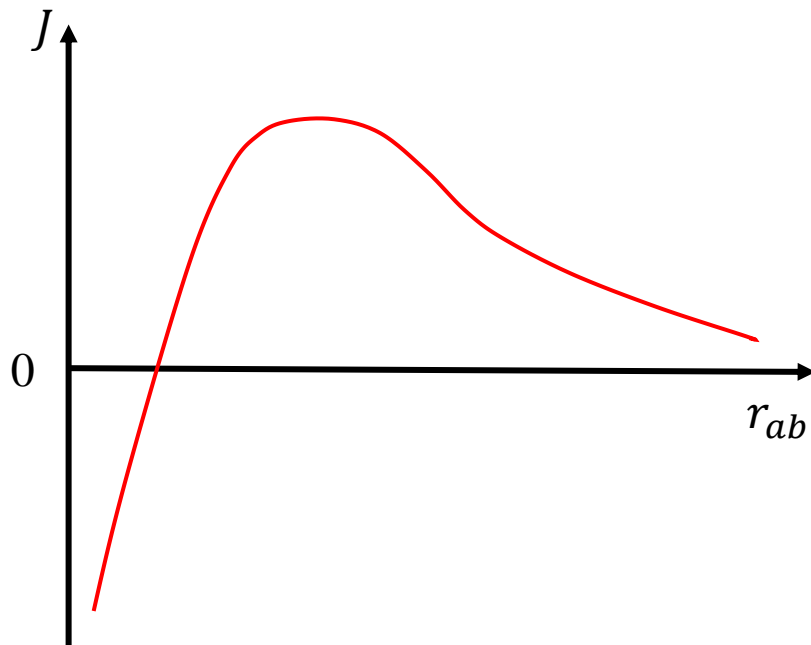


Figure 2.4. The exchange integral  $J$  as a function of  $r_{ab}$  which is the distance between the nuclei.

As shown in figure 2.4, to achieve a positive  $J$  value, a relatively large  $r_{ab}$  is required.

## 2.7 Ferromagnetic materials

At room temperature, the ferromagnetic elemental metals are Fe, Co and Ni. In this thesis, the most studied ferromagnetic materials are the alloys Permalloy ( $\text{Fe}_{20}\text{Ni}_{80}$ ) and CoFe.

## 2.8 Magnetic anisotropy

Experimentally<sup>10</sup>, it is found that the magnetization within a ferromagnetic material tends to align in certain preferred directions. This is known as magnetic

anisotropy. In this thesis, the types of magnetic anisotropy mainly fall into two different categories, magnetocrystalline anisotropy and shape anisotropy.

### **2.8.1 Magnetocrystalline anisotropy**

It is found that the magnetization tends to align along certain crystallographic axes. This is called magnetocrystalline anisotropy. This phenomenon is a quantum mechanical effect, the detailed calculation of which would be well beyond the scope of this thesis. In brief, this anisotropy is the result of the spin-orbit coupling. The orbital wave functions contain information about the symmetry of the lattice since the interaction between the atoms within the lattice is the result of the crystal field and the overlap of wave functions. The spins are ‘aware’ of the crystal via the spin-orbit coupling.

### **2.8.2 Shape anisotropy**

Consider a spherical ferromagnetic sample without magnetocrystalline anisotropy. The magnetization could lie in any direction since the demagnetization energy will be the same. If the same material is squashed into a thin film, with the thickness much smaller than the other two dimensions, the magnetization tends to lie within the film plane in order to minimize the demagnetization energy.

## **2.9 Domain and domain walls**

In practice, most ferromagnetic samples exhibit only a small net magnetization in the absence of an applied magnetic field due to the presence of magnetic domains within which the magnetization lies in different directions. Thus, the magnetic moments within different domains cancel each other out. It was Weiss in 1907 who first proposed that the magnetization has fixed magnitude but

arbitrary direction. Barkhausen<sup>11</sup> later on found that there were always discontinuities during the magnetization process. Further study<sup>12</sup> by Sixtus and Tonks showed that this was due to the displacement of magnetic domain boundaries, known as domain walls. Bloch<sup>13</sup> then pointed out theoretically that domain walls must be at least several hundred lattice constants in width since an abrupt change of magnetization over a very small distance would cost lots of energy due to the exchange interaction. A domain structure in a NiFe thin film is shown in figure 2.5.

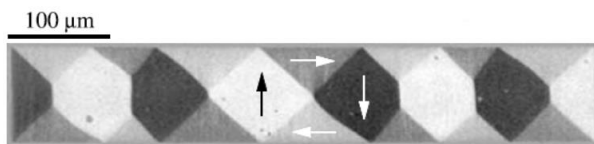


Figure 2.5 Domain structure in a NiFe thin film, arrows denote the direction of the magnetization within each domain<sup>14</sup>.

### 2.9.1 The formation of domains

As has been discussed before, the three main factors that can affect the energy of the magnetic system are the exchange interaction, the magnetostatic interaction and the anisotropy. If we consider the small square thin film ferromagnet in a single domain state shown in figure 2.6(a), the exchange energy is minimized since all magnetic moments are aligned parallel to each other, but the magnetostatic energy is large due to the magnetic charge at opposite sides of the sample. In figure 2.6(b), the magnetostatic energy has been reduced by forming two anti-parallel domains, but the exchange energy has increased significantly within the domain wall. In figure 2.6(c), the magnetization within the sample forms a closure domain structure, which is also called the Landau state, which has the minimum total energy.

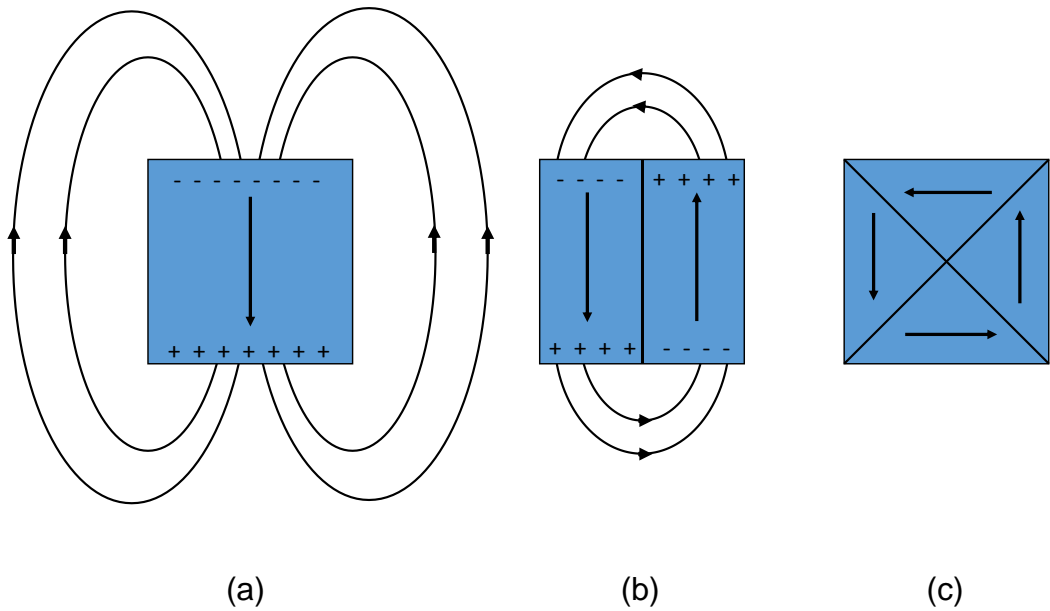


Figure 2.6 Formation of a closure domain structure, arrows denote the magnetization direction in domains.

### 2.9.2 Domain wall

From 2.9.1 we know that sometimes a multi-domain state is required in order to minimize the magnetostatic energy, but an abrupt change of the magnetization direction is not favoured since this would cost much more exchange energy. Therefore, due to the competition between the magnetostatic interaction and the exchange interaction, a transition region in which the magnetization changes its direction gradually is formed. This region is called a magnetic domain wall. There are generally two types of domain walls, Bloch walls and Néel walls. Bloch walls usually exist within bulk materials. As shown in figure 2.7(a)<sup>15</sup> the magnetization rotates out of the  $x$ - $y$  plane, yielding the accumulation of magnetic charge at the surfaces of the materials. Within a very thin film materials, a Bloch wall would cost much more magnetostatic energy, so a Néel wall [shown in figure 2.7(b)], in which the magnetization rotates within the  $x$ - $y$  plane from one domain to another, is favoured instead. For example, Permalloy thin film with thickness less than  $\sim 50$  nm could support Néel walls. Thicker Py

films ( $\sim 100$  nm) could support more complicated ‘cross-tie’ walls, for which the main Néel wall is cut at regular intervals by short tight-angle ‘cross-ties’ that terminate in free, single ends<sup>16</sup>. In this thesis, a special Néel wall will be discussed, named transverse domain wall, which is shown in Figure 2.7(b) to (f). Usually in nanowires, the majority of the magnetizations within the wire are aligned parallel to the length while the net magnetization within the domain wall is aligned perpendicular to the length due to the shape anisotropy. (c) and (d) are called head to head (HH) domain wall while (e) and (f) are called tail to tail domain wall (TT). More details about this type of domain wall will be introduced in Chapter 6 which will be devoted to studying the dynamics of coupled domain walls within nanowires.

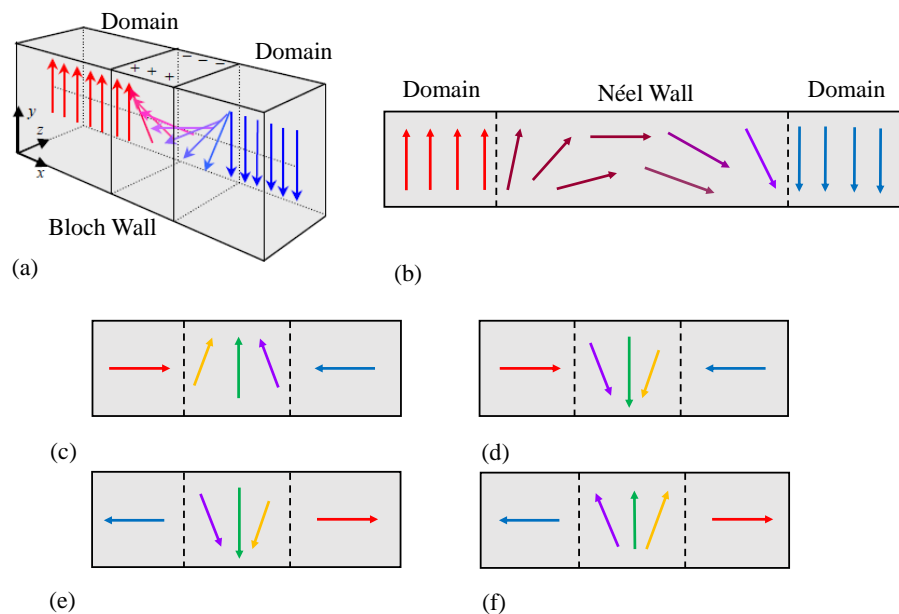


Figure 2.7. (a) Bloch wall in bulk materials. (b) Néel wall in thin film materials.<sup>15</sup> (c) - (f), transverse domain walls. Arrows denote the magnetization direction.

## 2.10 Magnetic Vortex

Magnetic vortex structures are usually found within ferromagnet nanodots or nanosquares. They result from the competition between the magnetostatic

interaction and the exchange interaction. From figure 2.8<sup>17</sup> we can see that within a circular nanodot, the magnetization of the magnetic vortex curls in-plane around a region of the magnetization that points out-of-plane<sup>18</sup>. The center region is called the vortex core, and usually has a diameter of a few nanometers<sup>19</sup>.

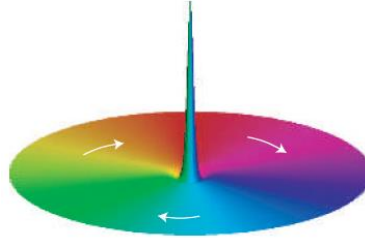


Figure 2.8 Magnetic vortex structure within a nanodot<sup>17</sup>, the core in the middle of the disk is the out-of-plane magnetization.

## 2.11 Superparamagnetic limit

As has been discussed in section 2.7, the magnetization in a ferromagnet is not absolutely stable above 0 K, but instead precesses with a very small angle due to thermal agitation. If the thermal agitation is strong enough to destroy the ferromagnetic order, the material will become paramagnetic and is then described by the Curie-Weiss law. Consider a single domain particle with uniaxial anisotropy, the magnetic anisotropy energy is:

$$E = \frac{1}{2}CV\sin^2\alpha, \quad (2-37)$$

where  $C$  is a constant related to the anisotropy,  $V$  is the volume of the particle and  $\alpha$  is the angle between the easy axis and the magnetization. As shown in Figure 2.9,  $\alpha = 0$  or  $\pi$  have lowest energy. If the thermal fluctuation energy is greater than  $0.5CV$ , the magnetization can move between those two equally low

energy states, which have anti-parallel magnetization. If the magnetization of this particle is sampled over time, the remanence magnetization would be zero. This is unhelpful for the design of magnetic recording devices, since the remanence magnetization within the recording media over time must be stable.

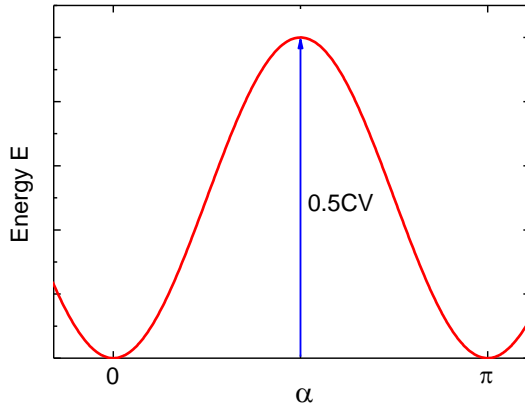


Figure 2.9 The energy of a single domain particle with uniaxial anisotropy as a function of the angle  $\alpha$  between the magnetization and the easy axis.

## 2.12 Magnetic hysteresis loop

As discussed above, a ferromagnetic specimen may contain many domains in which the magnetization is aligned in different directions. Since the net magnetic moment of the whole specimen is the vector sum of those in the domains, a ferromagnetic specimen usually exhibits a small net magnetic moment in the absence of an applied magnetic field. However, if an external field is applied, the magnetization within each domain is forced to align with the external field, yielding a net magnetic moment. Usually, we plot the magnetization component along the external field as a function of the external field. A typical curve is plotted in figure 2.10, and is called a magnetic hysteresis loop.

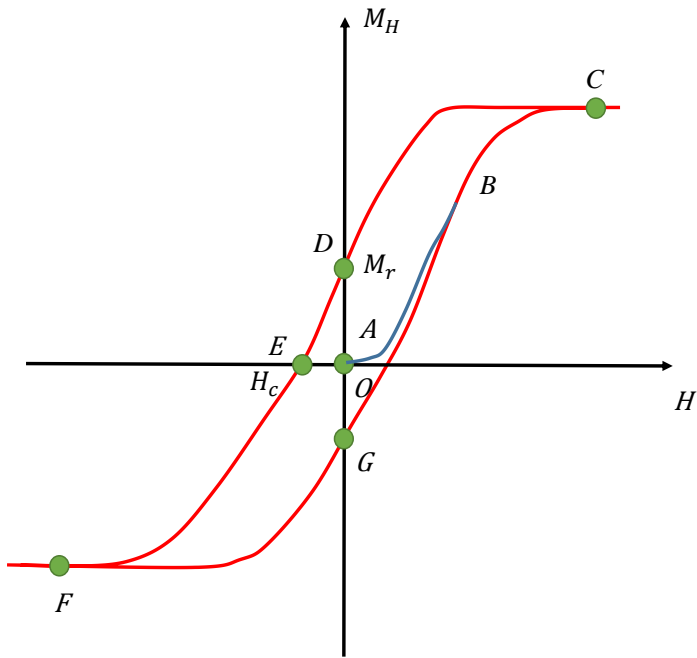


Figure 2.10. A typical magnetic hysteresis loop, the loop is run by the sequence of A-B-C-D-E-F-G-C.

It is assumed that the sample is initially in a demagnetized state, with zero net magnetic moment. Once an external field is applied to the sample, domains with different magnetization orientation begin to rotate parallel to the field. Therefore, a net magnetic moment along the direction of the applied field begins to develop. As the external field increases, the magnetic moment will reach its saturation, shown at position C, if we decrease the field, the curve will not follow the original path AB, but will instead go from C to D as the field decreases to 0. If we increase the field again in the opposite direction, we obtain the curve from D to E and then F, corresponding to saturation in the opposite direction. Again, if we decrease the field from F, the curve will go from F to G, and then C again if we go to positive saturation again. Therefore, if we start with a demagnetized sample, we will obtain the path ABCDEFGC. Since the magnetization lags the applied field, work is performed on taking the material through a cycle, and is given by the following equation:

$$W = \oint H dM_H. \quad (2-38)$$

The work is equal to the area enclosed by the hysteresis loop.

### 2.13 Stoner-Wohlfarth model

In the previous section, we reviewed how an external field magnetizes a multi-domain specimen by rotating the magnetization within different domains. The Stoner-Wohlfarth model gives a simple explanation of why domains rotate during this process.

If we consider a spherical single domain ferromagnetic particle with a uniaxial anisotropy shown in Figure 2.11, the shape anisotropy can be ignored, and the size of the particle is also too small to support more than one domain.

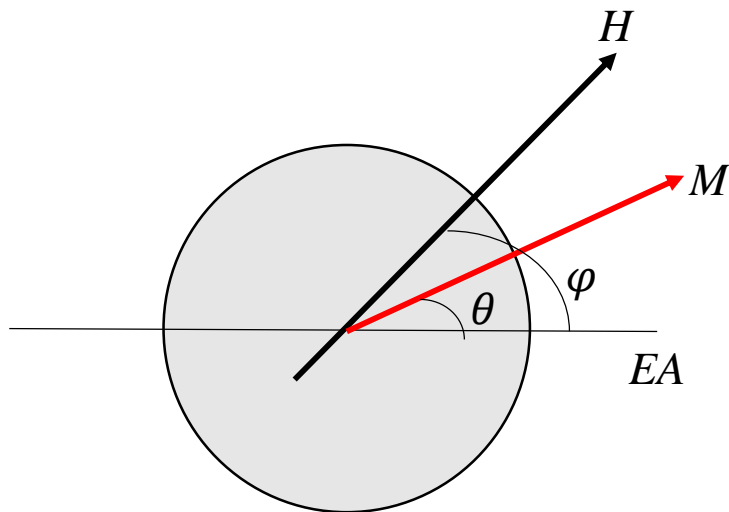


Figure 2.11 S-W model for a single domain spherical particle with uniaxial anisotropy but no shape anisotropy. *EA* denotes the easy axis, *H* and *M* denote the applied magnetic field and magnetization respectively.

The magnetic free energy density per unit volume may be written in the form:

$$E = -\mu_0 \mathbf{M} \cdot \mathbf{H} - K \cos^2 \theta, \quad (2-39)$$

where *K* is the uniaxial anisotropy.

Let's consider two simple cases,  $\varphi = 0$  and  $\frac{\pi}{2}$ . When  $\varphi = 0$ , equation (2-39) can be written as:

$$E = -\mu_0 M H \cos \theta - K \cos^2 \theta, \quad (2-40)$$

from which

$$\frac{\partial E}{\partial \theta} = \mu_0 M H \sin \theta + 2K \cos \theta \sin \theta. \quad (2-41)$$

When  $\frac{\partial E}{\partial \theta} = 0$ ,  $E$  has either minimum or maximum value. The solution is either  $\theta = 0$  or  $\frac{\pi}{2}$ .

To find the minima, the second order derivative

$$\frac{\partial^2 E}{\partial \theta^2} = \mu_0 M H \cos \theta + 2K \cos 2\theta \quad (2-42)$$

must be larger than 0. Therefore,  $\theta = 0$ . This means that if the magnetization is aligned perfectly parallel to the external field, it wouldn't rotate unless there is a small disturbance.

On the other hand, if  $\varphi = \frac{\pi}{2}$ , (2-39) has the form:

$$E = -\mu_0 M H \sin \theta - K \cos^2 \theta, \quad (2-43)$$

differentiation gives

$$\frac{\partial E}{\partial \theta} = -\mu_0 M H \cos \theta + 2K \cos \theta \sin \theta. \quad (2-44)$$

When  $\frac{\partial E}{\partial \theta} = 0$ , we obtain

$$\theta = \sin^{-1}\left(\frac{\mu_0 M H}{2K}\right). \quad (2-45)$$

From the calculation above, the hysteresis loops obtained when sweeping the field along the easy or hard axis are shown in figure 2-12.  $M_s$  is the saturation magnetization,  $H_c$  is the coercivity and  $H_k$  is the hard axis saturation field.

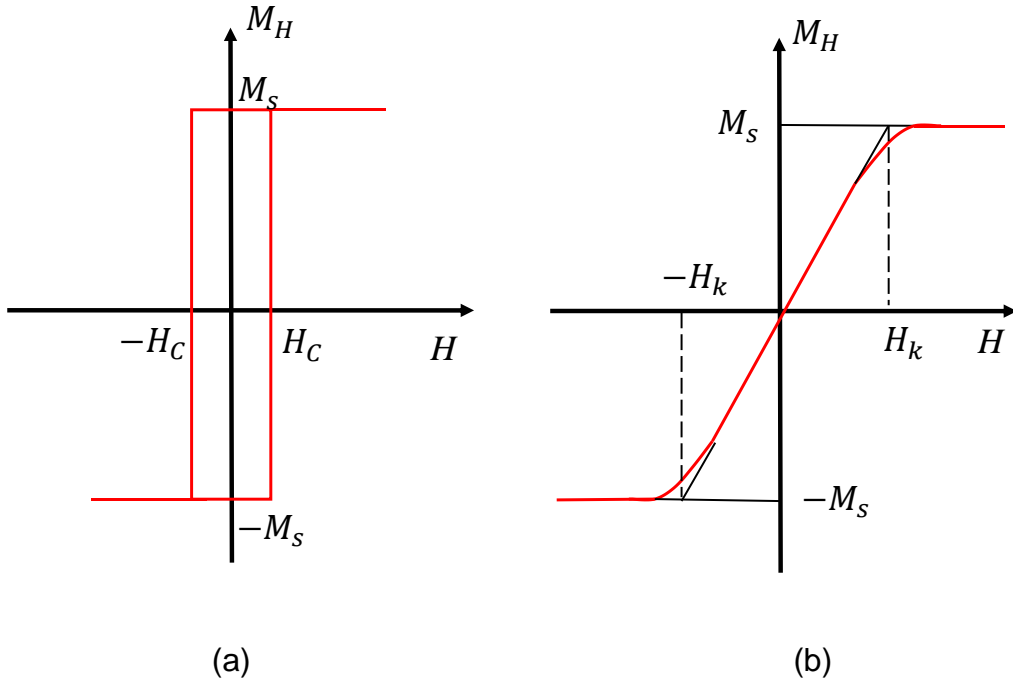


Figure 2-12. (a) Typical easy axis loop. (b) Typical hard axis loop.  $M_s$  is the saturation magnetization,  $H_c$  is the coercivity and  $H_k$  is the hard axis saturation field.

If the external field were applied between the easy and hard axis, the loop would look more like that shown in figure 2.10.

The above discussion assumes a single domain. For a multi-domain specimen, the hysteresis process involves both domain rotation and domain wall motion, and different mechanisms dominate under different circumstances. The latter can be driven by a magnetic field<sup>20</sup>, electric current<sup>21</sup> or voltage<sup>22</sup>.

## 2.14 Antiferromagnetism and interfacial exchange anisotropy

In antiferromagnetic materials, neighbouring magnetic moments are aligned antiparallel to each other and have equal value. Néel<sup>23</sup> first proposed that antiferromagnetic materials contain two sub-lattices with antiparallel spins, as

shown in figure 2-13. He assumed equal values of the magnetic moment since there is no net magnetic moment for the whole specimen. When the temperature is raised above a certain value known as the Néel temperature, the antiferromagnetic order will be destroyed and the sample will become paramagnetic.

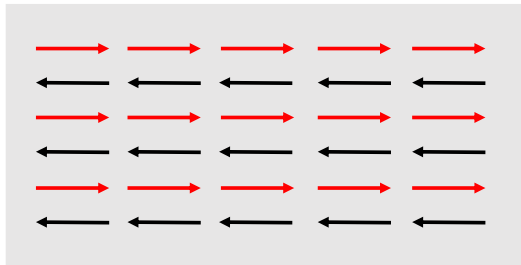


Figure 2-13. Antiferromagnetic order. Red and black arrows denote the opposite magnetic moments.

Within a hetero-structure containing adjacent antiferromagnetic and ferromagnetic layers, antiferromagnetic exchange bias can arise, for example, in the Co-CoO system<sup>24,25</sup>. The hysteresis loop of the ferromagnetic materials is shifted along the  $H$ -axis, as shown in figure 2-14(a). This is due to the exchange interaction<sup>26</sup> acting between the antiferromagnet and the ferromagnet at the interface. Suppose the Curie temperature of the ferromagnet is larger than the Néel temperature of the antiferromagnet. If the structure is cooled down from a temperature between  $T_C$  and  $T_N$  with an external bias field applied, the antiferromagnet will become ordered at the Néel temperature with the dipoles in the first atomic layer of the antiferromagnet becoming parallel to those in the adjacent ferromagnet, as shown in figure 2-14 (b). After removing the external bias field, since the antiferromagnetic phase has a large crystalline anisotropy, it will tend to align the magnetization of the ferromagnet in the direction that the external field was applied during field cooling.

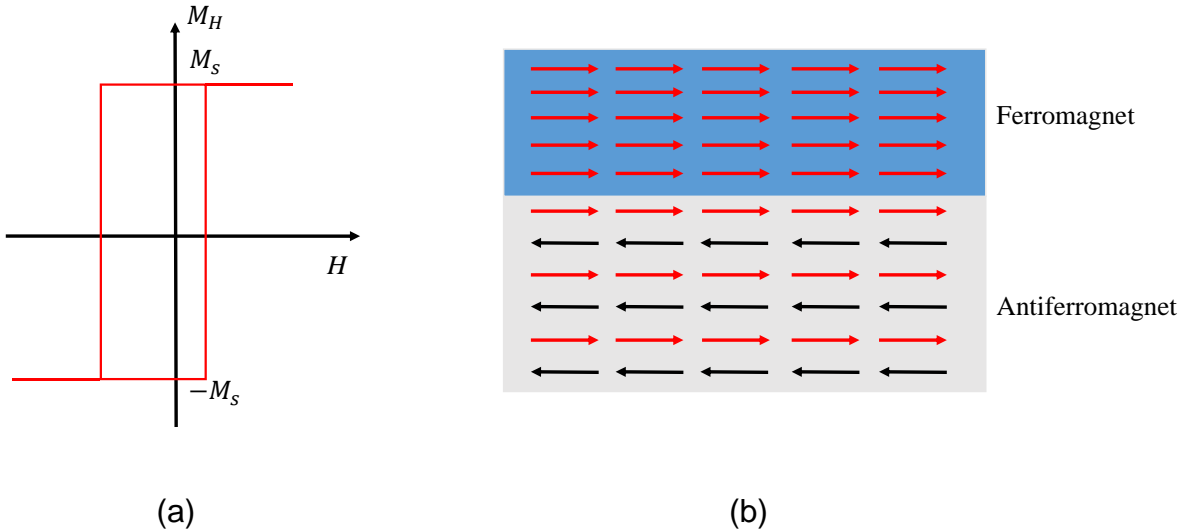


Figure 2-14. (a) The shifted hysteresis loop. (b) The antiferromagnet/ferromagnet bilayer, in which the interfacial spins within the antiferromagnet align with those within the ferromagnet spins.

## 2.15 Magnetic Dynamics

So far, we have reviewed ferromagnetism and antiferromagnetism in the equilibrium or static state. However, the dynamics of magnetic systems form the main part of this thesis.

### 2.15.1 Larmor precession

When a magnetic dipole  $\mathbf{m}$  experiences a uniform effective magnetic field  $\mathbf{H}_{\text{eff}}$ , the resulting torque  $\mathbf{T}$  can be written as:

$$\mathbf{T} = \mathbf{m} \times \mathbf{H}_{\text{eff}}. \quad (2-46)$$

In quantum mechanics, the angular momentum associated with the magnetic moment  $\mathbf{m}$  can be written as

$$\mathbf{L} = \frac{\mathbf{m}}{\gamma}, \quad (2-47)$$

where  $\gamma$  is the gyromagnetic ratio. The rotational form of Newton's second law, states that the rate of change of the angular momentum is equal to the torque, yielding the relationship

$$\frac{\partial \mathbf{L}}{\partial t} = \mathbf{T}. \quad (2-48)$$

Therefore

$$\frac{\partial}{\partial t} \left( \frac{\mathbf{m}}{\gamma} \right) = \mathbf{m} \times \mathbf{H}_{\text{eff}}, \quad (2-49)$$

which describes the precession of the magnetic moment around the effective field. Since the value of  $\gamma$  is negative, (2-49) is usually written as:

$$\frac{\partial \mathbf{m}}{\partial t} = -|\gamma| \mathbf{m} \times \mathbf{H}_{\text{eff}}. \quad (2-50)$$

Without any dissipation of energy, the magnetic moment would exhibit Larmor precession around the effective magnetic field, as shown in figure 2-15.

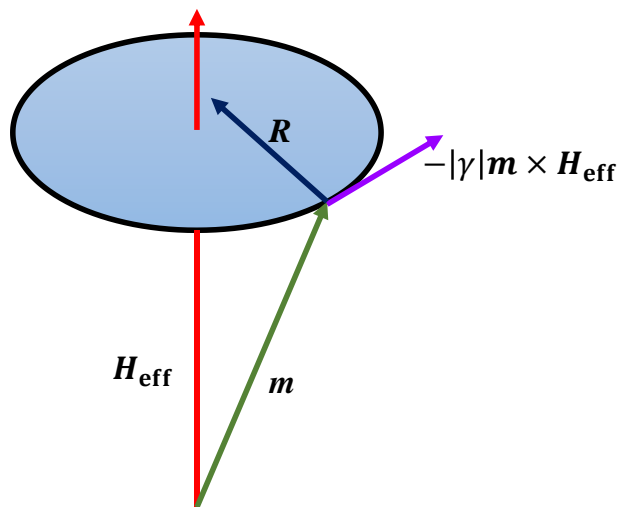


Figure 2-15 The precession of the magnetic moment around an effective magnetic field.  $\mathbf{H}_{\text{eff}}$  is the effective external field,  $\mathbf{m}$  is the magnetization,  $\mathbf{R}$  is the damping term.

## 2.15.2 Landau-Lifshitz-Gilbert Equation

In a real magnetic system, a freely precessing magnetic moment or magnetization tends to align with the effective magnetic field after a certain amount of time, reaching a state of equilibrium. To describe this motion, a phenomenological damping term is introduced<sup>27</sup>. This dissipative term is assumed to be proportional to the precession velocity and works to slow down the precession, and so a term  $-\eta \frac{\partial \mathbf{m}}{\partial t}$  is added to the effective field, where  $\eta$  is a positive constant, so that

$$\frac{\partial \mathbf{m}}{\partial t} = -|\gamma| \mathbf{m} \times (\mathbf{H}_{\text{eff}} - \eta \frac{\partial \mathbf{m}}{\partial t}). \quad (2-51)$$

Usually, this equation is written as:

$$\frac{\partial \mathbf{m}}{\partial t} = -|\gamma| \mathbf{m} \times \mathbf{H}_{\text{eff}} + \frac{\alpha}{|\mathbf{m}|} \mathbf{m} \times \frac{\partial \mathbf{m}}{\partial t}, \quad (2-52)$$

and is referred to as the Landau-Lifshitz-Gilbert equation, where  $\alpha = |\gamma| |\mathbf{m}| \eta$  is the Gilbert damping constant. Taking the vector product of  $\mathbf{m}$  with each side of (2-52), we obtain

$$\mathbf{m} \times \frac{\partial \mathbf{m}}{\partial t} = -|\gamma| \mathbf{m} \times (\mathbf{m} \times \mathbf{H}_{\text{eff}}) + \frac{\alpha}{|\mathbf{m}|} \mathbf{m} \times (\mathbf{m} \times \frac{\partial \mathbf{m}}{\partial t}). \quad (2-53)$$

Since

$$\mathbf{a} \times (\mathbf{b} \times \mathbf{c}) = (\mathbf{a} \cdot \mathbf{c})\mathbf{b} - (\mathbf{a} \cdot \mathbf{b})\mathbf{c}, \quad (2-54)$$

(2-53) can be rewritten as:

$$\mathbf{m} \times \frac{\partial \mathbf{m}}{\partial t} = -|\gamma| \mathbf{m} \times (\mathbf{m} \times \mathbf{H}_{\text{eff}}) - \alpha |\mathbf{m}| \frac{\partial \mathbf{m}}{\partial t}. \quad (2-55)$$

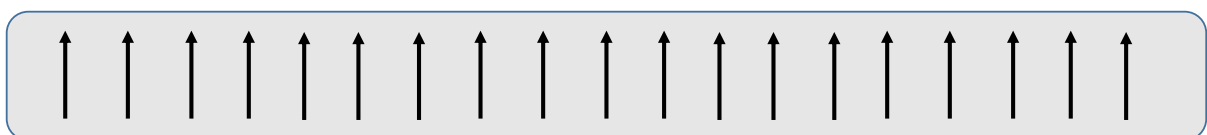
Substitute this result into (2-52), we obtain the Landau-Lifshitz equation:

$$\frac{\partial \mathbf{m}}{\partial t} = -\frac{|\gamma|}{1+\alpha^2} \mathbf{m} \times \mathbf{H}_{\text{eff}} - \alpha \frac{|\gamma|}{1+\alpha^2} \frac{\mathbf{m}}{|\mathbf{m}|} \times (\mathbf{m} \times \mathbf{H}_{\text{eff}}). \quad (2-56)$$

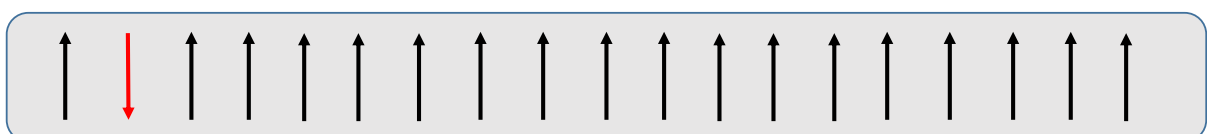
The first term on the right hand side of (2-56) describes the gyromagnetic precession and the second term describes the damping, which is labelled in figure 2-16 as  $R$ .

### 2.15.3 Spin Waves

In ferromagnetic crystals, a spin wave<sup>28</sup> is the propagation of a reversed macrospin through the crystal. Consider a ferromagnetic sample at 0 K, then, based on the third law of thermodynamics, the magnetic system should be completely ordered since there is no thermal agitation. Therefore a one dimensional spin system should appear as in figure 2.16(a). If the temperature then increases slightly, thermal fluctuations are introduced and a macrospin might be flipped, such as in the system shown in figure 2.16(b):



(a)



(b)

Figure 2.16. (a) The macrospin system at 0 K. (b) The macrospin system at temperature above 0 K and one of them is flipped by 180° due to the thermal agitation.

However, since the spin flip would cost lots of exchange energy the excitation with lowest energy is instead the propagating wave of macrospin shown in figure 2.17<sup>29</sup>. In order to reduce the exchange energy, the difference in the phase of precession between neighbouring spins varies gradually. Just as the phonon is used to describe quantized propagation of crystal vibrations, the magnon is used to describe quantized spin wave propagation.

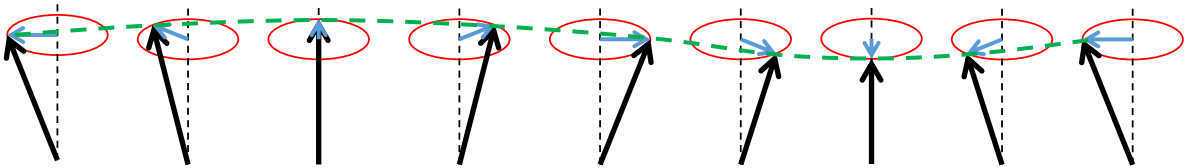


Figure 2.17. Simple representation of a spin wave. Black arrows denote the magnetization, blue arrows denote the projection of the magnetization onto a plane orthogonal to the equilibrium magnetization direction, and the green dashed line denotes the varying phase of magnetization precession.

Spin waves can also be introduced by non-uniformity of the magnetization dynamics, for example, by two-magnon scattering<sup>30</sup> during ferromagnetic resonance, which will be discussed next.

#### 2.15.4 Ferromagnetic Resonance

In an ideal ferromagnetic material, due to the strong exchange interaction between the spins, the magnetic moment tends to precess coherently. Therefore, it is easy and simple to consider the whole specimen as a macrospin precessing about the effective field. In the previous section, we showed that, due to the damping term within the LLG equation, the magnetic moment will align parallel to the effective field in equilibrium. However, precession can be achieved by applying a microwave field with a frequency  $\omega$  in a direction perpendicular to the static field. This phenomenon is known as ferromagnetic resonance (FMR). It is commonly used to study the dynamic properties of a

magnetic system. It can be understood that under certain conditions, the energy that the microwaves pump into the system can cancel or balance the damping, so that the magnetic moment can precess about the effective field in steady state.

### ***Equation of motion of FMR***

Consider an ellipsoidal specimen (shown in figure 2.18) with a uniaxial anisotropy along the principal axis. When uniformly magnetized as a single domain, the effective field can be written as:

$$\mathbf{H}_{eff} = \mathbf{H} + \mathbf{H}_1(t) - \tilde{\mathbf{N}} \cdot \mathbf{M} + \mathbf{H}_K, \quad (2-57)$$

where  $\mathbf{H}$  is the external static field applied along the z-axis,  $\mathbf{H}_1(t)$  is an external alternating field that is perpendicular to  $\mathbf{H}$  and lies within  $XY$  plane,  $\tilde{\mathbf{N}} \cdot \mathbf{M}$  is the demagnetizing field, and  $\mathbf{H}_K$  is the anisotropy field. In order to obtain a general solution, the anisotropy field can be written in terms of an effective demagnetizing tensor<sup>31</sup>  $\tilde{\mathbf{N}}_K$ , so that

$$\mathbf{H}_K = -\tilde{\mathbf{N}}_K \cdot \mathbf{M}. \quad (2-58)$$

For the sake of simplicity, the principle axes of the ellipsoid are chosen to be parallel to the three Cartesian axes, so that  $\tilde{\mathbf{N}}$  is diagonal. At the same time, in order to simplify the calculation, the easy and hard axis of the specimen will be assumed to lie along with the reference axes system shown in figure 2.18, therefore,  $\tilde{\mathbf{N}}_K$  is a diagonal tensor too. Since the alternating field lies in the  $XY$  plane, it has the form

$$\mathbf{H}_1(t) = H_{1x}(t)\mathbf{x} + H_{1y}(t)\mathbf{y} + H_{1z}(t)\mathbf{z}. \quad (2-59)$$

Usually experiments are performed in the regime where,  $|\mathbf{H}_1(t)| \ll |\mathbf{H}|$  and  $\mathbf{H}_1(t) = \mathbf{H}_{1,0}e^{i\omega t}$ .

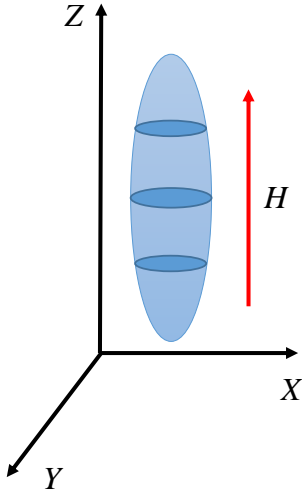


Figure 2.18. Ellipsoid specimen for FMR,  $\mathbf{H}$  is the applied external field.

As for the effective field, the magnetization  $\mathbf{M}$  can be expressed as two parts, an alternating part  $\mathbf{M}_1(t)$  and a static part  $\mathbf{M}_s$

$$\mathbf{M} = \mathbf{M}_1(t) + \mathbf{M}_s, \quad (2-60)$$

where  $|\mathbf{M}_1(t)| \ll |\mathbf{M}_s|$ , and

$$\mathbf{M}_1(t) = M_{1x}(t)\mathbf{x} + M_{1y}(t)\mathbf{y} + M_{1z}(t)\mathbf{z}. \quad (2-61)$$

where  $\mathbf{x}$ ,  $\mathbf{y}$  and  $\mathbf{z}$  are unit vectors. If we assume  $\mathbf{M}_s$  is constant and  $\mathbf{H}$  is applied parallel to the uniaxial anisotropy axis of the specimen, then substituting (2-60) into (2-52) and ignoring the second order terms yields

$$\begin{aligned} \frac{\partial \mathbf{M}_1(t)}{\partial t} = & -|\gamma|[\mathbf{M}_s \times \mathbf{H}_1(t) + \mathbf{M}_1(t) \times \mathbf{H} + M_s M_{1y}(t)(N_y + N_{Ky} - N_z - N_{Kz})i - \\ & M_s M_{1x}(t)(N_x + N_{Kx} - N_z - N_{Kz})j]. \end{aligned} \quad (2-62)$$

After scaling, (2-62) can be written as

$$\frac{i\omega M_{1x}(t)}{|\gamma|} = -M_{1y}[H + M_s(N_y + N_{Ky} - N_z - N_{Kz})] + M_s H_{1y} \quad (2-63)$$

and

$$\frac{i\omega M_{1y}(t)}{|\gamma|} = -M_{1x}[H + M_s(N_x + N_{Kx} - N_z - N_{Kz})] - M_s H_{1x}. \quad (2-64)$$

Since  $M_s$  is constant, the component  $\frac{\partial M_{1z}}{\partial t} = 0$ . For the case that  $\mathbf{H}$  is parallel to

Z axis or  $H_{1x} = H_{1y} = 0$ , the solutions for  $M_{1x}$  and  $M_{1y}$  are non-trivial when

$$\begin{vmatrix} \frac{i\omega_r}{|\gamma|} & -[H_r + M_s(N_y + N_{Ky} - N_z - N_{Kz})] \\ H_r + M_s(N_x + N_{Kx} - N_z - N_{Kz}) & \frac{i\omega_r}{|\gamma|} \end{vmatrix} = 0, \quad (2-65)$$

where  $H_r$  is the resonance field. Solving for resonance frequency  $\omega_r$  yields the so called Kittel formula

$$\omega_r^2 = \gamma^2 [H_r + M_s(N_x + N_{Kx} - N_z - N_{Kz})][H_r + M_s(N_y + N_{Ky} - N_z - N_{Kz})]. \quad (2-66)$$

### **Two magnon processes**

In the FMR experiment, the FMR linewidth may be defined as the full width at half maximum of the Lorentzian absorption line<sup>32</sup>, which has the form:

$$\Delta H_{FMR} = \frac{2\eta\omega_r}{\gamma}. \quad (2-67)$$

However, experimental data obtained from thin films generally shows a larger  $\Delta H_{FMR}$  value that results from an extrinsic contribution to the damping due to two magnon processes<sup>33</sup> first observed in yttrium iron garnet samples<sup>34</sup>. The two magnon scattering mainly originates from surface defects within the sample. In the ideal case, all spins precess coherently in response to the external alternating magnetic field. In fact the sample may support a whole spectrum of spin wave modes, with the uniform mode having wave vector  $\mathbf{k} = 0$ . In reality,

defects may scatter the uniform mode ( $k = 0$ ) into to a finite wave vector magnon that is degenerate in frequency, in analogy to the de Broglie wave scattering in quantum mechanics. A detailed calculation of two magnon scattering will not be presented since it is beyond the scope of this thesis.

## 2.16 Spin Transfer Torque and Spin Pumping

When a spin polarized current passes through a ferromagnetic layer, if the direction of the magnetization of the layer is different from the direction of the spin carried by the current, the magnetization of the ferromagnet exerts a torque on the spin-angular momentum of the injected electrons, causing them to become aligned with the local magnetization. Therefore the injected electrons must exert a torque on the ferromagnet. This is the so called spin transfer torque (STT) <sup>35</sup> (shown in figure 2.19) which was first proposed by J. Slonczewski<sup>36,37,38</sup>. Usually in a STT device, a non-metallic layer is sandwiched between two ferromagnetic layers, one of which is exchange biased by an antiferromagnetic layer.

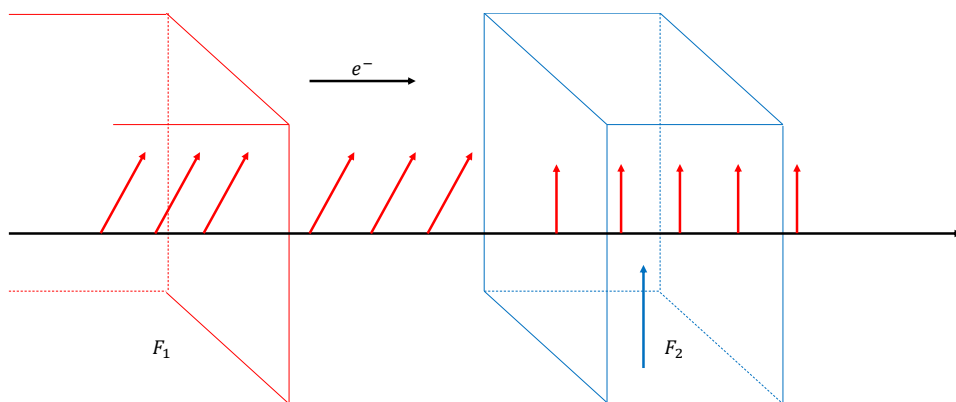


Figure 2.19. A depiction of spin transfer torque.  $F_1$  denotes layer 1 while  $F_2$  denotes layer 2. Red and blue arrows within  $F_1$  and  $F_2$  denote the magnetization within the layer 1 and 2 respectively. The red arrows in between  $F_1$  and  $F_2$  denote the electrons' spin polarization direction.

STT can also be added into the Landau-Lifshitz-Gilbert equation, as shown in figure 2.19. The dynamics within layer 2 can be described by the modified equation of motion:

$$\frac{\partial \mathbf{m}_2}{\partial t} = -|\gamma| \mathbf{m}_2 \times \mathbf{H}_{\text{eff}} + \frac{\alpha}{|\mathbf{m}_2|} \mathbf{m}_2 \times \frac{\partial \mathbf{m}_2}{\partial t} + |\gamma| \frac{1}{M_s d} (\boldsymbol{\tau}_{\parallel} + \boldsymbol{\tau}_{\perp}). \quad (2-68)$$

Here the third term on the right hand side is the spin transfer torque,  $\mathbf{m}_2$  denotes the magnetization of layer 2,  $d$  is the thickness of layer 2, while  $\boldsymbol{\tau}_{\parallel}$  and  $\boldsymbol{\tau}_{\perp}$  are the parallel and transverse spin torque that have the forms

$$\boldsymbol{\tau}_{\parallel} = aI \mathbf{m}_2 \times (\mathbf{m}_2 \times \mathbf{m}_1), \quad (2-69)$$

and

$$\boldsymbol{\tau}_{\perp} = bI \mathbf{m}_2 \times \mathbf{m}_1, \quad (2-70)$$

where  $a$  and  $b$  are constants,  $I$  is the charge current. STT can be used to switch or excite continuous precession of the magnetization in a certain layer.

The reciprocal process of spin transfer torque excitation is the so called ‘spin pumping’<sup>39,40</sup>, where a precessing magnetic layer pumps a pure spin current into an adjacent non-magnetic layer.



# Chapter 3 Experimental Techniques

## 3.1 Introduction

In this chapter, I will give a general introduction to the experimental techniques used in this thesis. The detailed experimental setups will be described within the following chapters where the experimental results will be discussed.

## 3.2 Magneto-Optical Kerr Effect

The magneto-optical Kerr effect (MOKE) has significantly impacted research on magnetic thin films. This is due to its sensitivity, spatial resolution, and experimental simplicity<sup>41</sup>. It was discovered by Kerr<sup>42</sup> in 1877 while he was examining the polarization of light reflected from a polished electromagnet pole. The phenomenon of MOKE can be described in the following way. When polarized light is reflected from a magnetic material, its polarization direction will experience a change, which is proportional to the magnetization  $M(T)$  and vanishes at temperatures above the Curie temperature<sup>43</sup>.

### 3.2.1 Different Geometries of MOKE

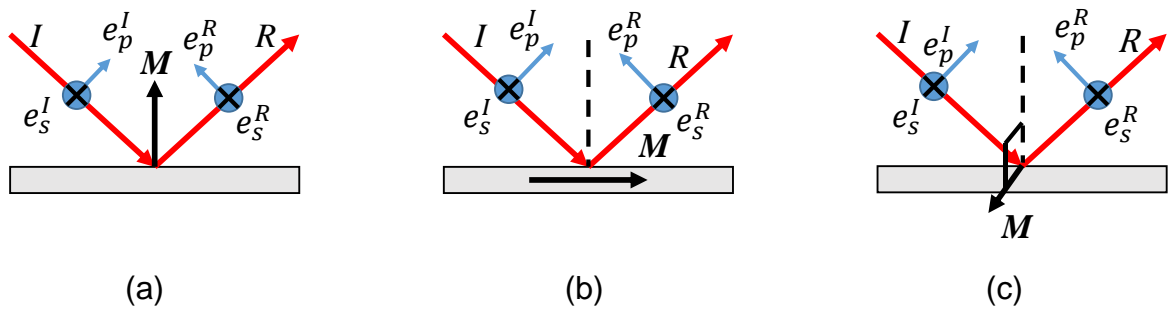


Figure 3.1. The three different MOKE configurations. (a) Polar (b) longitudinal and (c) transverse.  $I$  denotes the incident light,  $R$  denotes the reflected light and  $M$  denotes the magnetization. The subscript  $s$  denotes the electronic component perpendicular to the incident plane while the subscript  $p$  denotes the electronic component perpendicular to the light travelling direction but within the plane of incidence.

Depending upon the geometry of the plane of incidence and the magnetization, there are three different MOKE configurations, shown in figure 3.1, namely the polar (a), longitudinal (b) and transverse (c).

The oscillating electric field of the incident light can be decomposed into components parallel and perpendicular to the plane of incidence, which are called *p* and *s* component respectively. Figure 3.1 shows a schematic of the optical configuration at the boundary between two media. The counterpart of the MOKE is the Faraday effect, which describes the polarization change of light transmitted through a medium subject to a magnetic field.

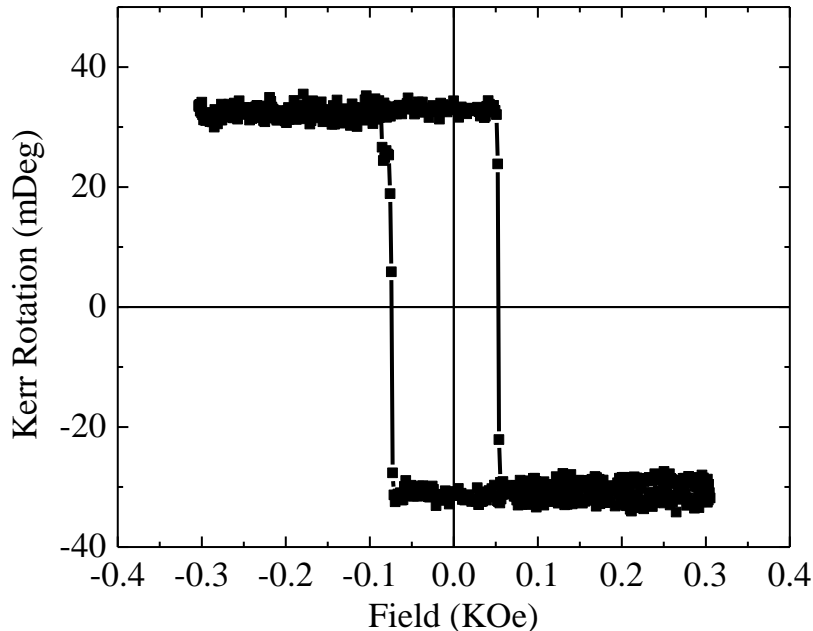


Figure 3.2. Hysteresis loop acquired in the longitudinal MOKE configuration from a ferromagnetic CrO<sub>2</sub> thin film

Usually, the longitudinal configuration is used to sense the change of magnetization in the plane of the surface, while the polar configuration is used to sense the change of magnetization out of plane. The transverse case is rarely used since it does not yield a Kerr rotation, instead, it results in a magnetization dependent reflectivity change. A typical hysteresis loop acquired

by longitudinal MOKE from a ferromagnetic CrO<sub>2</sub> thin film is shown in figure 3.2. In the hysteresis loop obtained from a conventional magnetometer, such as a vibrating sample magnetometer (VSM), the magnetization of the sample is expected to increase with increasing magnetic field. However, the measured Kerr rotation can have the same or opposite signs, depending upon the sign of the magneto-optic interaction.

### 3.2.2 The Origin of the Magneto-optical Kerr Effect

#### *Classical explanation*

The optical properties of a medium are determined by its dielectric tensor. Linearly polarized light can be treated as a sum of right and left circularly polarized modes. As the beam passes through a medium, the electric field will drive the electrons within the medium. The right and left polarized modes drive the electrons in right and left handed circular trajectories. Without a magnetic field, the radius of the circular motion will be the same in each case. Therefore, there is no difference between the dielectric constants for the left and right circular polarized modes. However, if there is a magnetic field applied parallel to the propagation direction of the electromagnetic wave, there will be a Lorentz force acting on each electron. The force points towards or away from the center of the circle for the left and right circular motion. Therefore, the symmetry has been broken, and the difference in propagation velocity for the left and right handed modes leads to polarization rotation. The different absorption of the left and right handed modes yields to a change of ellipticity.

## Quantum mechanical explanation

In 1932, Hulme<sup>44</sup> pointed out that it is the spin-orbit interaction that couples the electron spin to its motion to giving rise to a large Faraday rotation in ferromagnetic materials. The spin-orbit coupling is a result of the interaction between the electrons spin and the magnetic field which is sensed by the electron. This interaction couples the magnetic moment with the electron motion, therefore, linking the magnetic and optical properties of the medium.

### 3.2.3 A formalism to describe MOKE

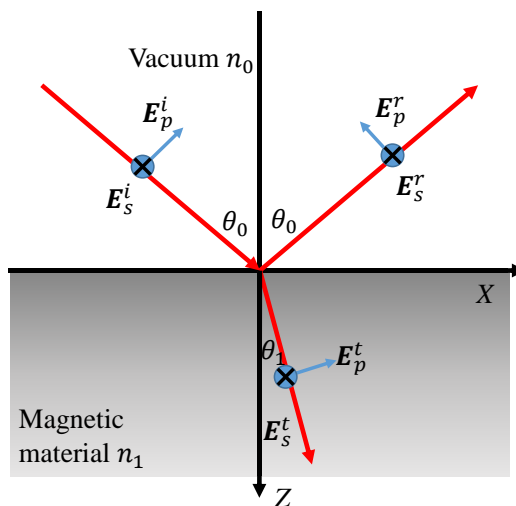


Figure 3.3 Light reflected and transmitted at the boundary between vacuum and a magnetic material. The subscription  $s$  denotes the electronic component perpendicular to the incident plane while the subscription  $p$  denotes the electronic component perpendicular to the light travelling direction but within the plane of incidence.

In general, the reflected and incident electric field amplitudes  $E^r$  and  $E^i$  are related through the reflectivity or Jones matrix:

$$\begin{bmatrix} E^r_s \\ E^r_p \end{bmatrix} = \begin{bmatrix} r_{ss} & r_{sp} \\ r_{ps} & r_{pp} \end{bmatrix} \begin{bmatrix} E^i_s \\ E^i_p \end{bmatrix}. \quad (3-1)$$

It is obvious that the non-zero off-diagonal components in the array indicate that there is a change of the polarization of the light reflected from the surface of

the material. If we consider light incident on the surface of a magnetic material from vacuum with refractive index  $n$ , shown in figure 3.3, the elements in the array in the first term of the right hand side of (3-1) have the following forms<sup>45</sup>:

$$r_{ss} = \frac{n_0 \cos \theta_0 - n_1 \cos \theta_1}{n_0 \cos \theta_0 + n_1 \cos \theta_1}, \quad (3-2)$$

$$r_{ps} = -\frac{iQn_0n_1 \cos \theta_0 (\sin \theta_1 u_x + \cos \theta_1 u_z)}{\cos \theta_1 (n_0 \cos \theta_0 + n_1 \cos \theta_1)(n_1 \cos \theta_0 + n_1 \cos \theta_1)}, \quad (3-3)$$

$$r_{pp} = \frac{n_1 \cos \theta_0 - n_0 \cos \theta_1}{n_1 \cos \theta_0 + n_0 \cos \theta_1} + \frac{2iQn_0n_1 \cos \theta_0 \sin \theta_1 u_y}{(n_1 \cos \theta_0 + n_0 \cos \theta_1)^2}, \quad (3-4)$$

$$r_{sp} = \frac{iQn_0n_1 \cos \theta_0 (\sin \theta_1 u_x - \cos \theta_1 u_z)}{\cos \theta_1 (n_0 \cos \theta_0 + n_1 \cos \theta_1)(n_1 \cos \theta_0 + n_1 \cos \theta_1)}, \quad (3-5)$$

where  $Q$  is the magneto-optical coupling strength (or Voigt) parameter, and

$\mathbf{u} = \frac{\mathbf{M}}{M_s}$ ,  $\theta_0$  and  $\theta_1$  are defined by Snell's law:

$$n_0 \sin \theta_0 = n_1 \sin \theta_1. \quad (3-6)$$

It should be noted that most magnetic materials are metal which are non-transparent for visible light, therefore the transmitted light intensity should be attenuated as the depth increases within the metal.

Usually the Kerr rotation and ellipticity are defined by elements from Jones matrix as:

$$\Phi_K = -Re \left( \frac{r_{sp}}{r_{pp}} \right) \quad (3-7)$$

and

$$\varepsilon_K = Im \left( \frac{r_{sp}}{r_{pp}} \right), \quad (3-8)$$

respectively for p-polarized incident light, while for s-polarized incident light

$$\Phi_K = \operatorname{Re} \left( \frac{r_{ps}}{r_{ss}} \right) \quad (3-9)$$

and

$$\varepsilon_K = \operatorname{Im} \left( \frac{r_{ps}}{r_{ss}} \right). \quad (3-10)$$

### 3.2.4 The Detection of MOKE

A simple longitudinal MOKE set up similar to that used in this thesis is shown in figure 3.4(a). A linearly polarized laser beam is incident on the sample surface and reflected back into a detector. Depending on the size of the sample, a lens might be needed in order to focus the light onto a smaller area. Inside the detector, the laser is split into two beams with orthogonal polarization directions by a Glan-Thomson beam splitter, and collected by two photodiodes. If we consider the electric vector of the beam lying 45 degrees from the X axis, as shown in figure 3.4(b), its two components are given by

$$E_x^r = E^r \cos \theta, \quad (3-11)$$

and

$$E_y^r = E^r \sin \theta. \quad (3-12)$$

Since the intensity sensed by the photodiode is proportional to the square of the amplitude of the electric field, the sum of the outputs of the two diodes is proportional to the full beam intensity, while the difference of the outputs, yields the quantity

$$\Delta I = (E^r)^2 (\cos^2 \theta - \sin^2 \theta) = (E^r)^2 \cos 2\theta. \quad (3-13)$$

Since the Kerr rotation is very small, usually much smaller than 1 degree, and if the initial angle is 45 degree, then

$$\Delta I \propto \Delta\theta.$$

(3-14)

Therefore, by measuring the difference of the intensity of the two beams, we can calculate the Kerr rotation after dividing by a calibration factor.

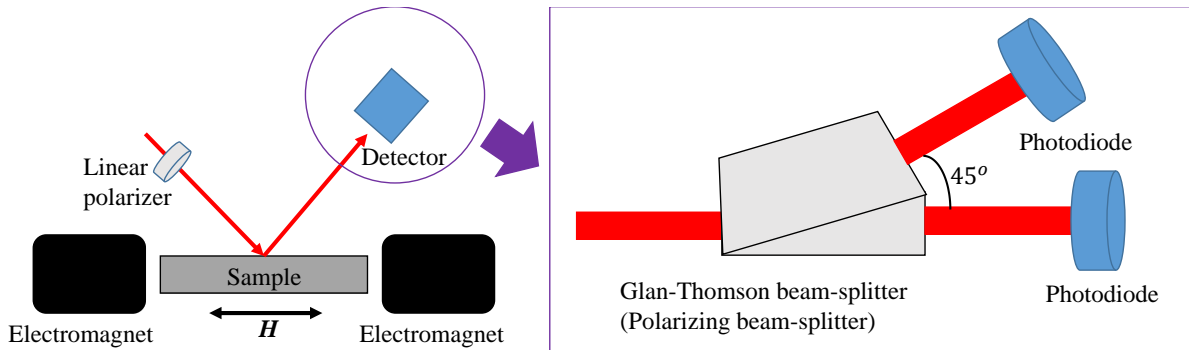


Figure 3.4(a) A simple longitudinal MOKE set up and the detector configuration.  $H$  is the applied magnetic field by the electromagnet.

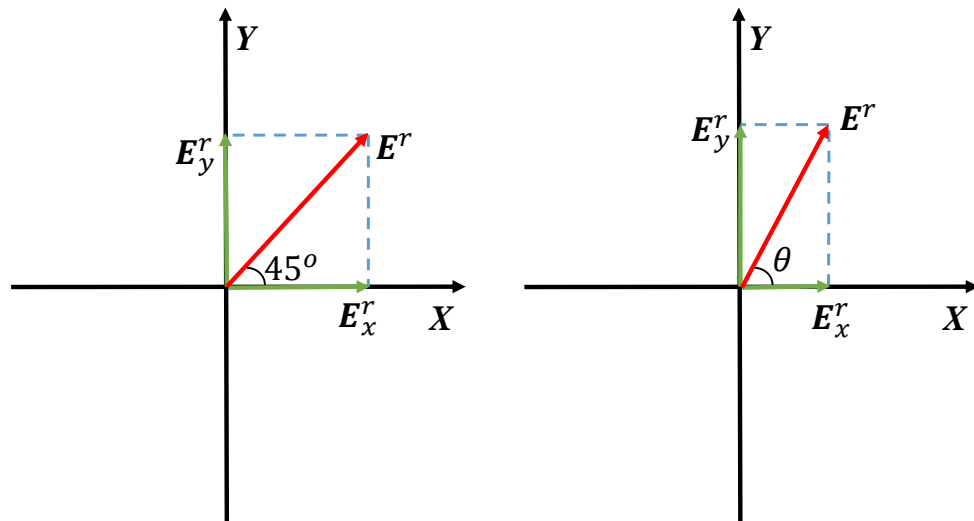


Figure 3.4(b) Rotation of the electric field vector and its components.

However, when measuring magnetization dynamics, the magnetization precesses about a certain magnetic field, and the static magnetization does not necessarily lie in the plane of incidence shown above. Therefore, it may be necessary to sense all three Cartesian components of the magnetization to form a complete picture of how the magnetization changes. From figure 3.5, we can

see that by detecting  $\Delta M_x$ ,  $\Delta M_y$  and  $\Delta M_z$  within a Cartesian coordinate system, a full picture of  $\Delta M$  can be formed.

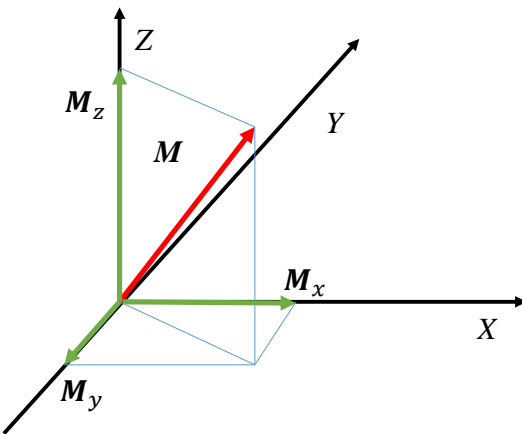


Figure 3.5 Three Cartesian components of the magnetization.

In order to record the three Cartesian components of the magnetization simultaneously, a normal incidence beam and a vector bridge detector<sup>46</sup> are required. The set up is shown in figure 3.6(a).

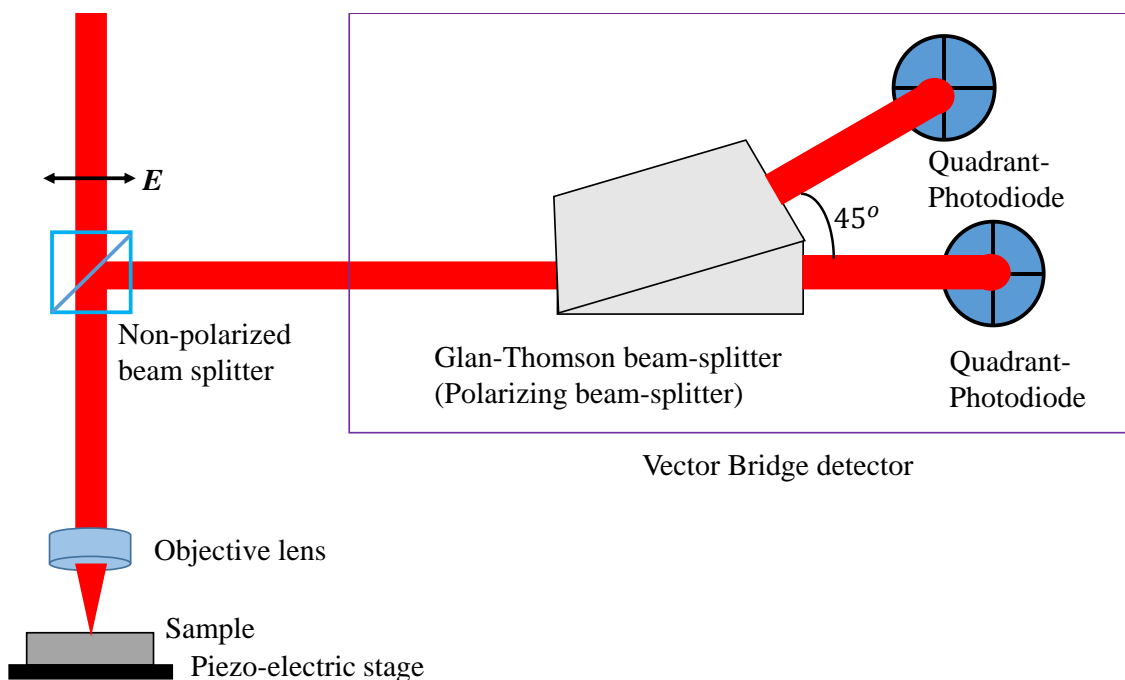


Figure 3.6(a) Set up for scanning Kerr microscopy. The piezoelectric stage allows the beam to be focused at a particular position on the sample.  $E$  is the electric component of the light.

A linearly polarized laser beam is focused on the surface of the sample at normal incidence by an objective lens. Depending on the numerical aperture of the lens and the wavelength, the focused spot size should be at least larger than half of the wavelength. After the focused beam is reflected back from the sample, it is re-collimated again by the objective lens and then goes into a vector bridge detector through a non-polarizing beam splitter. The only difference between the vector bridge detector and the detector mentioned before is that, within the vector bridge detector, there are two quadrant photodiodes instead of two normal photodiodes. The quadrant photodiode is divided into four equal parts that sense the incident light intensity individually. Therefore, the beams are also divided into four parts if they are aligned so as to be incident on the center of the diodes. As shown in figure 3.6(b) from reference 15, the beam focused onto the sample through an objective lens forms a cone shape after the lens and can also be divided into four equal parts,  $a$ ,  $b$ ,  $c$  and  $d$ . The beam incident from the  $a+b$  half will be reflected back to the  $c+d$  half, while the beam incident from the  $c+d$  half will be reflected back to the  $a+b$  half. The intensity sensed by the quadrant photodiodes will be  $I_{(c_1+d_1)}$  and  $I_{(c_2+d_2)}$ , and  $I_{(a_1+b_1)}$  and  $I_{(a_2+b_2)}$ . The longitudinal Kerr rotation due to the component of magnetization along the  $X$  axis can be obtained from the intensity difference

$$\Delta I_X = I_{(c_2+d_2)} - I_{(c_1+d_1)}, \quad (3-15)$$

for the the  $c+d$  part of the beam, and

$$\Delta I_{-X} = I_{(a_2+b_2)} - I_{(a_1+b_1)}, \quad (3-16)$$

for the the  $a+b$  part. Reversing the incident beam direction reverses the sign of the longitudinal Kerr rotation and so  $a+b$  and  $c+d$  parts of the beam exhibit Kerr

rotations of opposite sign due to the longitudinal Kerr effect. Obviously both halves of the beams also contain polar Kerr rotation due to any out-of plane magnetization, but the polar component has the same sign across the whole beam. So if we subtract  $\Delta I_X$  and  $\Delta I_{-X}$  the polar component will disappear, giving:

$$|\Delta I_X - \Delta I_{-X}| = 2|\Delta I_X|. \quad (3-17)$$

The same principles apply to the *b+c* and *a+d* halves.

For the detection of the polar component, if we add the four parts together, the longitudinal parts will disappear since they have opposite sign. Therefor in this case:

$$|\Delta I_Z| = I_{a_2+b_2+c_2+d_2} - I_{a_1+b_1+c_1+d_1}. \quad (2-18)$$

More details of the principle of operation of the vector bridge detector can be found in reference 15.

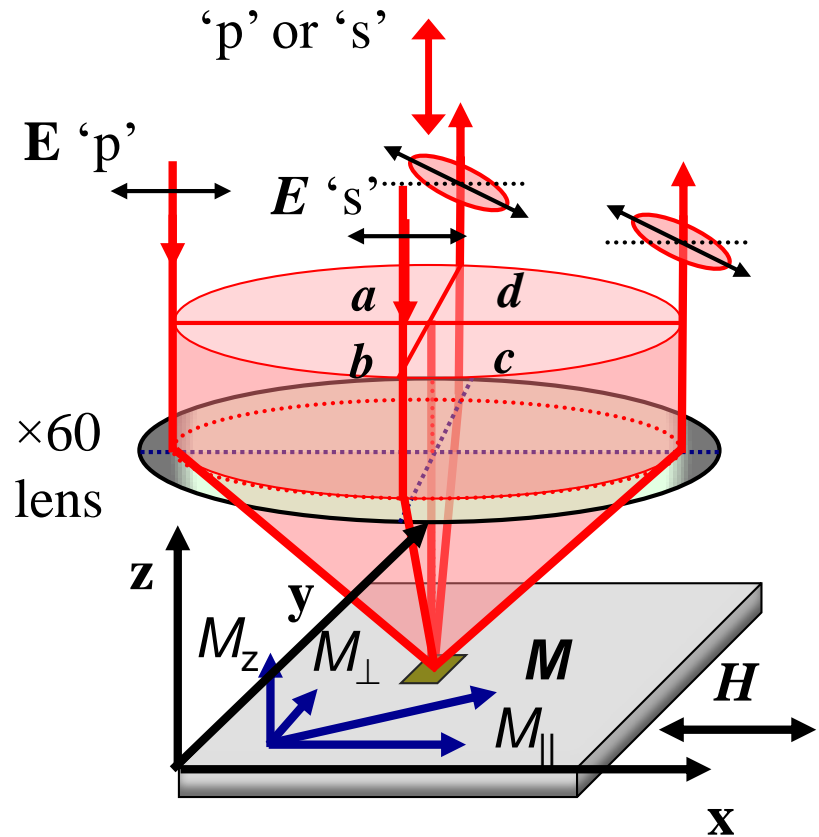


Figure 3.6(b) Cone of rays focused onto the sample through an objective lens, where a, b, c and d denote the beam in different quadrants<sup>15</sup>. S and p are the same notifications as in Figure 3.1 and 3.3 to denote the light polarization direction relative to the incident plane.

### 3.2.5 Time resolved scanning Kerr microscopy

As a stroboscopic measurement technique, time resolved scanning Kerr microscopy has benefited from the development of mode-locked laser technology<sup>47</sup>. Mode-locking is a technique in optics by which a laser can be made to produce pulses of light with duration on the order of 100 femtoseconds (fs)  $\sim 10^{-13}$ s. The basic idea of this technique is to introduce a certain phase relationship between the different longitudinal modes within the laser cavity, so that the output of the laser will be a train of ultra-narrow pulses separated in

time by the round trip time of the cavity. Details of the mode locking technique lie beyond the scope of this thesis.

In time resolved scanning Kerr microscopy (TRSKM), the laser pulses are analogous to the flash light of a camera. In a conventional camera, the flash is present for a very short time in order to form an image on the film. If the object is static or moves on timescales that are long compared to the duration of the flash, then acceptable images can be obtained, but if the objective is moving quickly, then the image may become blurred. Since the magnetic dynamics of interest happen in the picosecond time range, if a continuous wave or ns laser were used to study the magnetic dynamics<sup>48</sup>, only ‘blurred’ information could be acquired at best. This is the reason that femtosecond laser pulses are required while studying magnetization dynamics by TRSKM.

A practical TRSKM set up has been described elsewhere<sup>49</sup>. Figure 3.7 shows the basic set up in our lab. A Ti: Al<sub>2</sub>O<sub>3</sub> mode locked laser and an electric impulse generator are synchronized by a master clock. The laser pulse is delivered into a retro-reflector which we make use of to control the relative delay of the optical and electric pulses at the sample. The beam reflected back from the sample is re-collimated again and delivered into the detector. The electrical output from the detector goes into a lock-in amplifier(s) for which the reference signal is taken from the same function generator used to modulate the electric pulse generator. The signal recovered by the lock-in amplifier is recorded by a computer. For different samples, the experimental set up may vary, but the basic operation is the same. More details about the TRSKM can be found from Dr P. S Keatley’s PhD thesis<sup>15</sup>, who contributed significantly in setting up the Kerr microscope.

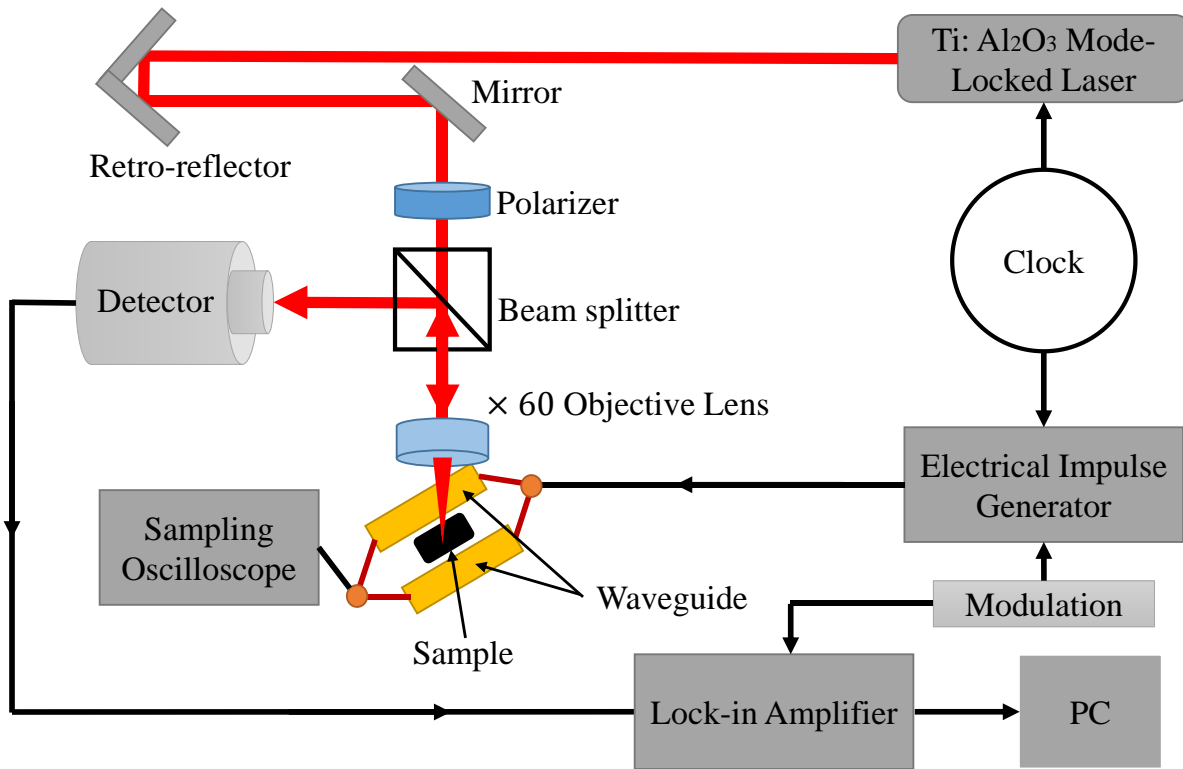


Figure 3.7 Time resolved scanning Kerr microscopy set up, clock denotes a master oscillator which synchronizes the laser pulses and the electrical pulses.

### 3.2.6 Time resolved low temperature MOKE

Some antiferromagnetic materials, such as Dy, CoO, NiO etc, have their Néel temperature near to or below room temperature. In order to study the dynamics of magnetic devices containing those kinds of materials, low temperature MOKE operation is required.

Figure 3.8 shows the low temperature time resolved MOKE set up in our lab. As for the TRSKM, the 800 nm mode-locked laser and the pulse generator are synchronized by the same master clock, with the retro-reflector to control the relative delay of the electrical pulse and the laser. Depending upon the required temperature, either liquid nitrogen or helium can be used as the cryogen. The laser is focused onto the sample by a lens through the window of the cryostat, and is re-collimated again before it is delivered into the detector. The window of

the cryostat is made of low Verdet constant glass in order to minimize the Faraday rotation introduced by the window.

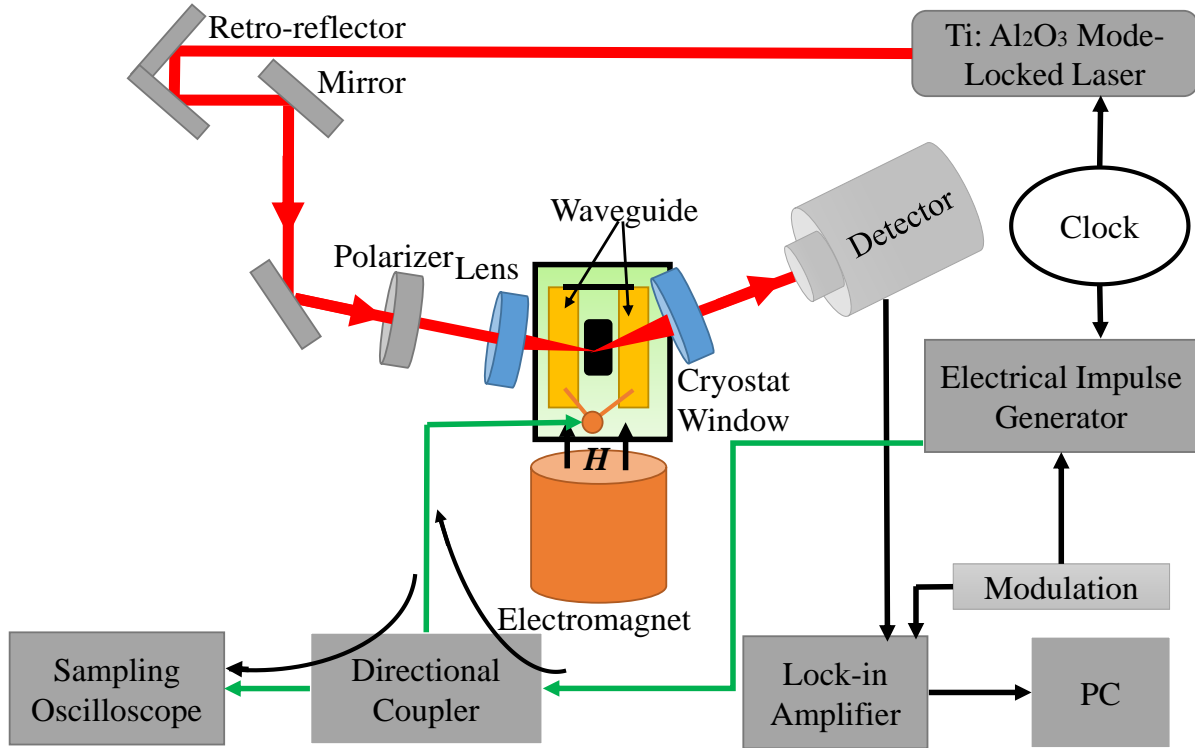


Figure 3.8. Low temperature MOKE set up; clock denotes the same master oscillator in figure 3.7.

Figure 3.9 shows the sample assembled within the cryostat between the pole pieces of the electromagnet. One pole of the electromagnet lies immediately beneath the cryostat while the return pole consists of a ring, surrounding the cryostat tail at a position above the sample location. The sample sits on a cold finger made of copper and is connected to a printed circuit board (PCB) by silver paint, from which the electrical RF or pulse is delivered into the sample waveguide. The whole cryostat is mounted on an adjustable height table in order to adjust the sample position relative to the laser beam. During low temperature operation, the cryostat chamber is pumped down to  $\sim 10^{-6} \text{ mbar}$ .

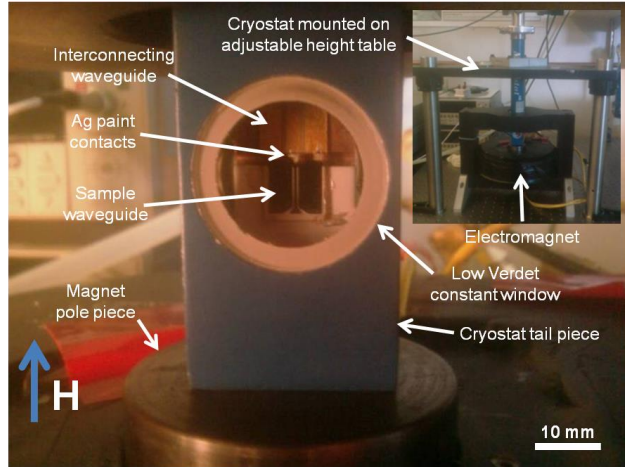


Figure 3.9 the sample assembled in the cryostat between the pole pieces of the electromagnet<sup>50</sup>.

The detailed experimental set up will be slightly different in each of the following chapters and I will introduce the specific set up within each chapter.

### **3.3 X-Ray magnetic circular dichroism (XMCD) and X-Ray magnetic linear dichroism (XMLD) measurements**

As has been discussed before, MOKE and TRMOKE are powerful tools with which to study magnetic dynamics. However, most magnetic devices today have multi-layered structures and the magnetic dynamics within each layer is not necessarily the same. MOKE and TRMOKE sense only the collective response from the magnetic layers that the laser can penetrate through. In order to study the magnetic dynamics within a specific layer in a magnetic device or the response of the anti-ferromagnetic (AFM) layer within an exchange biased magnetic structure, XMCD and XMLD should be performed when necessary. This thesis is mainly concerned with TRMOKE studies of magnetic devices and materials, so only an introduction to XMCD and XMLD is given. A systemic introduction of X-Ray measurements can be found in reference 50.

### **3.3.1 XMCD<sup>51</sup>**

Measurement of x-ray magnetic circular dichroism using synchrotron radiation is a widely used technique for element specific characterization of magnetic materials and devices today. In ferromagnetic materials, the absorption rate for left and right circular polarized X-rays is different and depends upon the projection of the net magnetic moment along the wavevector. Therefore, by measuring the difference of the absorption rates for left and right circular polarized X-rays, information can be obtained about the magnetization of ferromagnetic materials. A change or rotation of the net magnetic moment can be detected if it leads to a change of the projection along the X-ray wavevector. The pulsed nature of synchrotron radiation X-ray makes it suitable for stroboscopic pump-probe measurements, in the same way that a mode-locked laser is suitable for TRSKM. In addition, and most importantly, by tuning the photon energy of the X-ray, spin dynamics from different elements can be sensed individually.

### **3.3.2 XMLD<sup>51</sup>**

In chapter 7, the magnetic dynamics within an exchange biased structure will be studied. Since there is no net magnetic moment within the AFM layer, it is not possible to probe the dynamics with MOKE or XMCD. However, XMLD can be performed instead. In XMLD the same signal is obtained irrespective of whether the magnetic moment lies parallel or anti-parallel to the x-ray wavevector.

The experimental set up will be introduced in chapter 7 since it is specific to that chapter.

### **3.4 Summary**

In this chapter, I have introduced the basic principles of MOKE and the general experimental set up of the TRSKM. A brief introduction of XMCD and XMLD were presented too. Although in the following chapters, different studies required slightly different experimental set ups, the general idea stays the same.

## **Chapter 4 Time resolved scanning Kerr microscopy of hard disk writer yokes**

The samples studied in this chapter were fabricated at Recording Heads Operation, Seagate Technology, MN, USA. The TRSKM studies were performed by myself at the University of Exeter. Particular thanks go to Dr. P. Czoschke at Seagate Technology, for his advice and suggestions that influenced the direction of this study. I also wish to thank Dr. M. A. Gubbins who supervised me as a summer intern at R&D, Seagate Technology, NI, UK, in 2013 where I gained a much deeper understanding of my project. I also would like to thank Dr. P. S. Keatley who contributed significantly in setting up our Kerr microscope. All results in this chapter have already been published in Applied Physics Letters (Section 4.3), the IEEE Transactions on Magnetics (Section 4.4) and the Journal of Applied Physics (Section 4.5).

### **4.1 Introduction**

As has already been mentioned in Chapter 1, heat assisted magnetic recording (HAMR) is a promising way to push the superparamagnetic limit further. Since the fundamental design of HAMR writer wouldn't be much different from the current hard disk drive (HDD), it is still worth understanding the dynamics within HDD and optimizing its design. At the same time, due to the issues that HAMR faces mentioned in Chapter 1, it would be benefited to understand the hard drive writing process better. In this chapter, I will discuss my results on the magnetization dynamics of HDD writer yokes. I will first introduce the principles of operation of the HDD, discuss some issues that currently remain unresolved today, and then move on to the experimental results acquired by TRSKM.

## 4.2 Principle of HDD operation

Nowadays, hard disk drives record information by a technique known as ‘perpendicular magnetic recording’ (PMR) that was first proposed by Iwasaki<sup>52</sup>. A comparison of PMR and longitudinal magnetic recording (LMR) is shown in figure 4.1, where (a) shows the operation of a perpendicular head while (b) shows the operation of a longitudinal head. As is shown in figure 4.1(a), a group of coil winding(s) generate a magnetic field to magnetize the writer yoke. The magnetic flux generated within the writer will be concentrated through a tapered region or confluence region shown in figure 4.2 in order to generate the writing field in a very small area (~20~40nm). The soft underlayer acts as a magnetic flux return path in order to form a closed magnetic path from the writer pole to the return pole. Therefore, the field that writes the information is the ‘gap field’, which has a maximum value of  $4\pi M_s$ <sup>53</sup>, where  $M_s$  is the saturation magnetization of the writer pole. The magnetization within the recording media points either up or down. The LMR head writes the information using stray field, shown in figure 4.1(b), the maximum field delivered to the media being only about  $2\pi M_s$ , which is half the value for PMR. At the same time, since the magnetization within the media either points left or right, the demagnetizing energy of the written bits is greater. Therefore the stability of the written information is less good than for the PMR configuration. For PMR, the greater confinement of the ‘gap’ field permits a much higher recording density without shrinking the volume of each recording bit, which has greater length perpendicular to the plane of the disk. In addition, the enhanced write field also allows the use of media with higher anisotropy and coercivity, permitting further increases in recording density with acceptable thermal stability.

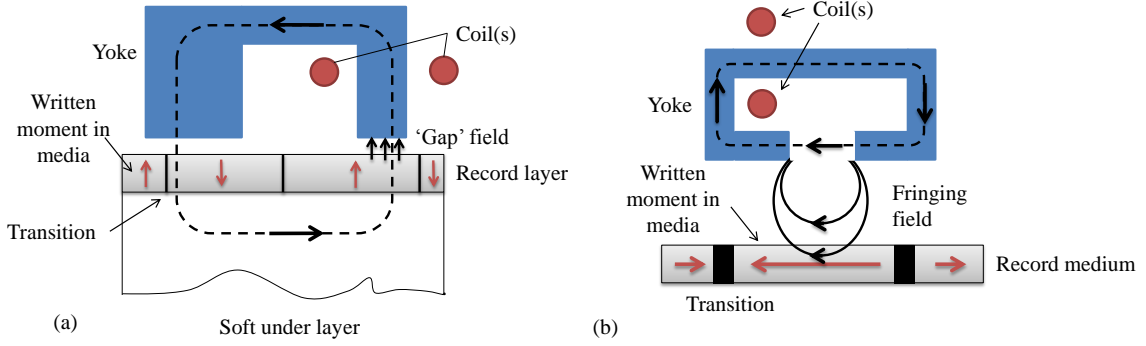


Figure 4.1. (a) Sketch of the perpendicular magnetic recording configuration. (b) Sketch of longitudinal magnetic recording configuration. (Re-made from reference 53).

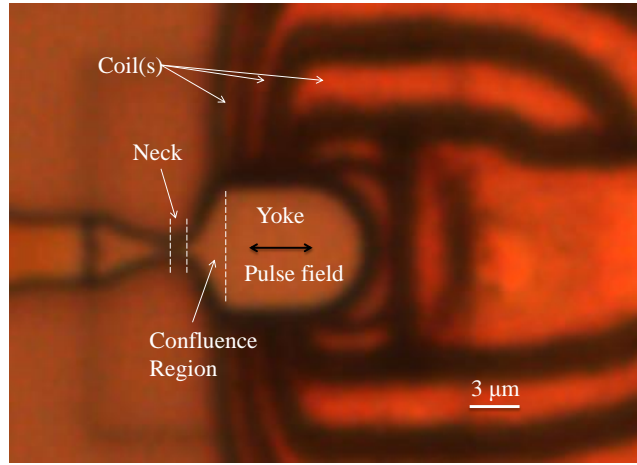


Figure 4.2. Wide field microscope image of the writer designed for TRSKM.

#### 4.2.1 Writing Physics

It is not the aim of this thesis to go into every detail of the design and physics within a HDD, rather the motivation of this study is to understand the magnetization dynamics within the writer during the writing process.

The typical shape of a yoke of a single pole head (SPH) is shown in figure 4.2, for a partially built writer that was designed specifically for TRSKM measurements. The cross section of a SPH is shown in figure 4.3. The yoke and the writing pole are excited by coil windings which generate the magnetic field to magnetize the yoke. The pole piece is usually designed to have a higher

permeability than the yoke, so that the magnetic flux generated within the yoke can easily propagate into the writing pole. The leading shield prevents the stray field from the yoke from affecting the media. The front shield has a similar function as well. However, in the operation of a real HDD, the permeability of the yoke is frequency dependent, and the performance of the shield cannot be understood in terms of its static permeability alone. The relaxation behaviour of the writer is also critical since increased data rates require the magnetization within the recording head to follow the driving field, avoiding erase after write<sup>54</sup> (EAW) phenomena. Previous studies<sup>55~61</sup> have been performed in order to address the rise time of the writing field and the remnant field within the tip region. However, since the yoke, which conducts the magnetic flux<sup>62</sup> into the confluence and tip region by a process of ‘flux beaming’ proposed by Michael Mallary in the 1980s, has a large influence on the writing field, improved understanding of how the dynamics within the yoke affects the writing field is needed to optimize writer design. In this thesis studies were performed on partially built writers that contained only the yoke and underlying pancake coil as shown in Figure 4.2.

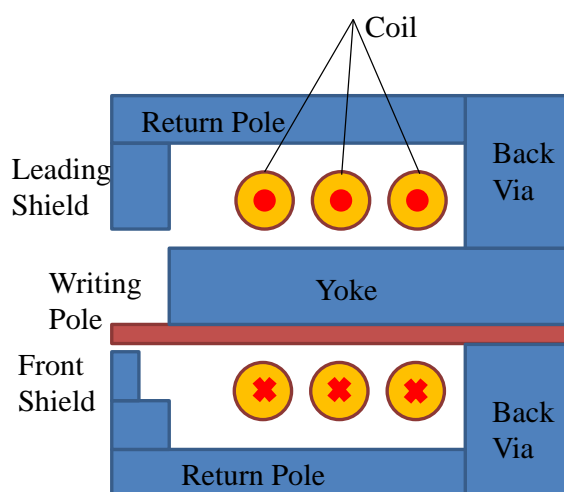


Figure 4.3. Schematic cross section of a perpendicular writer structure.

#### 4.2.2 Conduction of the flux

Mallary predicted<sup>62</sup> that flux is conducted via small angle magnetization rotation instead of domain wall motion. His experiment showed that a long strip of thin film Py still has some permeability loss as the driving field frequency increases after the skin effect has been removed. But for sheet films or thicker films (thicker than  $2.9 \mu m$ ), there is no such permeability loss. He postulated that the during high frequency excitation, a small angle Néel wall is created between the center region and the edge region of the strip, because only the magnetization within the center of the strip rotates during the excitation. The dashed line in Figure 4.4 (b) shows where the small angle Néel wall is created when a high frequency driving field is applied along the  $x$  direction.

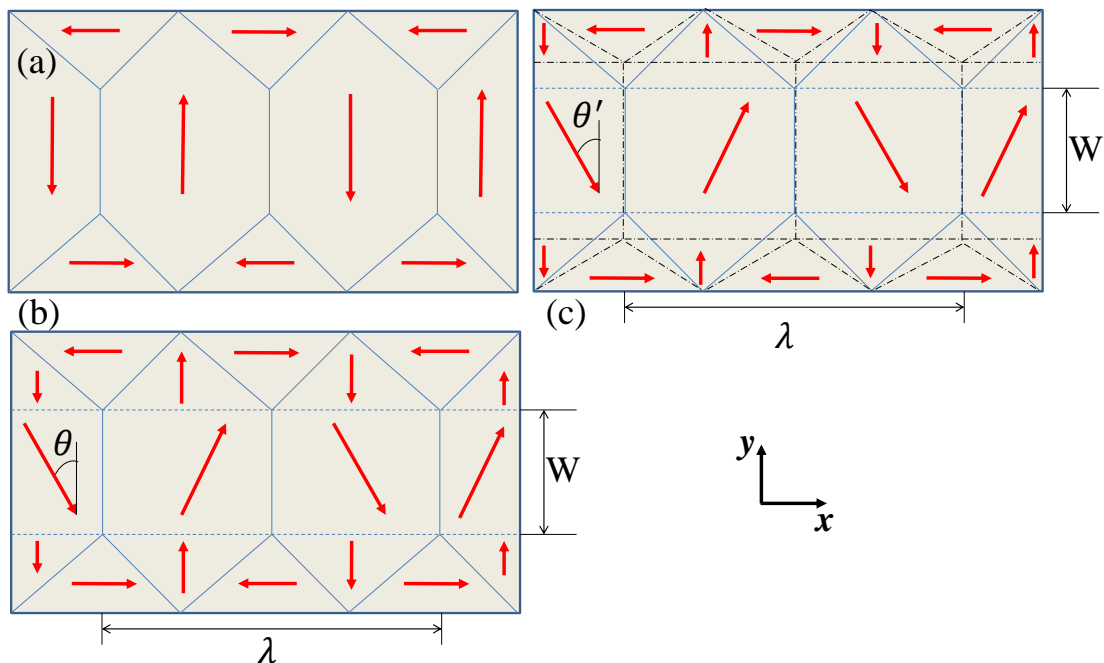


Figure 4.4. A Py strip used to conduct flux. (a) shows the domain configuration before excitation, while (b) shows the response to high frequency excitation. The dashed line denotes the Néel wall created during the excitation. (c) shows the spreading of the flux, the black dash-dot lines show the displaced domain walls.

The magnetic free energy associated with the creation of the wall has a number of contributions. The magnetostatic energy (per unit length per unit thickness of the strip film) due to the free magnetic poles at this wall has the form

$$E_M \approx C\theta^4, \quad (4-1)$$

where  $C$  is a constant. This is because the resulting free pole magnetic surface charge density is given by

$$\sigma = \pm M_s(1 - \cos \theta) \approx \pm \frac{1}{2}M_s\theta^2, \quad (4-2)$$

if  $\theta$  is very small, where  $M_s$  is the saturation magnetization. Since  $E_M \propto \sigma^2$ ,  $E_M \approx C\theta^4$ . The exchange energy per unit length and thickness has the form

$$E_{ex} = 2A\theta^2/\delta, \quad (4-3)$$

where  $A$  is the exchange constant and  $\delta$  is the wall thickness.

The anisotropy energy in the center region per unit length per unit thickness is

$$E_A = (K_\mu \sin^2 \theta)(W - \frac{4\delta}{3}), \quad (4-4)$$

where  $W$  is the width of the center region, and  $K_\mu$  is the anisotropy constant.

The background field energy is:

$$E_B = -(H_B M_S \sin \theta)(W - \delta), \quad (4-5)$$

where  $H_B$  is the background driving field.

By minimizing the sum of equations (4-3), (4-4) and (4-5),  $\delta$  is found to be

$$\delta = \sqrt{3A/K_\mu}. \quad (4-6)$$

For Permalloy, the value of  $\delta$  is  $\sim 0.3 \mu m$ . Therefore, the domain wall width and the exchange energy have only a very small effect on a writer that is usually microns wide. For example the devices studied in this thesis have width of  $6 \mu m$ , therefore, the wall width is only 5% of the width of the yoke. From (4-1), (4-3) and (4-4) we can see that for a very small rotation angle, the magnetostatic energy ( $\sim \theta^4$ ) (wall energy) will be very small compared with the anisotropy energy ( $\sim \theta^2$ ), so in the high frequency and small rotation regime, the flux is conducted by a small angle rotation of the center domains without displacement of the edge domain walls shown by the dashed line in the lower panel of figure 4.4.

From equation (4-1) and (4-4) we can see if  $E_M = E_A$ , which is the condition for the magnetostatic and anisotropy energies to be equal, the rotation angle would be:

$$\theta_c \approx \sqrt{\frac{K\mu W}{c}}. \quad (4-7)$$

For permalloy  $\theta_c \approx 10^\circ$ , so flux spreading occurs if the driving amplitude is large enough to rotate the magnetization by  $10^\circ$  in Py. As shown in figure 4.4(c), the spreading of the flux involves more domain wall motion, leading to a more complicated dynamic behaviour, which could potentially lead to a longer relaxation time for the writing field and hence erase after write (EAW) problems<sup>54</sup>.

Kasiraj<sup>48</sup> et al. at IBM first observed ‘flux beaming’ within a recording head by scanning Kerr microscopy in 1986, confirming that flux is conducted by rotation of magnetization near the center of the head with the closure domains at the edge of the head undergoing little or no magnetization rotation. Furthermore,

they also found that increasing the driving frequency would further confine the flux within the center of the yoke, while increasing the driving amplitude would spread the flux due to larger domain wall displacement towards the edges of the yoke. Resolving the magnetization dynamics within the writer by time resolved magneto-optical Kerr effect measurements was impossible at the time. However it is very important that we gain insight into the local magnetization dynamics within different writer structures in order to understand how the design affects the rise and fall times of the writing field. Freeman<sup>63</sup> et al. used time resolved MOKE system to explore the dynamics of a writer at its pole tip, but the presence of the shields did not allow the laser to probe the yoke. In our work, partially built writers without shields are studied by time and vector resolved scanning Kerr microscopy, in which, by making use of a vector bridge detector, signals from all three Cartesian components of the magnetization are recorded simultaneously, allowing us to fully address the dynamics within the writer yokes.

### 4.3 Study of the magnetization dynamics within a multi-layered yoke with three coils

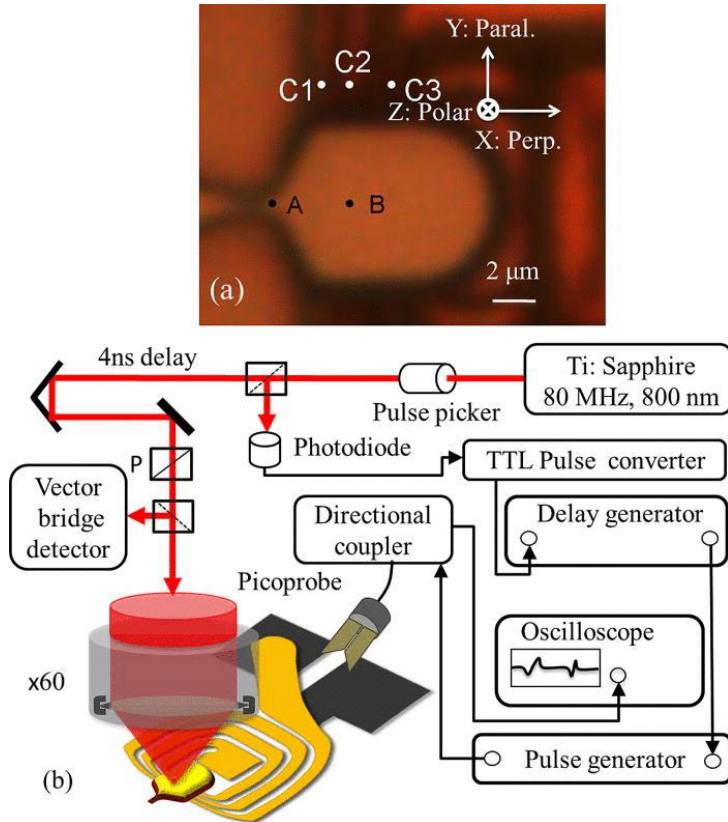


Figure 4.5. (a) Wide field optical microscope image of the sample. C1, C2 and C3 are the coil turns. A and B are positions where time resolved signals were recorded. (b) The experimental set-up.

In this study, writer structures with a multilayered yoke were excited with high-frequency current waveforms of different polarity, and with different bias magnetic fields to empirically determine and understand the static and dynamic states of the writer magnetization under conditions similar to those experienced in a hard disk drive. The sample consisted of a partially built writer structure with yoke and pole tip formed from 4 repeats of a NiFe(~1nm)/CoFe(50 nm) bilayer designed to possess a high moment and low coercive field. The geometry of the yoke, pole tip, and coil windings is shown in figure 4.5(a). The three coil turns, labeled C1, C2 and C3, lie under the yoke and generate an in-plane driving field when current is applied. The schematic layout of the TRSKM

specific to this study is shown in figure 4.5(b). The Ti: Sapphire mode locked laser generated a train of 80MHz laser pulses with 800nm wavelength. After the beam passed through the pulse picker, its repetition rate was reduced to 1MHz in order to synchronize to the pulse generator that had maximum repetition rate of 1 MHz. The 1 MHz laser pulse train was then sent into a 50/50 non-polarized beam splitter (BS). After the BS, one beam was directed into the  $\times 60$  objective lens and was normally incident on the sample which was placed on a piezoelectric scanning stage. The beam reflected back from the sample, was directed into a vector bridge detector<sup>46</sup> which simultaneously detected the total reflected optical intensity (refl.), the in-plane magnetization components parallel (paral.) and perpendicular (perp.) to the bias field, and the out of plane magnetization component (polar). The latter three outputs from the detector were input into three lock-in amplifiers so that phase sensitive detection could be used to extract the change in magnetization induced by the excitation waveform. Due to the optical skin effect, only the top 20 nm of the device was sensed. Another beam after the BS was collected by a fast photo diode to convert it into an electrical signal. The electrical signal was then sent into a TTL pulse converter to smooth the electrical signal into a TTL signal. This was then used to trigger a computer-controlled digital delay generator. The TTL signal output by the delay generator was used to trigger a pulse generator that can generate pulses of up to 40 V in amplitude and 2 ns in width. The time delay between the pump and the probe was controlled by either the digital delay generator or the retro-reflector. In this measurement, the pulse used to excite the writer had 1.6 ns duration and 11.2 V amplitude, since larger values led to signals that had noticeable stochastic character<sup>63</sup>. A bias magnetic field was applied in the plane of the yoke and perpendicular to its axis of symmetry.

Measurements were first performed without a static bias magnetic field. Figure 4.6(a) shows time resolved signals acquired from position B in Figure 4.5(a), while Figure 4.6 (b) and (c) show dynamic images taken at the time delays indicated in Figure 4.6(a). While the magnetic images appear less sharp than the reflectivity image, they were acquired simultaneously, suggesting that the dynamic magnetization varies gradually with position. The direction of the pulsed current  $I_p$  is shown in each panel. The polarity of the time resolved signals, and the contrast within the perpendicular and polar channels of the dynamic images, is seen to reverse with the polarity of the pulsed current as expected. However, in Figure 4.6(a) the parallel channel in the upper panel shows a constant value during the whole 4 ns scan, while a clear time dependent response to the pulsed current is seen in the parallel channel in the lower panel. The shapes of the signals observed in the perpendicular and polar channels also show definite but less dramatic differences between the upper and lower panels, for opposite current polarity. Surprisingly, the contrast in the polar channel, within Figures 4.6(b, c), shows the same polarity to the left and right of the coil windings even though the driving field is out of plane with opposite polarity. The polar contrast above the coil windings is somewhat weaker since the driving field lies in the plane. Comparison of Figures 4.6(b, c) reveals an almost identical distribution of contrast within the parallel channel as the current polarity is reversed. This can be understood if the static magnetization forms stripe domains with magnetization alternating between the up and down directions in adjacent domains. The magnetic field generated above the coil windings lies parallel to the symmetry axis of the yoke, and points to the left or right depending upon the polarity of the current. In either case the magnetization attempts to rotate parallel to the horizontal field, leading to a

similar change in the vertical magnetization component regardless of the current polarity. Since the parallel channel images show the change in the vertical magnetization component, light and dark stripes correspond to the magnetization rotating from +/-Y directions. The parallel channel images at negative time delay, 0.3 ns in Figure 4.6(b) and 0.34 ns in Figure 4.6(c), show weaker contrast at the right compared to the center of the yoke, suggesting a significantly different relaxation behavior at different positions within the yoke. Strong contrast is also observed in the parallel channel within the tip region at negative delay in Figure 4.6(b), but not in Figure 4.6(c), indicating a different equilibrium state and different relaxation behavior within the tip region for different current polarities.

The perpendicular channel in Figure 4.6(b) shows no contrast within the tip region throughout the 4 ns time scan. However, strong contrast appears within the tip region in the perpendicular channel in Figure 4.6(c) from 1.04 ns onwards and is still present at 3.46 ns after the driving current has been switched off, suggesting a potential EAW problem. Taken together with the contrast observed in the parallel channel in Figure 4.6(b) and (c), this indicates a complex equilibrium state magnetization distribution and tip response for different current polarities. The perpendicular channel images at 1.9 and 2.6 ns in Figure 4.6(b) and 1.04, 1.66, 2.28 and 2.7 ns in Figure 4.6(c) show that the maximum contrast appears within the upper and lower parts of the yoke respectively. This indicates that the equilibrium state magnetization is not exactly vertical, but is canted so as to lie parallel to the edge of the yoke within the confluence region. In Figure 4.6(b), where the current flows along -Y, the maximum contrast appears in the upper part of the yoke because the static magnetization is canted towards the right and so must rotate further to align

with the driving field that points to the left. By similar reasoning, in Figure 4.6(c), where the driving current instead flows along +Y, the driving field points to the right, and the magnetization must rotate through a larger angle in the lower part of the yoke, leading to stronger contrast in the perpendicular channel. The perpendicular channel in Figure 4.6(b) at 3 and 3.5 ns shows a dark horizontal band reminiscent of “flux beaming” superimposed on a “chequer board” type background. This occurs after the driving field has begun to fall, suggesting a different rate of relaxation across the area of the yoke. A completely different relaxation behavior is observed in Figure 4.6(c). The central horizontal band and chequer board background are not observed, and strong contrast is instead observed in the lower part of the yoke. Based on the dynamic images from the perpendicular and parallel channels, a putative equilibrium state that occurs during the pulse cycling has been sketched in Figure 4.7(a). The yoke contains two closure domain structures. The magnetization within the large stripe domains lies principally in the vertical direction as a result of induced anisotropy from wafer-level processing. The magnetization within each domain is canted differently within the upper and the lower parts of the yoke so as to be parallel to the edges at the right and left hand ends of the paddle. Proposed metastable equilibrium states within the tip region during repeated pulsing are inset in Figure 4.7(a) and are seen to depend upon the current polarity.

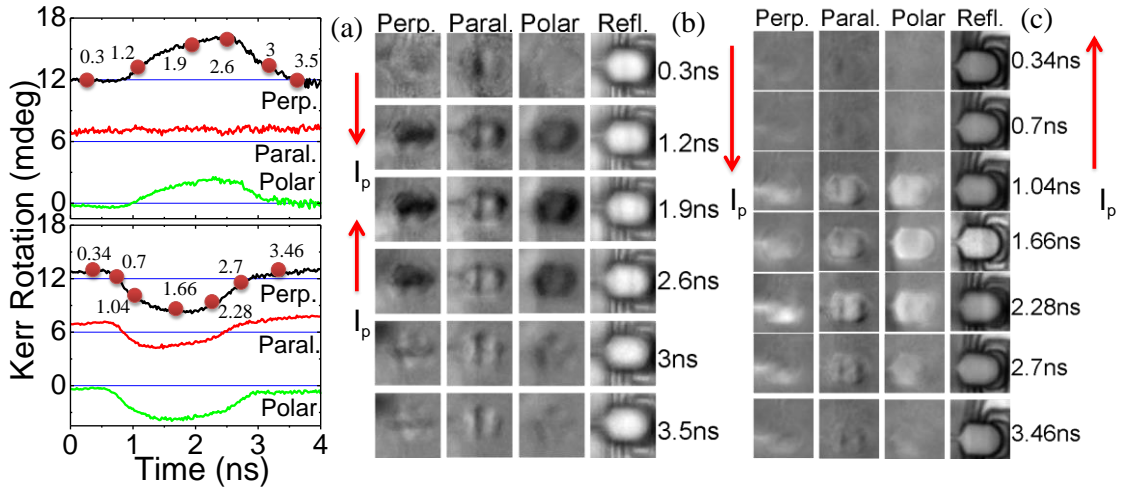


Figure 4.6. (a) Time resolved signals acquired from position B in Figure 4.5. (a). The direction of the pulsed current  $I_p$  within the current windings for the upper and lower panel is shown. (b) and (c) Dynamic images obtained from the 4 detector channels defined in the main text with  $I_p$  flowing downwards and upwards respectively. For a particular channel the contrast is normalized to the maximum Kerr amplitude observed within that time series. Black/white corresponds to the dynamic magnetization lying in the  $-/+ z$ -direction,  $-/+ x$ -direction, and  $+/- y$ -direction for the polar, perpendicular, and parallel channels respectively. The Cartesian axes are defined within Figure 4.5 (a) and shown above the columns in panels (b) and (c). 0.3 and 0.34 ns are the negative delay in (b) and (c) respectively.

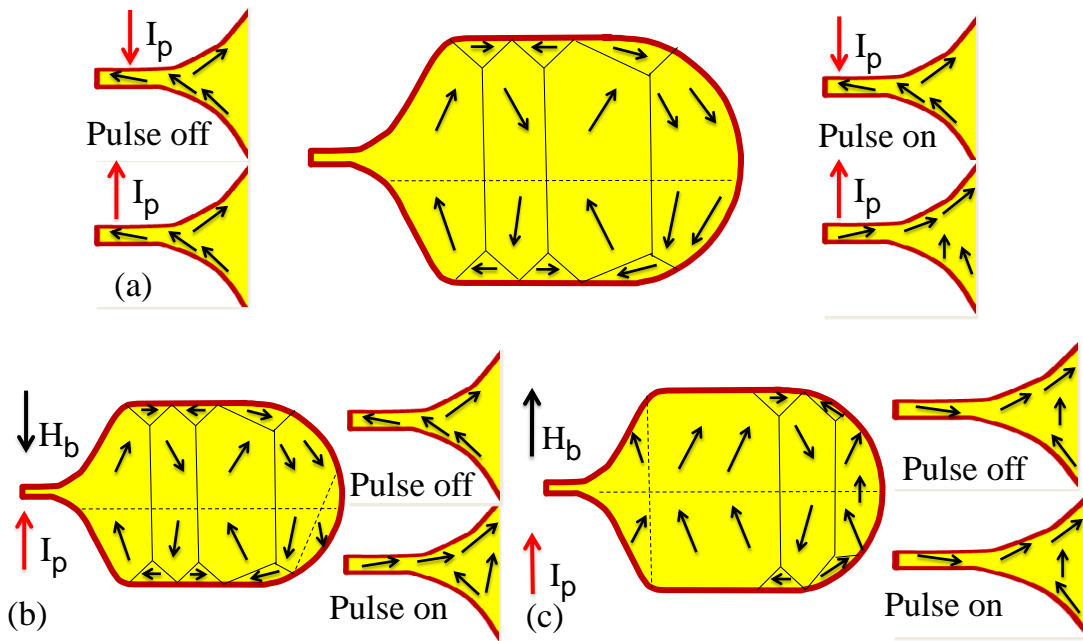


Figure 4.7. Sketches of proposed equilibrium states. The dashed lines delineate regions with different canting direction. There is no bias field  $H_b$  applied in (a), while  $H_b$  is applied in the  $-Y$  and  $+Y$  directions in (b) and (c) respectively. Metastable states of the tip during pulse cycling are inset with the polarity of the pulsed current  $I_p$  shown.

To obtain a better understanding of the equilibrium state and relaxation behavior, a bias field of 200 Oe was applied orthogonal to the symmetry axis of the yoke. Figure 4.8(a) shows the time resolved signals obtained from position B for both field polarities. The direction of the current was along +Y axis in all cases. Surprisingly, the strongest contrast is observed within the lower part of the yoke in the perpendicular channel in both cases, and a stripe domain structure continues to be observed within the parallel channel. This indicates that the 200 Oe bias field is insufficient to make the equilibrium state uniform.

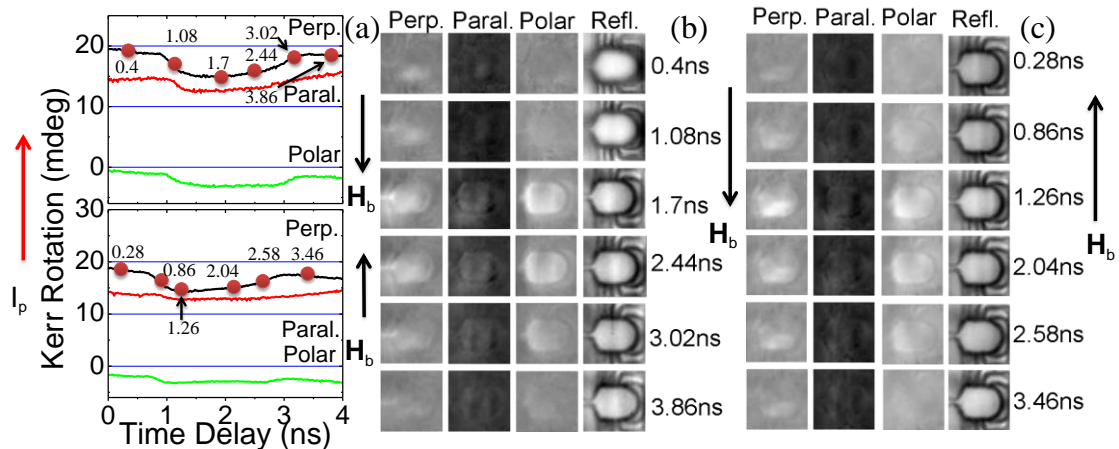


Figure 4.8. (a) Time resolved signals acquired from position B in Figure 4.5(a). The direction of the bias field  $H_b$  for the upper and lower panel is shown. (b) and (c) Dynamic images obtained from the 4 detector channels (X: Perp., Y: Paral., Z: Polar, and Refl.) with  $H_b$  along -/+Y axis. For a particular channel the contrast is normalized to the maximum Kerr amplitude observed within that time series. Black/white corresponds to the dynamic magnetization lying in the -/+ z-direction, -/+ x-direction, and +/- y-direction for the polar, perpendicular, and parallel components, respectively. The Cartesian axes are defined within Figure 4.5(a) and shown above the columns in panels (b) and (c). 0.4 and 0.28 ns are the negative delay in (b) and (c) respectively.

The perpendicular channel in Figure 4.8(b) shows clear contrast within the tip region at 1.7, 2.44, 3.02 and 3.86 ns, but the contrast within the same region is very weak for the perpendicular channel in Figure 4.8(c).

The parallel channel signals in Figure 4.8(a) show a significant offset that appears as a dark background in the parallel channel images of Figure 4.8(b-c). This is most likely the result of mechanical vibration since the bias field exerts a force upon the coil windings when current is supplied. Figure 4.8(c) shows a black stripe parallel to the bias field at the right end of the yoke for the full range of delay, and a weaker dark region close to the tip. Within Figure 4.8(b) the distribution of contrast is more similar to that in Figure 4.6(b) and (c) with 2 stripes along the Y-axis appearing at the center and right hand end of the yoke. The polar channel images within Figure 4.8(b-c) are almost identical, indicating that the polar component is not affected by the direction of the bias field. Based upon the images recorded in the perpendicular and parallel channels, sketches of the putative equilibrium states that occur during the pulse cycling are presented in Figure 4.7(b) and (c). The 200 Oe bias field is insufficient to produce a uniform equilibrium state. A stripe domain pattern is still observed and the magnetization within the upper and lower parts of the yoke continues to cant in different directions. However when the bias field is along +Y direction, as in Figure 4.8(c), there are only three domains with anti-parallel magnetization within the yoke. Again the magnetization within the tip region does not simply follow the direction of the applied bias field, but occupies a meta-stable equilibrium state that is dependent on both the pulse polarity and the applied bias field. The blurriness of the dynamic images may indicate that the yoke dynamics are partly stochastic in character.

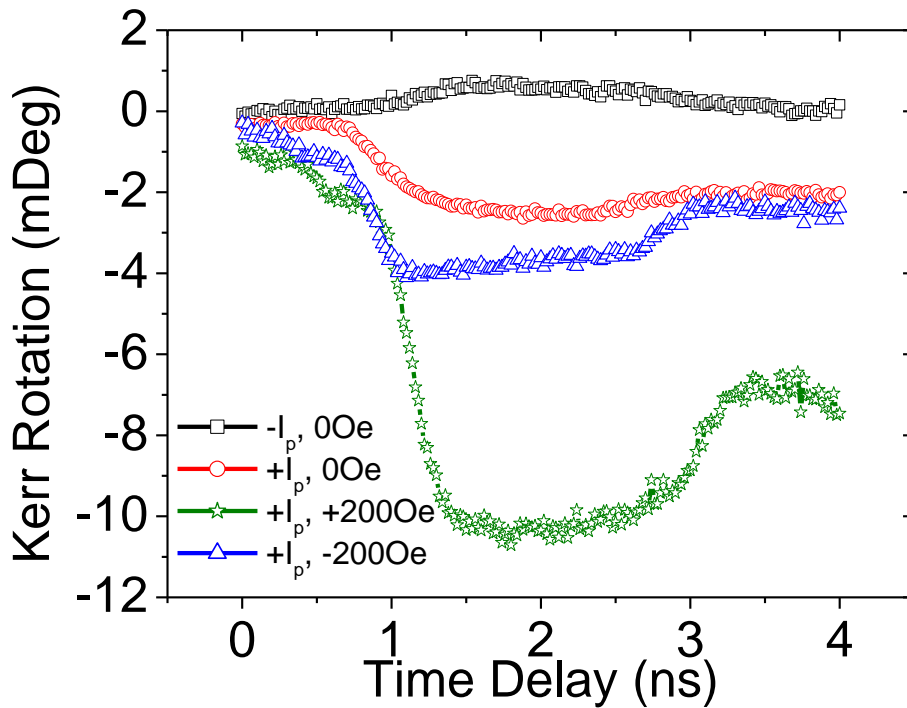


Figure 4.9. Perpendicular component of the time resolved signal acquired at position A. The legend indicates whether the direction of the driving current is along +Y ( $+I_p$ ) or -Y ( $-I_p$ ) and whether the bias field points along +Y (+200 Oe) or -Y (-200 Oe).

Figure 4.9 shows the perpendicular component of the time resolved signal acquired at position A in Figure 4.5(a), which is located deep in the confluence region, both with and without bias field and for driving currents of different polarity. When there is no bias field, the amplitude of the perpendicular magnetization component is greater when the driving current flows along +Y (red curve), but the magnetization relaxes less effectively after the current pulse has passed. When the current flows upwards, the response is larger when the bias field points to +Y (+ 200 Oe, blue curve) rather than -Y, (-200 Oe, green curve), and the response is larger with rather than without the bias field. This behavior is consistent with the contrast seen within the tip region for the perpendicular channel in Figure 4.8(b) and (c) and confirms that the direction of the applied bias field has a significant effect upon the dynamics of the writer. Since position A is close to the air bearing surface (ABS), it seems likely that

very different head fields will be obtained by changing the polarity of either the driving current or the bias field. The perpendicular magnetization component does not appear to relax fully after the current has passed for any of the four curves, suggesting that EAW may be a significant problem.

In summary, the magnetization dynamics within a multilayered writer yoke have been clearly resolved in TRSKM measurements. The perpendicular and parallel channel dynamic images suggest that, in the absence of a bias field, the yoke supports a stripe domain equilibrium state while the equilibrium state of the tip during pulse cycling is metastable and depends upon the polarity of the driving current. A bias field of 200 Oe is insufficient to induce a uniform equilibrium state and a modified stripe domain configuration continues to be observed. The dynamics observed within the tip region suggest that the equilibrium state during repeated pulsing depends upon the polarity of both the driving current and the bias field. Different combinations of bias field and current polarity lead to different dynamics deep within the confluence region; in agreement with recent modeling work<sup>61</sup>. These data suggest that the magnetization dynamics throughout the yoke can vary significantly depending on the current polarity and any bias or anisotropy field.

#### **4.4 The effect of the coil positions**

As stated in the previous section, by varying the polarity of the bias field and the pulse, different equilibrium states and writing fields can be achieved, suggesting a strong influence of the yoke upon the writing field. In this section, the effects of locating a single coil at different positions under the yoke are explored.

The experimental set up is shown in figure 4.10(a). It is similar to that used in the last section except that an additional DC bias current of opposite polarity to that of the pulse is applied in order to achieve a quasi bi-polar driving condition. Three samples have been measured that have the same geometry as in the last section except there is only one coil excited within each device, shown in figure 4.10(b).

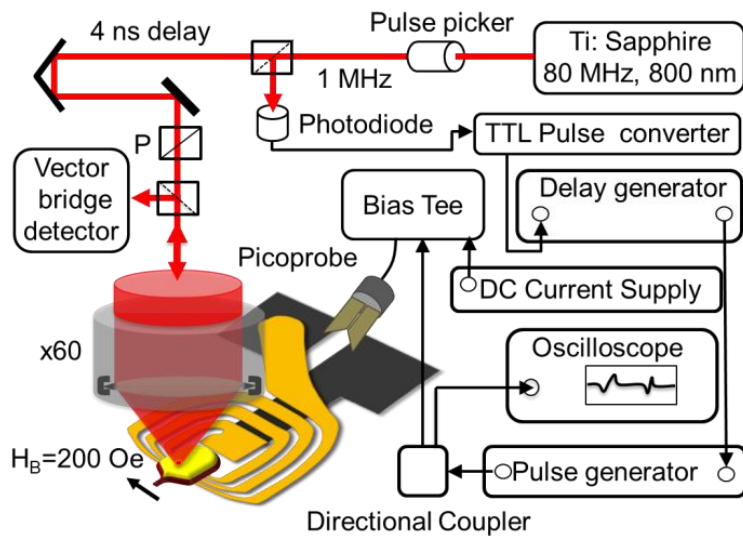


Figure 4.10. (a) Schematic of the time resolved scanning Kerr microscope (TRSKM) set up

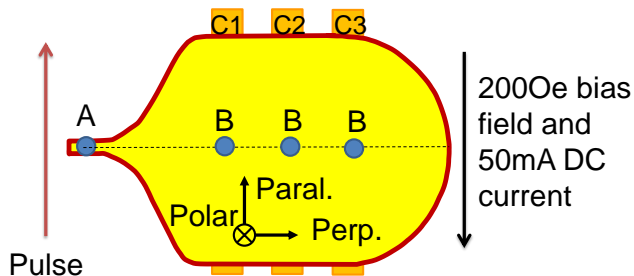


Figure 4.10. (b) Schematic of the device. Time resolved measurements were made at positions A, deep in the confluence region, and B above each active coil winding. Arrows denote the magnetization components sensed by the polar, parallel and perpendicular channels of the detector and the directions of applied electrical pulse, DC current, and bias field.

In a finished writer position A would be very close to the air-bearing surface (ABS). Therefore the amplitude and time dependence of the write field should

closely follow those of the perpendicular magnetization component at this point. The normalized Kerr rotation from the perpendicular channel measured at position A, is shown in Fig. 4.11(a). The devices are labeled left, right and centre according to the location of the active coil winding. While the rise time is insensitive to the position of the active winding, the signal relaxes most quickly when only the centre coil turn is connected (red curve). Fig. 4.11(b) shows the same signals without normalization and offset for clarity. The signal is largest and smallest when the centre and left coils respectively are active. This confirms the need for the rear part of the yoke to generate flux that can propagate into the confluence region.

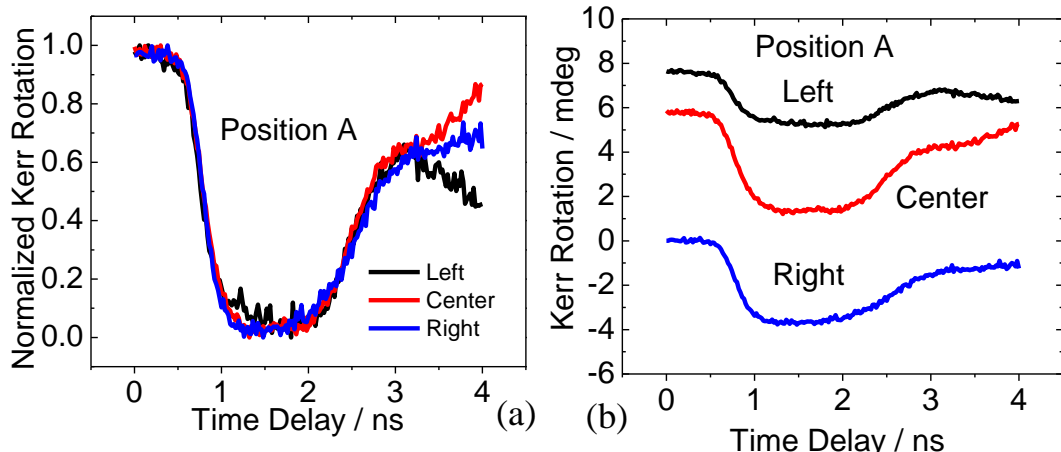


Figure 4.11. (a) Normalized Kerr rotation from the perpendicular channel measured at position A. (b) The signals without normalization from (a) offset in the vertical direction for clarity.

Fig. 4.12(a) shows the normalized Kerr rotation from the perpendicular channel measured at position B, the point where the symmetry axis of the yoke intersects the centre of the active coil. A constant background has been subtracted so that the initial sections of each signal are overlapped. The signals from the three devices begin to rise in a similar manner, but that from the device with the central coil connected is seen to saturate and begin to relax before the

others. Figure 4.12(b) shows the same signals without normalization and offset for clarity. The signal from the device with only the central coil turn connected has largest amplitude. Since the distance between the active coil winding and the upper surface of the yoke was the same in each device, and the same current pulse was delivered to each coil as evidenced by the form of the reflected waveforms, the same driving field is expected at position B in each case. The different response of the yoke observed at position B in each device is most likely due to the inhomogeneous character of the ground state, which arises due to the strong in-plane demagnetizing fields associated with the thick yoke structure. The ground state may in fact become meta-stable, being able to fully relax only in the 0.159 ms between bursts of pulses, and not within the 1000  $\mu$ s between successive pulses within each burst.

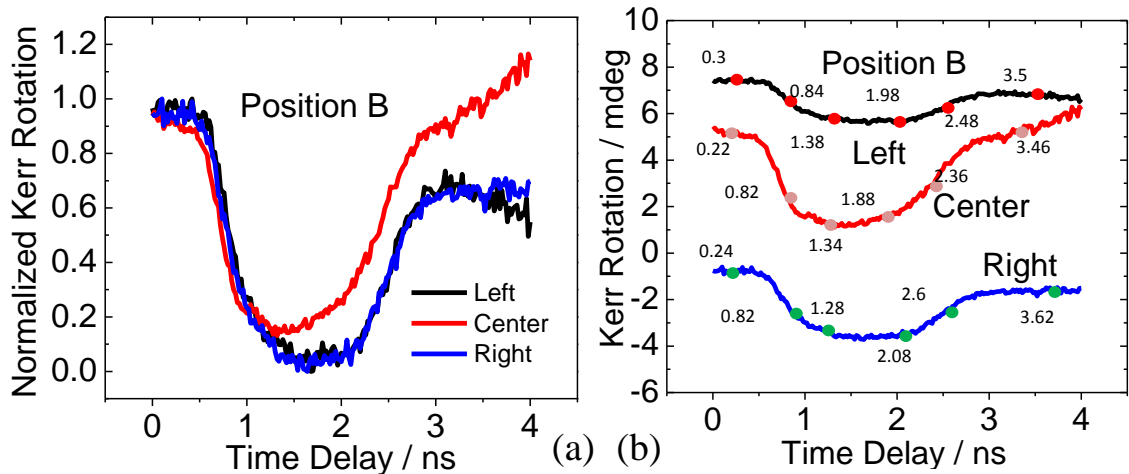


Figure 4.12. (a) Normalized Kerr rotation from the perpendicular channel measured at position B. (b) Un-normalized signals from (a) offset in the vertical direction for clarity. Symbols indicate the time delays at which dynamic images were acquired. 0.3, 0.22 and 0.24 ns are the negative delays of the left, center and right coils respectively.

The dynamic images in Figure 4.13 were acquired at the delay times indicated within Fig. 4.12(b) in order to better understand the time dependent signals

acquired from positions A and B. In each device the perpendicular channel images exhibit flux beaming, but the contrast is stronger when the center or right hand coil are connected. This is consistent with the observation of smaller time resolved signals at A and B when only the left hand coil was connected. The perpendicular channel image at 0.3 ns (negative delay) in Figure 4.13(a) shows almost no contrast, indicating a well-relaxed ground state. However its counterparts in fig. 4.13(b) at 0.22 ns and in fig. 4.13 (c) at 0.24 ns still show a flux beaming feature, suggesting that there is residual magnetic flux propagating into the confluence region and pole tip that may lead to EAW. The improved relaxation behavior in Figure 4.13(a) may occur because the left hand coil winding has less influence upon the ground state at the back (right hand end) of the yoke. However, as shown previously, the perpendicular magnetization component at position A and hence the write field is also smaller. The perpendicular channel image in Figure 4.13(c) shows reduced flux within the confluence region compared to its counterpart in Figure 4.13(b), reflecting the smaller driving field generated by the right hand coil within this region. The centre coil winding is therefore more effective in controlling flux propagation along the full length of the yoke.

The parallel component channel in Fig. 4.13(b) and (c) shows a black vertical stripe at the center of the yoke, while there is no such feature in Fig. 4.13(a), suggesting that different meta-stable ground states are established during repeated pulsing. Within Fig. 4.13(a), the parallel channel suggests a quasi-uniform ground state with static magnetization parallel to the bias field, while in (b) and (c), a stripe domain structure occurs with the magnetization of the central domain aligned antiparallel to the bias field. The parallel channel images in (b) and (c) acquired before the pulse arrives (0.22 ns and 0.24 ns

respectively) show some contrast at the position of this anti-parallel domain, again indicating remnant flux propagating through the yoke that may lead to EAW.

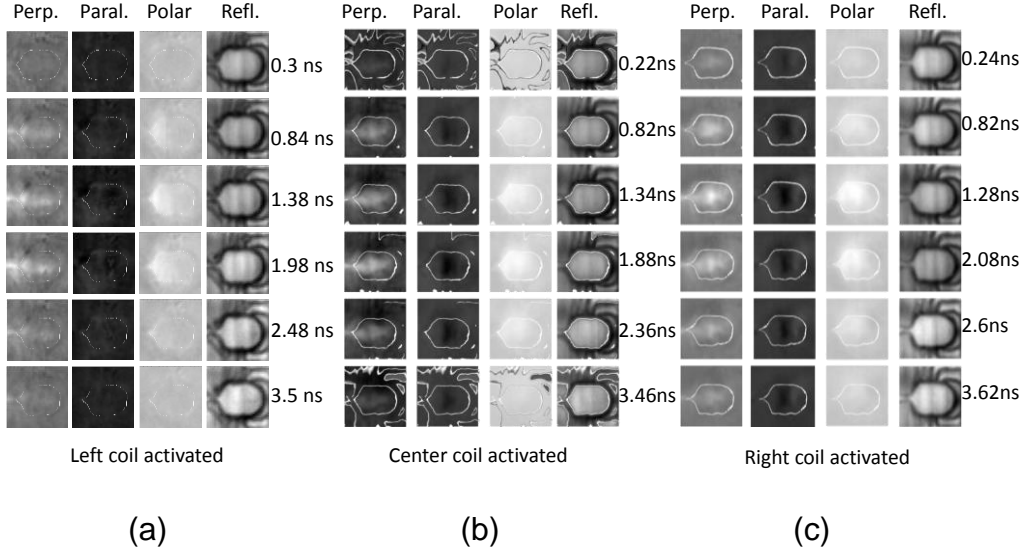


Figure 4.13. Time resolved scanning Kerr microscopy images of the changes induced in the parallel, perpendicular and polar magnetization components defined within Fig. 4.10(b). Three coil windings may be seen within the reflectivity images. The left, centre, and right hand coil windings are active within panels (a), (b) and (c) respectively. The first row of each column is the negative delay.

Surprisingly, the polar channel images of all three devices reveal a unipolar response over the entire area of the yoke, even though opposite contrast might be anticipated at opposite ends of the yoke due to the opposite polarity of the polar driving field on either side of the active coil winding. The polar channel also exhibits a large background for all three devices. This may be due to mechanical vibration induced by the force that the bias field exerts upon the coil windings when pulsed current is applied.

In summary, the time resolved perpendicular magnetization component signals show that while the amplitude within the tip depends upon the location of the active coil winding, the rise time does not. Dynamic images show that a coil

winding located at the center of the yoke is most effective in controlling flux propagation along the entire length of the yoke as well as directing flux into the confluence region. A coil winding placed close to the confluence region is most effective in controlling erase after write. These findings justify the use of multi-turn coil windings, which combine the benefits of placing a coil in each of these different locations.

#### **4.5 Bipolar pulse excitation of a synthetic antiferromagnetic yoke**

In the previous two sections, it was shown that yokes with different coil configurations can occupy different meta-stable states during pulse cycling. Pulses of similar amplitude but opposite polarity also caused the pole tip magnetization to exhibit changes of different amplitude, suggesting a complicated influence of the yoke dynamics upon the write field. All of these experimental studies were carried out with unipolar pulses, while a hard disk drive employs a bipolar waveform with positive and negative phases of similar amplitude<sup>61</sup>. To afford a more direct comparison with the performance of the writer in a hard disk drive, bipolar pulses have been used in time resolved scanning Kerr microscopy measurements performed on a partially built writer with a NiFe/CoFe(100nm)/Ru/NiFe/CoFe(100nm) synthetic antiferromagnetic (SAF) yoke structure. The SAF structure was designed in order to bias the magnetization within the yoke so that the writing field will switch off quickly after the driving pulse has gone.

The sample geometry, the experimental setup, and the input bipolar pulse are shown in figure 4.14. The experimental set up is similar to that in previous sections but without any bias field or DC current. In addition, a combination of two power dividers, a polarity switcher, and some cables of carefully selected

length were used to convert the unipolar output of the pulse generator into a bi-polar pulse. The resulting bi-polar pulse was delivered to the writer coil through a directional coupler as in the previous sections. More details about the bi-polar pulse generation can be found in the Appendix 1. The geometry of the writer measured in this section is the same as in section 4.3 except for the stack structure which is NiFe/CoFe(100nm)/Ru/NiFe/CoFe(100nm) with 3 coil windings connected beneath it.

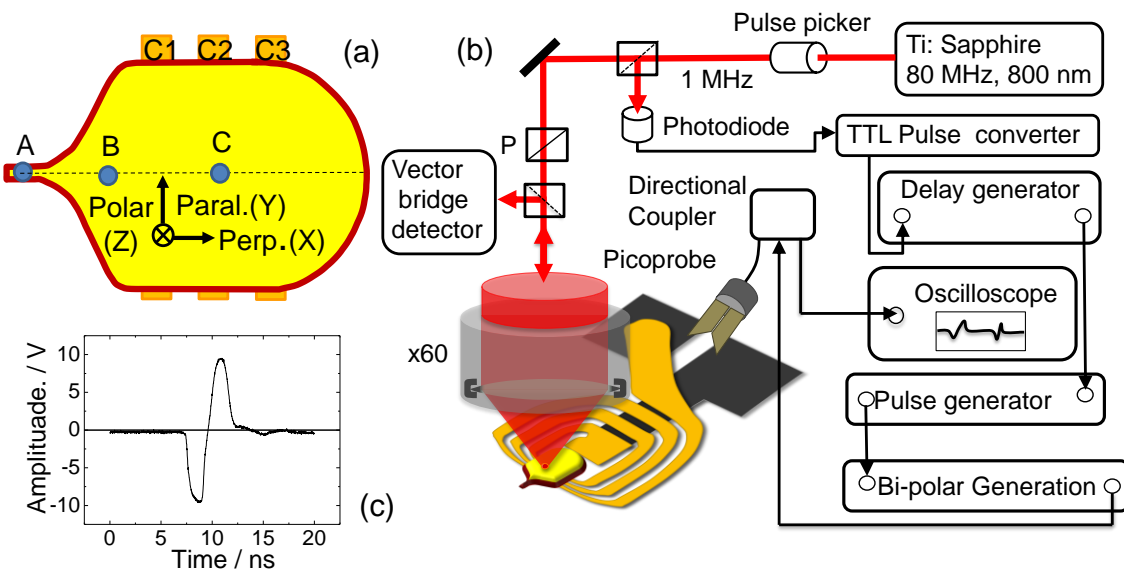


Figure 4.14. (a) Sketch of the device and three positions where time resolved signals were acquired: A, deep in the tip region; B, on the symmetry axis and at the edge of the confluence region; C, at the intersection of the symmetry axis and the C2 coil. The three components of the magnetization are labelled perpendicular (X), parallel (Y) and polar (Z). (b) The time resolved scanning microscopy setup. (c) The bipolar pulse delivered to the coil.

Figure 4.15(a) shows the normalized perpendicular (X) component of the dynamic magnetization at positions A, B and C. An offset was subtracted prior to normalization so that the rise and fall times may be more easily compared. The dashed line shows the normalized driving current recorded by the oscilloscope. Figure 4.15(b) shows the same signal as in Figure 4.15(a) but

without the normalization and offset subtraction. Unsurprisingly, since position C is directly above the center coil, of the 3 positions, the magnetization dynamics at C follow the driving current most closely. In fact the normalized driving current and signal from position C are closely overlapped except between 4.5~5.5ns, where the signal at C leads the driving current, and at 5.5ns where the signal overshoots the driving current. These differences are possibly the result of secondary pulses caused by impedance mismatches between the writer coil, a long coplanar strip structure running from the device to the edge of the wafer, and the high frequency probe that provides a transition to coaxial cable. The shape of the normalized time resolved signal at position A is similar to that at C, following it closely when the driving pulse is rising, but then lagging behind on the falling edge. This suggests that the yoke dynamics only dominate the dynamics within the pole tip, and hence the write field, when the driving pulse is rising. The signal obtained at position B has smaller amplitude. While the magnetic field generated by the coil lies in the plane of the yoke at position C, it is canted out of plane at position B, and so a smaller in-plane deflection of the magnetization is to be expected. A larger signal is obtained at A due to the concentration of flux in the confluence region as intended. The signal at A has a negative offset while those from B and C have positive offsets suggesting that full relaxation is not achieved within 1  $\mu$ s and has different character at different positions within the writer. The signal at position A also shows a response of different amplitude for different polarities of the driving current. This asymmetry is consistent with results from section 4.3, in which a writer was tested separately with unipolar pulses of opposite polarity.

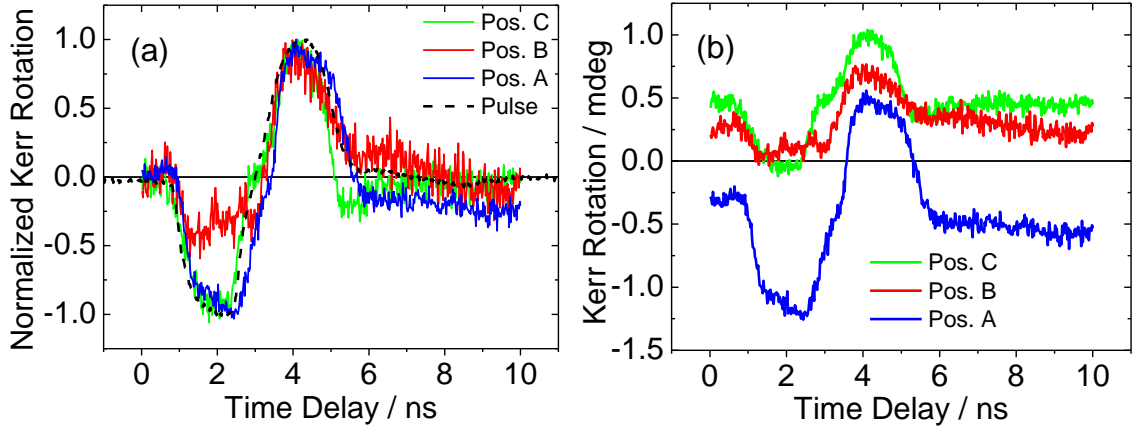


Figure 4.15. (a) The normalized perpendicular (X) magnetization component at position A, B and C. An offset was subtracted prior to normalization. (b) The signals in (a) prior to offset subtraction and normalization.

In order to obtain a better understanding of the dynamics of the writer, the time resolved images in Figure 4.16 were acquired at delay times corresponding to points of interest in the perpendicular channel signal from position C, which is shown in Figure 4.16(b). The borders of the yoke have been highlighted so as to guide the eye.

The synthetic antiferromagnetic yoke structure was intended to produce a single domain static ground state. However, during pulse cycling the yoke can also occupy a meta-stable equilibrium state depending upon the driving pulse configuration. The dynamic images suggest the formation a multi-domain equilibrium state. The perpendicular channel images reveal a light vertical stripe close to winding C3 up to 3.58 ns delay, after which additional black contrast appears around the stripe before quickly fading again. The parallel channel images also show a black stripe at a similar but not quite identical position that expands and then contracts again with increasing time. The polar channel images show similar, but again not identical, features to the parallel channel, supporting the idea that the yoke is sufficiently thick that the magnetization can

cant out of plane to some extent in a truly 3 dimensional magnetization distribution. In addition there is a more uniform variation in contrast superimposed when the pulse is present. The field generated by the coil should favor contrast of opposite sign at opposite ends of the writer, but this is not observed, in agreement with section 4.3.

Within the confluence region a light strip is observed along the symmetry axis within the perpendicular images for delay times in the range of 0 to 2.92 ns, and 5.44 to 500 ns, confirming the concentration or funneling of flux within this region. In fact the images change very little between 5.44 ns and 500 ns, indicating that the writer relaxes to a state of metastable equilibrium at 5.44 ns, in agreement with the offset of the signal at position A observed in Figure 4.15(b). Assuming that the full thickness of the yoke responds in a similar manner to the surface region sampled by the optical probe, channeling of residual flux to the tip region could lead to problems with EAW.

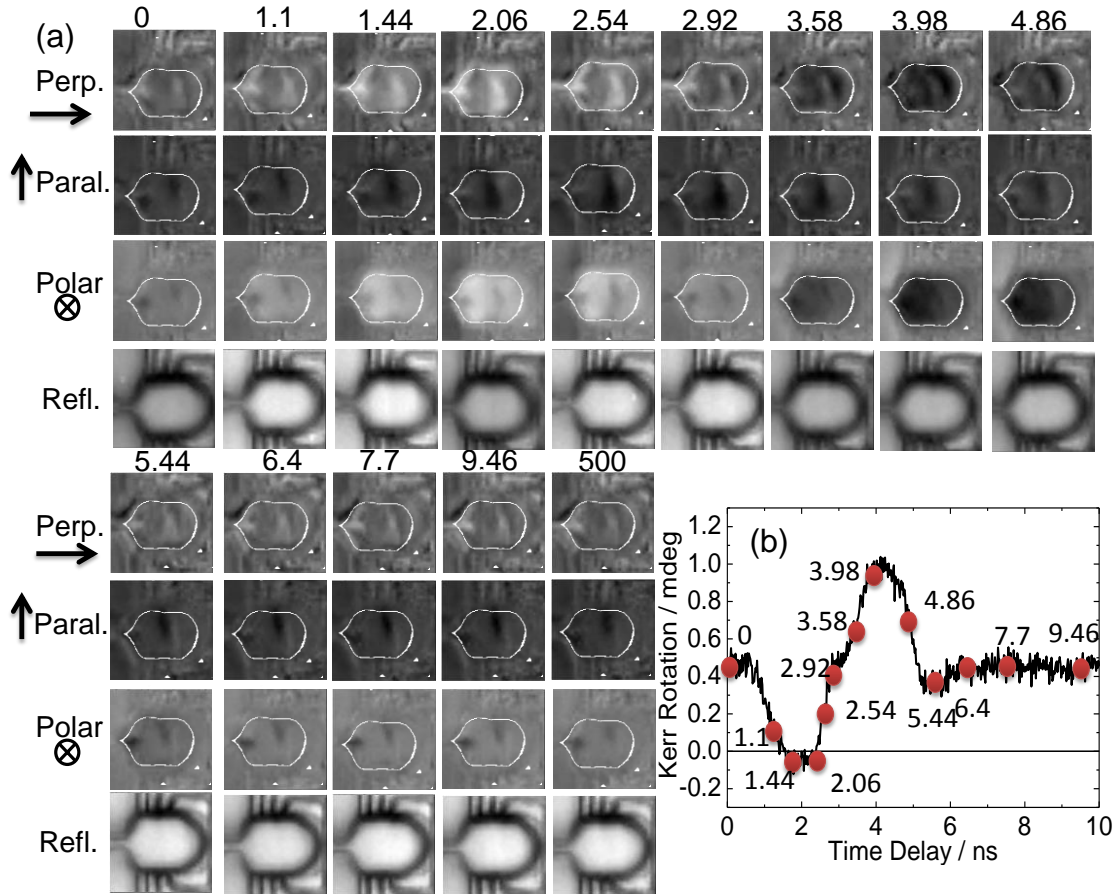


Figure 4.16. (a) Dynamic magnetization and reflectivity images acquired at the delay times indicated in panel (b). For a particular channel the contrast is normalized to the maximum Kerr amplitude observed within that time series. Black/white corresponds to the dynamic magnetization lying in the  $-/+ z$ -direction,  $-/+ x$ -direction, and  $+/- y$ -direction for the polar, perpendicular, and parallel channels respectively. The Cartesian axes are defined within Figure 4.14(a) and shown next to the row names in (a). (b) Time dependence of perpendicular (X) component measured at position C in Figure 4.14(a). 0 ns is the negative delay.

The incomplete relaxation within the confluence region could occur for one of two reasons. Firstly, the effective anisotropy within this area may be different to that within the main part of the yoke, due to the shape or stress or both. The distribution of stress may be modified by lapping of the wafer at the air-bearing surface, so the anisotropy might be different again within an actual write head. If the easy axis is canted from the parallel (Y) direction, then the magnetization may switch between two states that have inequivalent perpendicular

components of magnetization. Secondly, due to the funneling effect, the magnetization in the confluence region is more sensitive to any residual flux present in other regions of the yoke. Compared to section 4.3 and section 4.4, in which contrast in the perpendicular channel was observed in either the upper or lower half of a multilayered yoke but not both, the contrast within the perpendicular (X) channel images at peak values of the driving field (1.44 and 3.98 ns) is more uniform across the width of the yoke. While the excitation conditions are somewhat different in detail to these previous studies, flux beaming is not observed in the region of the coil windings. This may be because the constituent layers of the SAF yoke have thickness greater than the exchange length, leading to a more complicated 3 dimensional ground state that cannot be probed optically.

To summarize the results of this section, time resolved measurements of the perpendicular (X) magnetization component show that the yoke only dominates the dynamics within the confluence region when the pulse is rising. The amplitude of the signal from position A, which is deep within the confluence region, is much larger than that from other positions, indicating funneling of the flux from the yoke to the tip. Dynamic images show an incomplete relaxation behavior within the confluence region after the pulse has gone, which may be due to modified anisotropy within this region and funneling of residual flux from other parts of the yoke. In-plane dynamic images reveal the existence of a non-uniform equilibrium state during pulse cycling and an absence of flux beaming, suggesting that the SAF yoke, which is thick compared to the exchange length, may occupy a more complicated 3 dimensional equilibrium state that cannot be probed optically.

## 4.6 Conclusion and future work

Time resolved scanning microscopy has been performed to study the magnetization dynamics within hard disk writer yokes under different conditions. We have confirmed that the dynamic response of the writer is very sensitive to the driving conditions, when there are three active coil windings, uni-polar driving field in opposite directions result in very different dynamic response within the deep confluence region, suggesting an asymmetric writing field during the actual writing process. While there is only one active coil winding, the relaxation behavior of the yoke is different if the active coil is located at different position. For the same yoke stack structure and same driving frequency, flux beaming seems to occur only when the driving amplitude is not too large, in agreement with the previous study of Kasraj<sup>48</sup> et al. The SAF yoke design did not yield good writing dynamics, perhaps because the inter-layer exchange coupling cannot produce a simple antiferromagnetic alignment of layers within a very thick yoke.

Since the driving conditions is one of the key factors which affects the writer dynamics, a systematic study of the driving condition within a particular writer design is necessary. The amplitude of the driving pulse should be varied while keeping the same repetition rate and pulse width, and the pulse width should be varied while keeping the amplitude and repetition rate constant. All the above haven't yet been addressed symmetrically by experiment. At the same time, higher pulse repetition rates should be considered since the driving frequency within a real hard drive is much higher than 1 MHz.

# **Chapter 5 Observation of vortex dynamics in arrays of nanomagnets**

Results shown in this chapter were obtained through collaboration between three different institutions. The sample was fabricated in the laboratory of Dr. J. R. Childress at Hitachi Global Storage Technology. The TRSKM study was carried out at the University of Exeter by myself and Dr. P. Gangmei. The X-ray photo-emission electron microscopy (XPEEM) was performed at Beamline I06 of Diamond Light Source by Dr. S. A. Cavill, Professor G. van der Laan, Dr. M. K. Marcham and Dr. P. S. Keatley from the University of Exeter. The simulations and analysis were performed by Dr P. S. Keatley and myself. The Scanning electron microscopy (SEM) was carried out at the University of Exeter by Mr. T. Loughran.

## **5.1 Introduction**

Magnetic vortex structure is one of the most fundamental spin structures observed in submicron-sized ferromagnetic elements<sup>64</sup>. Usually Magnetic thin-film square- or disc-shaped nanostructures with adequate dimensions exhibit a magnetic vortex state<sup>65</sup>. The most important feature of magnetic vortex is the out of plane magnetization at the center of the structure due to the competition of the exchange interaction and the magneto-static interaction. The ground state of a vortex structure can be characterized by two degrees of freedom<sup>66</sup>, one is called polarization  $P = \pm 1$  of the vortex core, which is the out of plane spin or magnetization direction in the core or the center of the structure; another is called circulation  $C = \pm 1$ , which is the sense of rotation of magnetization in plane. These binary states can be used for information storage<sup>67</sup> since the polarity and the chirality of the vortex offer two ‘bits’ of data. Therefore,

understanding magnetic dynamics within such devices is the first step for the designing. At the same time, the gyrotropic mode of a magnetic vortex is currently the subject of intense research because microwave emission from a spin torque vortex oscillator (STVO) has a tuneable frequency and narrow linewidth that is attractive for microwave signal processing applications. While the emitted power from a single STVO is too small to be of widespread technological use, it may be enhanced by careful consideration of the device materials<sup>68</sup>, or by phase locking the response of multiple STVOs so that the power level increases as the square of the number of devices<sup>69</sup>. Phase locking has only been demonstrated for a small number of STVOs that share a common magnetic layer or have electrical interconnects between devices<sup>70</sup>. For large numbers of isolated STVOs the dynamic dipolar interaction between the gyrotropic modes of the individual elements has the potential to phase lock and synchronise their dynamic response without the need for common layers or additional interconnects. However to understand the formation of collective gyrotropic modes within large arrays it is first necessary to image the dynamics of individual elements so that the character of the collective modes may be determined.

The excitation and detection of dynamically coupled magnetic vortices has recently been reported in pairs<sup>71~75</sup> and chains<sup>76</sup> of microscale ferromagnetic disks and squares. In arrays of vortices, ferromagnetic resonance (FMR) experiments revealed broadening of the gyrotropic mode as the separation between the elements was decreased<sup>77</sup>, suggesting increased splitting of a large number of unresolved collective modes. The time-resolved magneto-optical Kerr effect (TRMOKE) was used to detect the splitting of collective gyrotropic modes within arrays, which was shown, with the aid of micromagnetic

simulation, to be due to inter-element magnetostatic coupling mediated by uncompensated magnetic charge near to the edges of the elements.<sup>78</sup> While most of these studies investigate microscale magnetic elements, in a STVO, excitation of the vortex gyrotropic mode using spin transfer torque (STT) is achieved by generating a large current density in a nanoscale magnetic element.

In this work we use time-resolved scanning Kerr microscopy (TRSKM) to detect the vortex gyrotropic modes of individual nanomagnets within arrays. By imaging the polar Kerr signal at a fixed point in the microwave cycle, the phase of gyration across the array can be detected. To explore the effect of the dipolar interaction between the elements two arrays of 250 nm square elements with edge-to-edge separation of 500 nm and 50 nm were considered. TR Kerr images reveal that for a small inter-element separation (50 nm) strong magneto-optical contrast can be obtained from small clusters of elements. Micromagnetic simulations show that the observed magneto-optical contrast requires a specific equilibrium magnetic state.

## 5.2 Experiment and sample details

A multilayer stack of composition Ta(5)/Cu(25)/[Ta(3)/Cu(25)]<sub>3</sub>/Ta(10)/Ru(5)/Ni<sub>81</sub>Fe<sub>19</sub>(40)/Al(1.5) (thicknesses are in nm), was sputtered onto an insulating Sapphire wafer of 500 μm thickness, with the Al capping layer being allowed to oxidise naturally. Arrays of Permalloy (Py) squares were formed on the Cu underlayer by a combination of electron beam lithography and ion beam milling. The remaining Cu was patterned by photolithography and ion beam milling to form a coplanar waveguide (CPW) with a width and separation designed to achieve a characteristic impedance of 50 Ω. A schematic of the coplanar waveguide structure is shown in Figure 5.1 (a). The nanomagnet arrays lay on

top of the central conductor in a narrow section of 2.29 mm length in which the signal track was 6  $\mu\text{m}$  wide. Magnetization dynamics were excited using the in-plane magnetic field associated with pulsed or microwave (RF) current waveforms passing through the narrow section of the CPW. A NiCr thin film resistor with dc resistance of  $\sim 50 \Omega$ , was deposited at one end to attenuate the time-varying current and prevent multiple reflections.

Time-resolved scanning Kerr microscopy (TRSKM) was used to study the coupled vortex dynamics of  $250 \times 250 \text{ nm}^2$  square nanomagnets within two arrays with edge-to-edge separations of 500 nm and 50 nm. Landau flux closure domain states were generated by applying an alternating in-plane magnetic field with continuously decreasing amplitude. A Ti:sapphire oscillator was used to generate optical pulses of 100 fs duration, 800 nm wavelength and 80 MHz repetition rate. Second harmonic generation was then used to generate a 400 nm (blue) optical probe that was expanded ( $\times 5$ ) to reduce beam divergence, before being linearly polarized, and then focused to a diffraction limited spot diameter of  $\sim 300 \text{ nm}$  using a high numerical aperture (0.85,  $\times 60$ ) microscope objective lens<sup>79</sup>. TR measurements were made by using a 4 ns optical delay line to change the relative phase of the optical pulses and the pulsed or microwave field excitation generated by the CPW at the sample position. The amplitude of the excitation was modulated at a frequency of  $\sim 3 \text{ kHz}$ . The Kerr rotation was measured using a balanced photodiode polarizing bridge detector, with a lock-in amplifier being used to recover the modulated signal component. TR images were acquired by scanning the sample beneath the focussed spot at a fixed time delay using a piezoelectric scanning stage. The microscope had sufficient spatial resolution and long term

mechanical stability to detect magnetization dynamics within individual nanomagnets within the arrays.

TRSKM is a stroboscopic technique that reveals only changes in the magnetic state. Understanding of the equilibrium magnetic state is required to interpret the TRSKM measurements. Therefore x-ray photo emission electron microscopy (XPEEM) was employed as a complementary technique to understand the typical arrangement of Landau flux closure states that may be expected in the arrays used in the TRSKM measurements. Images of the equilibrium state of nominally identical arrays were acquired by XPEEM at the I06 Nanoscience beamline at the Diamond Light Source, UK. X-rays with energy corresponding to the L<sub>3</sub> absorption edge of Fe (707.12 eV) were used to acquire 10 x-ray absorption images using left- and then right-circular polarization. The images for each polarisation were averaged and normalized to the average of 10 pre-edge (703 eV) images for each polarisation. The difference of these images for the two polarization states was divided by their sum to produce normalized x-ray magnetic circular dichroism (XMCD) images. The spatial resolution of the XPEEM using a potential difference of 15 kV between the sample and the objective was ~50 nm. The resulting high resolution XMCD images show the projection of the in-plane component of the equilibrium state magnetization parallel to the x-ray wavevector.

### **5.3 Results and discussion**

#### **5.3.1 Static and dynamic measurements of single microscale elements**

Since the elements within the arrays have a length that is smaller than the focused spot size in the TRSKM it is necessary to first confirm that the magnetic

field initialization generates a vortex equilibrium state within square elements. In Figure 5.1(b) an XPEEM image of a Landau flux closure state is shown for a 10  $\mu\text{m}$  square confirming that the field initialization is suitable for vortex nucleation. The black and white contrast in the XPEEM image corresponds to the in-plane component of the equilibrium magnetization that lies either parallel or anti-parallel to the x-ray wavevector. In the grey domains to either side of the center, the magnetization is also of opposite sign, so that the magnetization rotates in the plane of the square forming a vortex core at the center. In elements with length greater than the focused spot size in the TRSKM, the Landau state can be detected using the higher frequency magnetic precession within the domains. In Figure 5.1(c) a TR Kerr image of the Landau state in a 1  $\mu\text{m}$  square is shown. The white and black contrast above and below the center of the square, results from the out of plane torque of opposite sign acting on the two domains with magnetization perpendicular to  $\mathbf{h}(t)$  the pulsed magnetic field. In Figure 5.1(d) TR signals acquired from these two domains are almost identical, but for their opposite sign. Therefore, in smaller squares, for which the optical spot size is similar to, or larger than the square, the net polar Kerr signal due to precession within the domains may be negligible. In fact, in an ideal symmetric element the polar Kerr signal due to vortex gyration is also expected to be negligible since there is no net change in the out-of-plane component of the dynamic magnetization as the vortex gyrates within the region of the optical probe. However, detection of the vortex gyration using TR polar Kerr microscopy has previously been reported<sup>80</sup>. In the following we describe how the vortex gyration is observed using this technique.

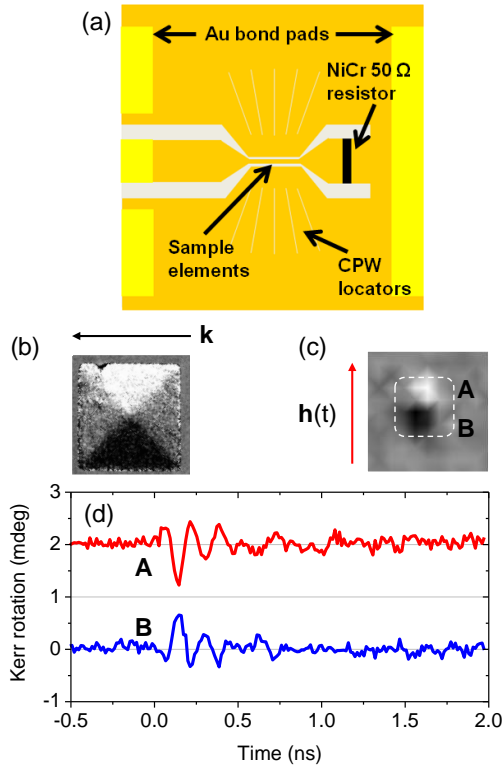


Figure 5.1. (a) Schematic of the coplanar waveguide structure with the location of the sample elements indicated. (b) An XPEEM image of a Landau flux closure state in a 10  $\mu\text{m}$  square is shown. (c) TR Kerr image of a 1  $\mu\text{m}$  square acquired at the first antinode of precession. (d) Time dependent Kerr signals acquired at positions A and B in (c).

In Figure 5.2(a) the measured (black trace) and simulated<sup>81</sup> (blue trace) out-of-plane component of the dynamic magnetization of a 500 nm square is shown in response to an in-plane pulsed field. The experimental TR Kerr signal shows the low frequency vortex gyration superimposed upon the higher frequency precessional modes of the closure domains. The experimental data was acquired with a 300 nm focused spot size that yields the average out-of-plane component of the dynamic magnetization within the probed area. In micromagnetic simulations, when the components of the dynamic magnetization are averaged across the entire area of the square, only higher frequency modes that possess a spatially symmetric component are observed in the out-of-plane magnetization, while the low frequency gyration of the vortex core is only

observed in the in-plane magnetization components. However, if the dynamic magnetization is averaged over a  $250 \times 250 \text{ nm}^2$  region, of roughly similar area to that of the optical probe in the experiment, that is slightly displaced from the center of the square (inset graphic Figure 5.2(a)), the vortex gyration can be observed in the out-of-plane component as in the experiment. This result implies that detection of vortex gyration using the polar Kerr effect in a TRSKM measurement requires a small displacement of the optical probe with respect to the centre of the square. Since the beam intensity has a Gaussian profile, a net polar Kerr signal due to the vortex gyration is observed even when the element is smaller than the spot size, as long as the center of the beam is displaced relative the center of the element.

In Figure 5.2(a) the higher frequency oscillations of the simulated TR trace have smaller amplitude relative to the smoothed trace than observed in the experiment. The relative amplitude is likely to be affected by the position, area, shape, and profile of the region of interest in the simulation, in addition to the pulsed field amplitude. Fast Fourier transform (FFT) spectra shown in Figure 5.2(b) show that the overall dynamic response is well reproduced by the simulation. Spatial maps of the FFT power spectra calculated from the micromagnetic simulation confirm that the lowest frequency mode is the vortex gyrotropic mode, while the higher frequency modes are found to be associated with oscillations of the domain walls separating the Landau closure domains (5 GHz), and higher frequency azimuthal modes with at least one nodal plane in each closure domain (7.6 GHz, 8.9 GHz, and 10.8 GHz).

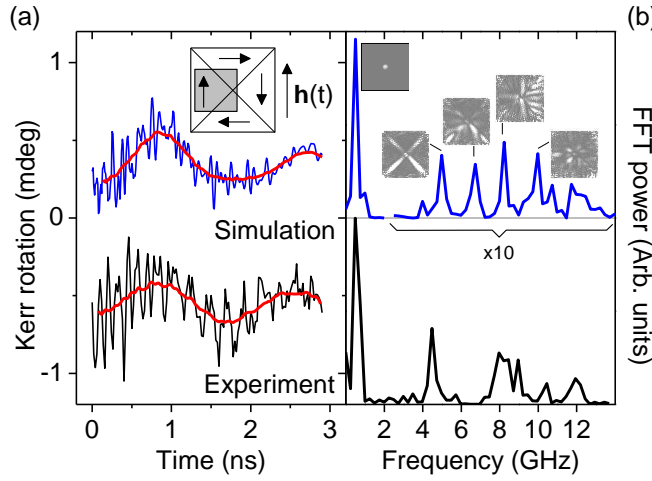


Figure 5.2. (a) Measured and simulated TR traces of the out-of-plane component of the dynamic magnetization acquired from a single 500 nm square in the vortex ground state in response to a pulsed magnetic field. The simulated trace is extracted from the 250 nm square region shown inset. (b) Fast Fourier transform (FFT) power spectra corresponding to the TR traces in (a). The inset images show the spatial distribution of the FFT power spectra calculated from the simulations.

### 5.3.2 Dynamic measurements of arrays

To study the dynamic interaction of vortices within the arrays, TRSKM with RF magnetic field excitation was used. The array with largest edge-to-edge separation (500 nm) was studied first so that the response of individual isolated  $250 \times 250 \text{ nm}^2$  nanomagnets could be detected. The output power of the RF synthesizer was maintained at 25 dBm for all measurements, the driving RF field is estimated to be a few Oe. In Figure 5.3(a) typical TR polar Kerr signals acquired from a single square within the array [highlighted by the blue triangle in the scanning electron microscope image inset in Figure 5.3(b)] are shown for three different values of the RF frequency. The largest amplitude response, corresponding to the resonance frequency of the vortex gyrotropic mode, was found to be at 880 MHz. For the aspect ratio (length to thickness) of the square elements studied in this work, the resonance frequency of the vortex gyrotropic

mode is in good agreement with the empirical formula given in Reference 82. In Figure 5.3(b) the Kerr amplitude for three different elements within the array is shown as a function of the RF frequency. Figure 5.3(b) shows that the frequency dependence of the Kerr amplitude varied from element-to-element.

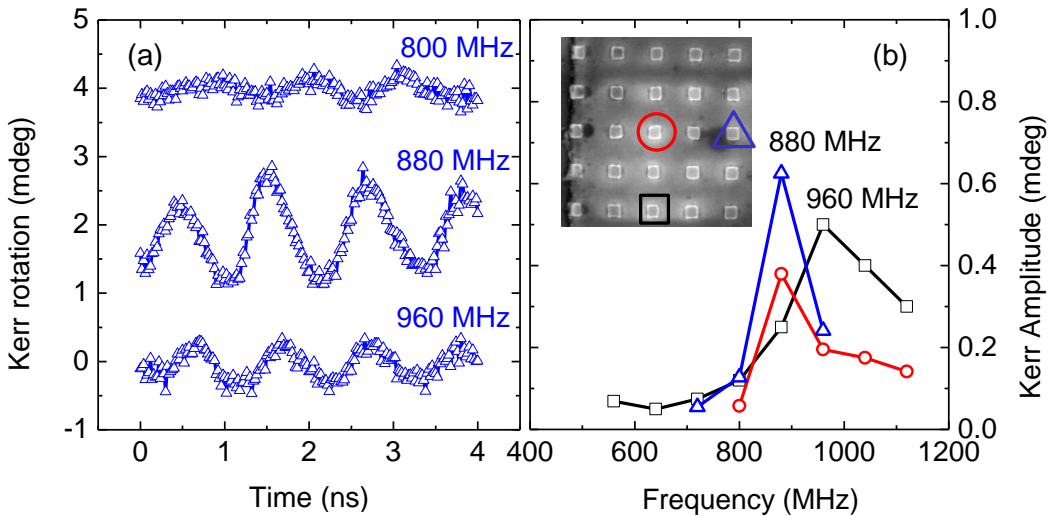


Figure 5.3. (a) Time resolved signal from the element marked by blue triangle in (b). The amplitude of measured TR Kerr signals is shown as a function of RF frequency for the square element indicated by the blue triangle within the scanning electron microscope (SEM) image in panel (b). The data in panel (b) show the frequency dependence of the FMR amplitude for the elements highlighted by the same symbol within the SEM image.

A resonance frequency of  $\sim 880$  MHz was observed in two of the three elements shown, while the linewidth and amplitude were somewhat different in all three elements. While these differences might result from the weak interactions of an element with its nearest neighbours, the gyration frequency depends upon the aspect ratio of the element, and so these differences are more likely due to variations in the size and shape of individual elements resulting from the fabrication process. While the vortex gyrotropic mode is expected to have a narrow linewidth, the frequency resolution of the TRSKM was limited by the laser repetition rate (80 MHz).

In Figure 5.4(a) two TR Kerr images of the array containing 250 nm squares with 500 nm edge-to-edge separation are shown for two points in the microwave cycle separated by  $\pi$  radians (labelled + and -). The frequency of the RF excitation was 960 MHz. It is clear that some elements are missing from the TR images, but where elements are visible, variations in the amplitude and orientation of the black and white contrast of the Kerr signal can be seen. The black and white contrast results from the amplitude modulation of the excitation, as illustrated in Figure 5.4(e). At a particular point in the cycle of the microwave excitation, the vortex core will be at a corresponding point on its trajectory away from the center of the element. The effect of amplitude modulation is then detected in TRSKM measurements as a change of the out-of-plane component of the magnetization ( $\Delta M_z$ ) as the vortex core ‘jumps’ from the center of the element (equilibrium state, RF excitation off) to this particular point on the trajectory (gyrotropic state, RF excitation on). When the core jumps from the center to the edge of the element in this way, a corresponding decrease (increase) of the polar Kerr signal can be observed when the optical probe is near to the center (edge) of the element. As the phase of the excitation changes, the regions of black and white contrast rotate about the centre of the element, as confirmed by TR images acquired at antinodes of opposite polarity. The term ‘phase of gyration’ is hereafter used to refer to the orientation of the regions of black and white contrast.

In the following discussion, different squares within the array will be referred to by their (column, row) coordinates. In Figure 5.4(a) Column 1 lay outside the scanning range. The TR images were acquired at time delays corresponding to antinodes of opposite polarity in the polar Kerr signal acquired from square (5,1). It is clear that the black and white contrast corresponding to vortex gyration is

not observed in all elements within the array. For example squares (2, 5), (3, 5), (4, 3), and (5, 4) appear to be missing. These ‘missing’ squares have a quasi-uniform single domain ground state that supports confined spin wave modes with frequency typically greater than 2 GHz at remanence<sup>83,84</sup> and so no response is observed at 960 MHz. Comparison of Figure 5.4(a) and (b) shows that the formation of the vortex state was not reproducible in all squares. When the ground state of the array was reset, the majority of squares remained in the vortex state, but square (3, 5) adopted the vortex state generating a detectable signal, while squares (4, 2), (4, 4), and (2, 4) adopted the single domain state yielding no signal at 960 MHz.

In the lower panel of Figure 5.4(b) a normalized XMCD image of a nominally identical 5×5 array is shown in the left panel. The dark and light contrast in the XMCD image corresponds to the in-plane equilibrium magnetization that lies parallel and anti-parallel to the x-ray wavevector in the –x direction. To the left of every element is a bright white shadow that is an artefact resulting from the shallow x-ray grazing angle used in XPEEM. In addition the element edges appear as a thick black border. This is a result of imperfect alignment of the 20~25 x-ray absorption images that contribute to each normalized XMCD image. The XMCD image reveals that elements (3, 2) and (4, 5) have a single domain state, which supports the interpretation of the missing elements in Figure 5.4(a). In the remaining elements, approximately one half of each element is dark, while the other half is light. While the detailed structure of the Landau flux closure state observed in the 10 μm square (Figure 5.1(b)) is not readily seen in Figure 5.4(b), opposite contrast above and below the center of each element strongly suggests that the majority of elements have a Landau flux closure domain structure and contain a magnetic vortex.

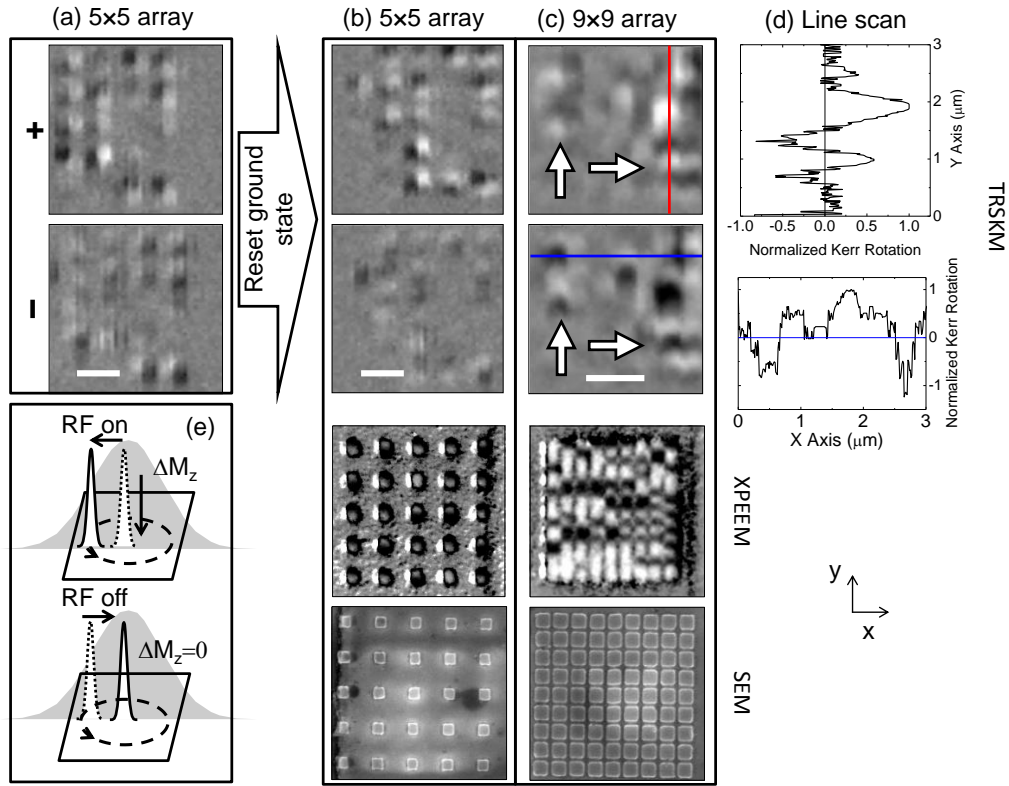


Figure 5.4. TR polar Kerr images, XPEEM images and SEM images of arrays of 250 nm squares with separation of 500 nm in (a) and (b), and 50 nm in (c). After acquisition of the images in (a), the ground state was re-initialized before acquiring the images in (b). In all images the horizontal white bar has 1  $\mu\text{m}$  length. The solid white arrows denote regions of contrast with size comparable to that of a single element. In (a) and (b) the rows and columns of numbers form a coordinate system by which the squares are referred to in the main text. All images are shown at antinodes of opposite polarity (labelled + and -) in the TR signal acquired from the square (5,1) in the top-right corner of the array. (d) Kerr rotation line scans from taken along the red and blue lines shown in (c). (e) Schematic illustration of the how magneto-optical contrast arises. The solid curves represent the polar magnetization component of the vortex core, while the grey shading represents the Gaussian intensity profile of the focused optical probe.

For the two field histories shown in Figure 5.4(a) and 5.4(b) many of the elements in the Landau state appear to have similar contrast and phase of gyration. In Figure 5.4(a) elements (4, 5) and (5, 5) have similar phase of gyration, while element (3, 5) is missing. In Figure 5.4(b) element (3, 5) now occupies a Landau state while the phase of gyration of (4, 5) has changed by  $\pi$  radians. The Landau state has four different configurations corresponding to the

possible permutations of the circulation of the in-plane magnetization and the vortex core polarization. The sense of gyration is determined by the core polarization<sup>85,86</sup>, while the phase of gyration differs by  $\pi$  radians between the two circulation states. Although sweeping an in-plane magnetic field with decreasing amplitude is not expected to select the circulation or core polarization of the Landau state, the  $\pi$  phase shift in (4, 5) suggests that the element has moved between 2 different Landau configurations. On the other hand, the phase difference between the gyration in elements (3, 4) and (4, 5) is different by about  $\frac{\pi}{2}$  radians for both field histories and is instead the result of a difference in size or shape between these two elements. In Figure 5.4(b) the XPEEM image of the 5×5 array reveals that the circulation of the Landau state is not strongly correlated from element-to-element. While it is not possible to extract the core polarization from the XPEEM images, the image clearly shows that nearest neighbours may occupy Landau states with the same or opposite sense of circulation. This again suggests that the phase differences observed from element-to-element in the TR Kerr images of Figure 5.4(a) and 5.4(b) are associated with the presence of vortices of different circulation and polarization.

The configuration of the Landau state within a particular element may depend on factors such as thermal effects, element edge roughness, and inter-element dipolar interactions. In the 5×5 array with large edge-to-edge separation, the dipolar interaction is not expected to have a significant influence on the Landau state configuration. Comparison of Figures 5.4 (a) and (b) shows that several elements (described earlier) changed their equilibrium states when the field protocol used to induce the equilibrium state was repeated. This suggests that thermal effects influence the formation of the equilibrium state in the 5×5 array.

In Figure 5.4(c), similar TR Kerr images were acquired from a 9×9 array of 250 nm squares with 50 nm edge-to-edge separation for which the static and dynamic dipolar interactions between elements are expected to be enhanced. While the spatial resolution of the TRSKM is insufficient to observe the individual elements within the array, remarkably, regions of alternating TR Kerr signal (indicated by the large white arrows) are observed that appear to extend over length scales that are equal to or larger than the individual element size. As shown in the line scan in the upper panel of Figure 5.4(d), the large area of white contrast extends from ~1500-2200 nm, similar to the length of two elements, while in the lower panel, sharp transitions occur at ~400 and ~700 nm, similar to the length of a single element. As observed for the 5×5 array with larger separation, the 9×9 array exhibits regions with no obvious Kerr signal at a microwave frequency of 960 MHz, for example, in the lower-left quadrant of the array. This is consistent with the XPEEM image [Figure 5.4(c), bottom panel] of a nominally identical 9×9 array that shows many of the elements occupy a quasi-uniform single domain state. While 50 nm spacing between individual elements are not fully resolved in the XPEEM image, individual elements are still clearly seen. Elements with uniform contrast over a length scale of the row height (element size) in the *y*-direction occupy single domain states, while elements with contrast variation (dark and light) over the size of the element in the *y*-direction occupy a Landau state. The XPEEM image in Figure 5.4(c) shows a large cluster of Landau states located at the middle of the right-hand edge of the array. While an exact correspondence with the equilibrium states observed by TRSKM is not expected, the appearance of clusters of elements in the Landau state is qualitatively similar.

Micromagnetic simulations using the Object Oriented Micromagnetic Framework (OOMMF)<sup>87</sup> were performed to interpret the TR Kerr images. 2x2 arrays of square elements were simulated using a cell size of 5x5x40 nm<sup>3</sup> and an exchange parameter of 1.3x10<sup>-7</sup> ergs/cm. The nominal dimensions for the film thickness (40 nm), element size (250 nm), and edge-to-edge separation (50 and 500 nm) were used. The saturation magnetization and g-factor were assumed to have values of 800 emu/cm<sup>3</sup> and 2.1 respectively. While a Gilbert damping parameter  $\alpha$  of about 0.01 is typically observed for permalloy, a value of 0.001 was assumed so as to yield smaller linewidths make any mode splitting more obvious. Simulations were performed for five different circulation and polarization configurations. The Landau state of each element was prepared by defining four closure domains with uniform in-plane magnetization and a circular core with uniform out-of-plane magnetization. The five regions were exchange coupled and allowed to relax in zero external magnetic field. Initially the value of  $\alpha$  was set to 0.5 to allow the magnetization to relax more efficiently. Pulsed magnetic field simulations were then performed with a pulse defined as the product of the functions  $f(t) = 1 - \exp(-\frac{t}{\tau_1})$  and  $g(t) = -\exp(-\frac{t-t_0}{\tau_2})$ , where  $t_0 = 70$  ps,  $\tau_1 = 50$  ps, and  $\tau_2 = 40$  ps, so as to yield a full width half maximum (FWHM) pulse width 70 ps and a full (0-100%) rise time of 30 ps.

The pulse shape is shown in the inset of Figure 5.5(b). Vector maps of the magnetization were recorded over a period of 100 ns at 0.05 ns intervals. The out-of-plane component of the magnetization for each element was averaged over its lower half only, so as to yield finite time dependent signal from the gyrotropic mode.

Figure 5.5(a) shows simulated TR signals corresponding to the out-of-plane component of the dynamic magnetization  $M_z$  for each element of a simulated  $2 \times 2$  array. Each column represents a different equilibrium configuration of the Landau states of the elements within the array, as shown in the schematics at the top of each column that are labelled 1 to 5. In each column, four TR signals are shown corresponding to the average response of  $M_z$  in the lower half of the highlighted squares (red) in the schematic of the  $2 \times 2$  array to the right of the TR signals.

The evolution of the TR signals is markedly different for the five equilibrium configurations. TR signals from all four elements in configuration 5 exhibit beating [Figure 5.5(a), column 5] with frequency of  $\sim 70\text{MHz}$ . Since TRSKM with microwave excitation has a frequency resolution of  $80\text{MHz}$ , it is not expected that the modes giving rise to the beating can be resolved experimentally. In configurations 2 and 4, the amplitude of the TR signals from the upper-right and lower-left elements of the arrays decays much faster than those from the upper-left and lower-right elements. In configurations 1 and 3, the TR signals from all elements exhibit a qualitatively similar non-exponential relaxation, but without any clear beating. These features all point to the influence of dipolar interactions between elements. Interestingly, the largest effects, beating in configuration 5 and variations in relaxation in configurations 2 and 4, occur when the array contains elements with different core polarization, suggesting that the polarization drives the inter-element interactions.<sup>88</sup>

In Figure 5.5(b), fast Fourier transform (FFT) spectra are shown for the top-left element in configuration 5 for edge-to-edge separations of  $50\text{ nm}$  and  $500\text{ nm}$ , as used in the experiment. For a separation of  $500\text{ nm}$  the spectrum shows a

single peak with frequency of 0.99 GHz, at which the elements within the two columns gyrate with opposite sense. For a smaller separation of 50 nm, two modes with frequencies of 1.03 GHz and 1.10 GHz are observed, that are different by the 70 MHz beat frequency seen in the time domain. Further simulations of arrays with element separations of 100 nm and 200 nm showed that the splitting of these modes decreased until they could not be resolved for a separation of 500 nm. For the dominant lower frequency mode, elements within the two columns again gyrate with opposite sense. The character of the other possible collective modes will not be considered any further here, since the aim of the present study is only to explain the results of the TRSKM study.

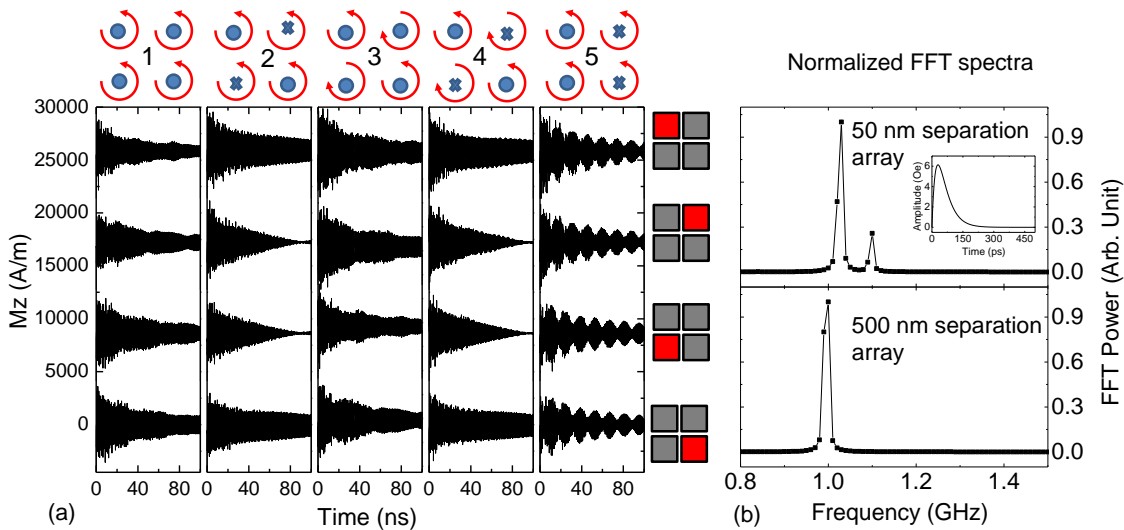


Figure 5.5. (a) out of plane magnetization ( $M_z$ ) sampled from the bottom half of each element. Red squares on the right side of the plot denote the element positions within the array. The red arcs denote the circulation of the Landau state, while the blue dots and crosses denote the vortex polarization. (b) Normalized FFT power spectra for the upper left element in configuration 5. The inset figure in the upper panel denotes the pulse shape used in the simulation.

In the experiments, amplitude modulation was applied to the microwave waveform used to excite the sample. Therefore TRSKM was used to probe the change in the out-of-plane component of the dynamic magnetization with

respect to the equilibrium state, as shown schematically in Figure 5.4(e). To understand how the equilibrium state configuration of the densely packed arrays can lead to the magneto-optical contrast observed experimentally in Figure 5.4(c), images of the difference between the dynamic and equilibrium magnetization maps were calculated.

Figure 5.6(a) shows a magnetization difference image for the vortex gyrotropic mode for an array with 50 nm edge-to-edge separation with equilibrium configuration 4 (Figure 5.5(a)). The in plane RF driving field has frequency of 0.96 GHz and amplitude of 5 Oe, while the value of the Gilbert damping parameter  $\alpha$  was set to 0.01. The pair of elements in the column on the left-hand side of the array shows red contrast towards the center of the pair, while the pair in the right-hand column shows blue contrast towards their center. The red and blue contrast corresponds to a positive and negative change in the out-of-plane component of the dynamic magnetization respectively. To understand the signal obtained by scanning a 300 nm diameter laser spot across the centre of the array, and to afford direct comparison with the experimental results, the calculated  $\Delta M_z$  image was convolved with a 2-D Gaussian function with full width half maximum (FWHM) of 300 nm. In the convolved image of Figure 5.6(b), regions of black and white contrast with similar size to that of an individual element are observed at the centre of the array, providing one possible explanation of why regions of similar period are seen in the TRSKM images of Figure 5.4(c).

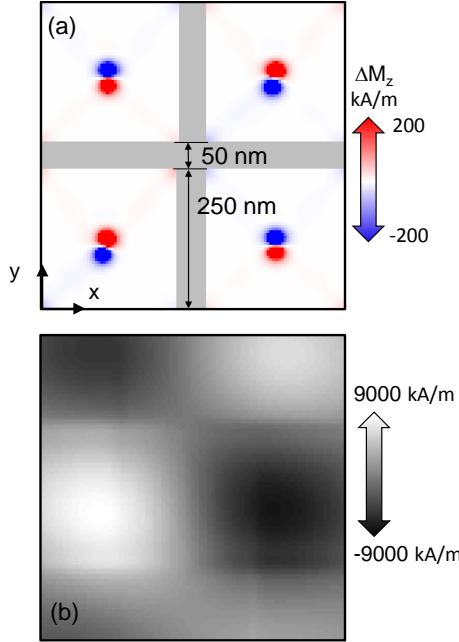


Figure 5.6. (a) Spatial variation of the change of the out of plane magnetization ( $\Delta M_z$ ) induced by the microwave excitation, for an array with 50 nm separation in configuration 4 of Figure 5.5. (b) Convolution of the  $\Delta M_z$  image with a 2 dimensional Gaussian function with FWHM of 300 nm.

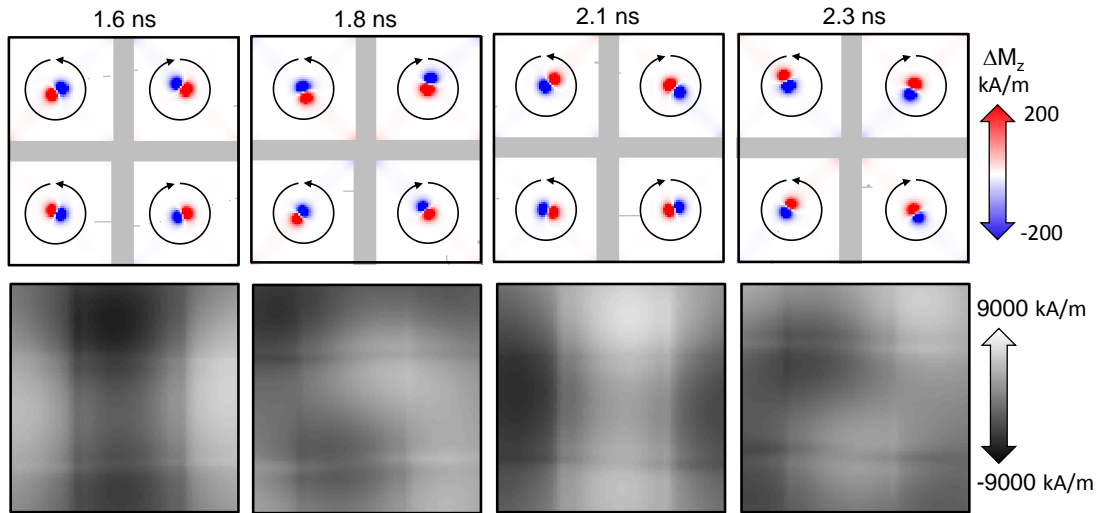


Figure 5.7. Upper panels show the spatial distribution of the change of the out of plane magnetization  $\Delta M_z$  induced by microwave excitation at a frequency of 1.03 GHz. The elements in the 2 x 2 array have 50 nm separation and equilibrium state corresponding to configuration 5 in Figure 5.5. Black arcs denote the sense of gyration of the vortex. The lower panels show the expected form of the magneto-optical signal calculated in a similar manner to that in Figure 5.6 that is described within the main text. The red squares denote the real position of the arrays.

However, the TRSKM images in Figure 5.4(c) reveal that in at least one region, black, or alternatively white, contrast can extend over a length equivalent to two

elements. Figure 5.7 shows difference images for an array with 50 nm element separation, with equilibrium configuration 5 in Figure 5.5(a), excited by an in plane microwave magnetic field with frequency of 1.03 GHz and amplitude of 5 Oe. Images are shown for 4 different points in the microwave cycle, with the sense of gyration in each element being indicated by circular arcs. At a time delay of 1.6 (2.1) ns the blue (red) regions lie closer to the vertical centreline of the array, whereas at 1.8 and 2.3 ns the red regions lie closer to the centreline for 2 elements, while the blue regions lie closer in the other 2 elements. Repeating the convolution procedure used in Figure 5.6, it is seen that black, or alternatively white, contrast now extends across a length of 2 elements in the vertical direction at certain points in the microwave cycle (1.6 and 2.1 ns) while a weaker alternating contrast extends over a length of just one element at other times (1.8 and 2.3 ns). Comparing Figures 5.6 and 5.7, the maximum contrast for regions extending over a length of 1 and 2 elements is seen to be of comparable magnitude. However, in the upper panel of Figure 5.4(d), the region with a length of 2 elements exhibits greater maximum Kerr rotation than those with a length of 1 element. From Figure 5.7 it is obvious that stronger contrast over a square region of 2 element side could be achieved if either all red, or alternatively all blue, regions were to lie along the diagonals close to the centre of the array. While all distinct combinations of circulation and polarization of the 2 x 2 array were simulated, this configuration was not realized. This suggests that dipolar interactions with elements outside the 2 x 2 array, as are present in the 9 x 9 array studied experimentally, are required to achieve this state. Simulations of larger arrays take much longer to compute and lie beyond the scope of the present study.

## 5.4 Summary

In summary, we have demonstrated that TRSKM measurements of the polar Kerr effect can be used to detect vortex gyration, excited by a microwave waveform, in individual square nanomagnets with size smaller than the focused spot diameter. TRSKM images revealed differences in the phase of vortex gyration within individual elements of an array for which inter-element dipolar interactions are expected to be weak. These differences arise both from variations in the gyration frequency of individual elements and also the different possible polarization and circulation of the vortex state. The distribution of equilibrium states within the elements may be influenced by structural imperfections, but thermal effects were also shown to play a role since different equilibria states were obtained when the same field initialization process was repeated. TRSKM images of an array of closely spaced nanomagnets revealed regions of uniform contrast extending over lengths comparable to that of either one or two elements. Simulations showed that the spatial extent of regions of uniform contrast depends strongly on the equilibrium configuration, including the circulation and polarization within individual elements. For certain equilibrium configurations, dynamic simulations revealed splitting of the gyrotropic mode. The present work demonstrates the rich magnetization dynamics that may be achieved by controlling the circulation and polarization of vortices within an array of nanomagnets. More extensive micromagnetic simulations are required to understand the character of the collective gyrotropic modes that may occur.

# **Chapter 6 Time-resolved Kerr microscopy of coupled transverse domain walls in a pair of curved nanowires**

The sample studied in this chapter was fabricated by Dr. L. O'Brien at the University of Cambridge. The TRSKM study was carried out at the University of Exeter by myself and Dr. P. S. Keatley. The results were recently published in the Journal of Applied Physics, in a paper authored by P.S. Keatley, W. Yu, L. O'Brien, D. Read, R.P. Cowburn, and R.J. Hicken.

## **6.1 Introduction**

As has been mentioned in Chapter 1, magnetic domain wall logic has been attracting a lot of attentions recently. Therefore, understanding how to manipulate the magnetic domain walls (DWs) in nano structures has become an interesting research area.<sup>89</sup> Domain wall motion can be driven by either magnetic field<sup>90</sup> or spin polarized current<sup>91</sup>. If the effects of the magneto-crystalline anisotropy are negligible, only the geometry of the nano structure determines the magnetic state of the structure<sup>89</sup>. This is because in such magnetic structures the stray field energy favours the magnetizations to be aligned along the edges of the structure, so the stray field can be minimized. Therefore, the magnetization often points to the long axis of the element. If such a structure is not in a mono-domain state, for instance, two domains with opposite direction exist [as shown in Figure 2.7 (c)-(f)], a 180° head-to-head or tail to tail domain wall (transvers domain wall) has to be present in between the domains<sup>92</sup>.

At the same time, the static and dynamic dipolar interactions are perhaps the most obvious mechanisms by which to couple the magnetic behaviour of two individual nanomagnets when their separation is similar to their size. Therefore, coupled magnetic systems are interesting from both fundamental and technological perspectives<sup>93, 94</sup> since the static magnetic configurations and associated resonances can be continuously tuned using a magnetic field<sup>95</sup>. In the previous chapter we were trying to understand the relationship between the interactions and the gyrotropic mode of the individual elements within a nanomagnets array. In contrast to a nanomagnet, the magnetization of a transverse domain wall (TDW) in a planar nanowire (NW) is only confined across the NW width, but free to move along the NW length. Therefore coupled TDWs are a relatively simple (1D) system in which the static and dynamic dipolar coupling can be studied<sup>96, 97</sup>. As it will be shown soon, after the initiations of the TDW within a coupled NW pair, the TDWs are confined in the center of the NW pairs due to dipolar interactions. In this chapter we use time-resolved scanning Kerr microscopy<sup>79</sup> (TRSKM) to directly observe magnetostatically coupled TDWs and estimate their static de-coupling field. Measurement of the static de-coupling field of coupled TDWs is important for the development of domain wall logic,<sup>98</sup> and race track memory devices.<sup>99</sup>

## 6.2 Sample and experimental set-up

Pairs of curved NWs of different width, separation, and radius of curvature were fabricated along the center of a Ti/Au(200 nm) coplanar stripline (CPS) of length  $L = 16$  mm with 63  $\mu\text{m}$  wide tracks separated by 5  $\mu\text{m}$ . Electron-beam lithography was used to fabricate the NW pairs from a thermally evaporated  $\text{Ni}_{80}\text{Fe}_{20}$  (10 nm) film on a Si substrate. Here we report measurements on a pair

of 300 nm wide NWs with 1.5  $\mu\text{m}$  radius of curvature and inner edge-to-edge separation of 30 nm.

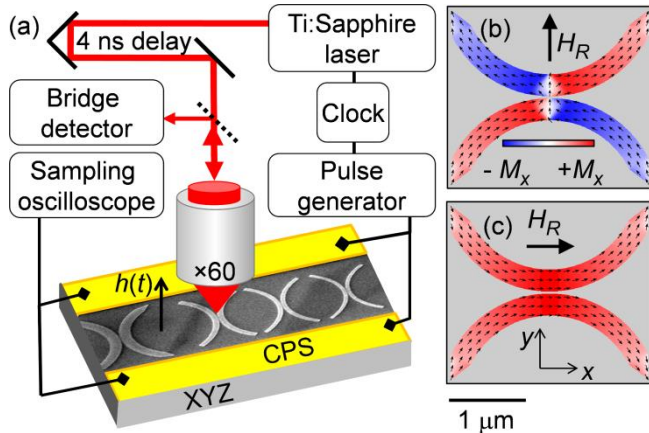


Figure 6.1 (a) A schematic of the experimental geometry with an out-of-plane pulsed magnetic field excitation  $h(t)$ . Part of the NW sample is shown in the SEM image inset between the CPS tracks. The simulated equilibrium states of a NW pair are shown for perpendicular (b) and parallel (c) reset fields  $H_R$ . The red and blue color scale represents  $+M_x$  and  $-M_x$  respectively.

TRSKM was used to study the dynamic response of the NW pair, Figure 6.1(a). A Ti:Sapphire oscillator was used to generate ~100 fs laser pulses with 800 nm wavelength at a repetition rate of 80 MHz. The laser pulses were synchronised with the pulsed output waveform of an impulse generator. The pulsed waveform was amplitude modulated at a frequency of ~3.1 kHz before passing through the CPS. The resulting time-varying (and modulated) magnetic field was used to excite magnetization dynamics within the NWs. The out-of-plane component of the dynamic magnetization was detected at normal incidence using the polar Kerr effect. The laser pulses were expanded ( $\times 5$ ), re-collimated, linearly polarized, and then focused to a diffraction limited spot of ~500 nm diameter using a  $\times 60$  microscope objective. The polar Kerr rotation  $\Phi_K$  was detected using a polarizing balanced photodiode bridge detector. As has been discussed in Chapter 3, since the full beam was sampled on each photodiode there was

no sensitivity to the in-plane component of the dynamic magnetization via the longitudinal Kerr effect. A lock-in amplifier was used to recover the modulated Kerr signal at 3.1 kHz. Time-resolved (TR) traces were acquired by fixing the position of the laser spot on the NW sample and recording the Kerr rotation as a function of time by scanning a 4 ns optical delay. TR images were acquired by fixing the time delay and scanning the sample beneath the laser spot using a piezo-electric stage. A large (~2 kOe) in-plane reset magnetic field  $H_R$  was applied to the NW sample using a quadrupole electromagnet.

### 6.3 Results and discussion

TDWs were formed in the NWs by applying  $H_R$  in the y-direction, Figure 6.1(a).<sup>101</sup> At the same time, micromagnetic simulations using the Object Oriented Micromagnetic Framework (OOMMF)<sup>100</sup> were performed to interpret the experimental time-resolved Kerr images. The NW pair was simulated using a  $2680 \times 2360 \times 10$  nm<sup>3</sup> mesh, a cell size of  $5 \times 5 \times 10$  nm<sup>3</sup>, and exchange parameter of  $1.3 \times 10^{-7}$  erg/cm. The nominal dimensions for the film thickness (10 nm), NW width (300 nm), radius of curvature (1.5 μm), and edge-to-edge separation (30 nm) were used. The saturation magnetization, g-factor, and Gilbert damping parameter α were assumed to have values of 800 emu/cm<sup>3</sup>, 2.1, and 0.01 respectively. Equilibrium state magnetization maps were extracted from hysteresis loop and magnetization curve simulations that assume α = 0.5 to allow the magnetization to relax efficiently. Pulsed magnetic field simulations were performed with a 70 ps pulse with a 30 ps rise time. The pulsed field amplitude was estimated to be ~50 Oe using the Biot-Savart law, and an estimate of the peak current half way along the CPS where the NWs were located. The peak voltage  $V_{\frac{L}{2}}$  is given by  $\sqrt{V_0 V_L}$  assuming an exponential decay

of the amplitude due to losses in the CPS as the pulse propagates along its length  $L$ , where  $V_0$  and  $V_L$  are the incident (5.2 V) and transmitted (1.75 V) peak voltage measured using a 50 GHz sampling oscilloscope.

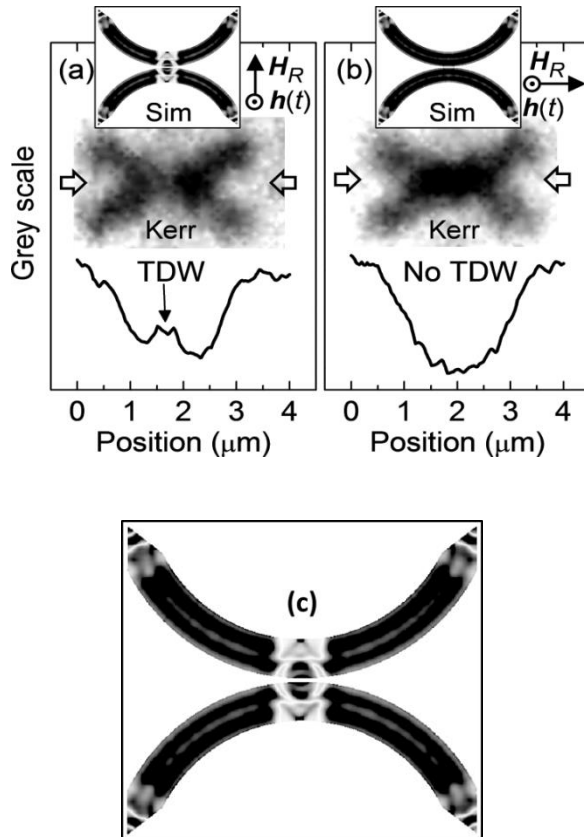


Figure 6.2. TR Kerr images for the NW pair (a) with and (b) without TDWs. Contrast profiles, shown below the Kerr images, are plotted on the same grey scale in (a) and (b). The profiles were extracted from a  $4 \times 0.25 \mu\text{m}^2$  region that was taken horizontally through the center of the interaction region (width and position indicated by block arrows). Corresponding simulated images of the out-of-plane component of the dynamic magnetization are inset in (a) and (b). (c) Zoomed in simulation image in (a), the mixed contrasts in the centre of the pair indicate the reduction of the Kerr signal.

As  $\mathbf{H}_R$  is reduced to remanence, micromagnetic simulations show that the magnetization in each NW relaxes towards opposite x-directions to form two domains with a TDW at the center of each NW. In Figure 6.1(a) the magnetizations in the domains of the upper NW are tail-to-tail (TT), while those of the lower NW are head-to-head (HH).<sup>96</sup> Since the TDWs form at the closest

point of separation, this will now be referred to as the TDW interaction region. The TDWs can be ejected from the NW pair by applying  $H_R$  in the x-direction, Figure 6.1(b).<sup>101</sup> When the field is reduced to remanence the magnetization relaxes to form a single domain, where the magnetization follows the curvature of the NWs.

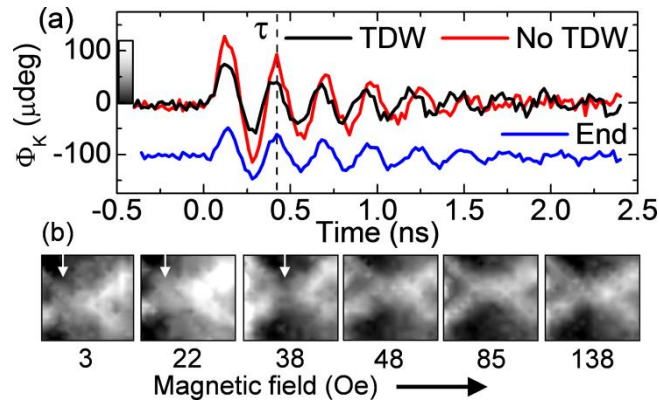


Figure 6.3. (a) TR Kerr signals acquired at remanence from the interaction region with (black curve) and without (red curve) TDWs, and from the end of a NW (blue curve, offset for clarity). (b) A sequence of TR Kerr images acquired at remanence and at delay  $\tau$  after a magnetic field of increasing amplitude has been applied in the x-direction.

TR images acquired at a maximum of the polar Kerr precession signal are shown for the NW pair with and without TDWs in Figure 6.2(a) and (b) respectively. It was not possible to couple to the TDW resonance<sup>102</sup> using an out-of-plane pulsed magnetic field. However, by imaging the precessional response within the domains the TDWs can be detected. The Kerr image in Figure 6.2(a) reveals a small reduction of the Kerr signal in the interaction region, while in Figure 6.2(b) the Kerr signal appears to be more uniform, and perhaps slightly enhanced in the interaction region. The enhanced signal is due to the magneto-optical contribution from both NWs in the interaction region.<sup>102</sup> This effect also occurs when the TDWs are present in the NWs, and leads to a smaller reduction in the Kerr signal than might be expected from micromagnetic simulations (inset). The difference in Kerr signal is clearly seen in horizontal

contrast profiles extracted from a 250 nm wide section taken through the center of the interaction region.

In Figure 6.2(a) the contrast profile shows a clear reduction in the black contrast at the expected location of the TDWs (indicated by arrow), while no such reduction is observed in Figure 6.2(b) indicating the absence of the TDWs. The inset simulated images of the out-of-plane component of the dynamic magnetization show that the TDWs lead to a complicated response that cannot be spatially resolved experimentally. In the interaction region the precession frequency will vary due to the continuously changing magnetization and internal field resulting in a net reduction in the out-of-plane component of the dynamic magnetization, as observed experimentally in the Kerr images.

When TDWs are present in the interaction region a stray magnetic field is generated by uncompensated magnetic dipoles at the inner edges of the NWs. Since the HH and TT TDWs have opposite net magnetostatic charge, the magnetic potential is attractive and the TDWs are magnetostatically coupled.<sup>96</sup> Here we estimate the static de-coupling field of the TDWs using TRSKM. Figure 6.3(a) shows TR signals acquired from the interaction region of the NW pair shown in Figure 6.2(a) and (b). A TR signal acquired from the left-most end of the upper NW in Figure 6.2(a) shows that the precession has similar phase near to the ends of the NW, while the amplitude is slightly reduced since only a single NW is probed. When TDWs are present (absent) in the interaction region the precession frequency was 3.8 GHz (3.56 GHz). The higher frequency when TDWs are present is consistent with an increase in the demagnetizing field since the magnetization is confined across the width of the NW. In addition, the static dipolar field of one TDW may contribute to the total internal field within the

other TDW. When the TDWs are ejected the magnetization is parallel to the length of the NW so the demagnetizing and stray field contributions to the internal field are reduced.

In Figure 6.3(b) a sequence of TR Kerr images are shown. The images were acquired at time delay  $\tau$  in Figure 6.3(a) for which the precession signals with and without TDWs show temporal overlap so that it is possible to observe the transition between NWs with and without TDWs. First TDWs were generated in the interaction region (with pulse generator switched off).  $H_R$  was reduced to remanence and the field orientation rotated through 90°. The first image in Figure 6.3(b) shows the dynamic response at remanence (~3 Oe). A reduction in Kerr signal observed slightly to the left of the interaction region (indicated by arrow) indicates the presence of the TDWs. The shift of this region may be due to pinning of the TDWs at edge defects to the left of the interaction region.

Before each image was acquired, a magnetic field was applied while the impulse generator was switched off to avoid resonance assisted de-coupling of the TDWs. The field strength was increased between subsequent images, but then reduced to remanence for the acquisition of each image. Images acquired after applying a field of 22 Oe and 38 Oe, still show the reduced region of Kerr intensity to the left of the interaction region. Differences in the first three images may be attributed to the influence of different pinning sites for the TDWs after larger magnetic fields have been applied.

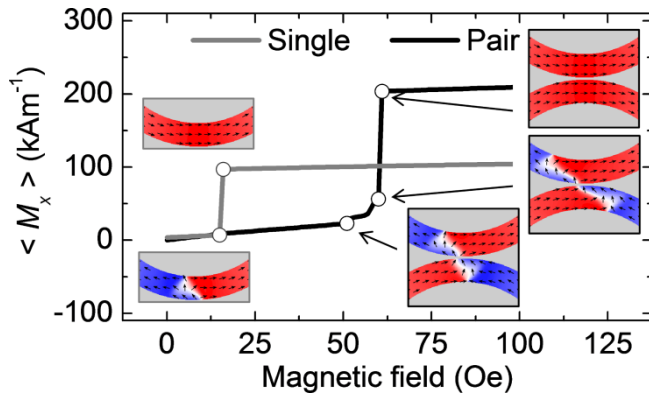


Figure 6.4. Simulated magnetization curves for single and pair NW configurations. Inset maps of the static magnetization are shown where red and blue indicate  $+M_x$  and  $-M_x$  respectively. The height of the curve for the NW pair is twice that of the single NW since only one NW is present in the simulated mesh in the latter case.

Images acquired after a field of 48 Oe was applied, show the TR Kerr signal to be more uniform throughout the NW pair, with little difference observed after 85 Oe, 138 Oe, and  $H_R \sim 2$  kOe (not shown) was applied, indicating that after 48 Oe the TDWs were ejected. Therefore, the static TDW de-coupling field is estimated to be between 38 Oe and 48 Oe.

To understand if the experimental TDW de-coupling field was reasonable, magnetization curves (starting from zero field) were simulated for single and pair NW configurations that assume no edge roughness or thermal effects. Figure 6.4 shows the averaged  $M_x$  component of the static magnetization averaged over the simulated mesh. For the single NW the TDW was ejected at 15 Oe. In contrast the TDWs of the NW pair were ejected via a series of metastable states. Initially the TDWs are displaced as the domains with magnetization parallel to the applied field grow at the expense of the antiparallel domains. The TDWs are displaced in opposite directions owing to the TT and HH domain structure. Up to 51 Oe, the TDWs retain their remanent state structure. However, as the field is increased to 60 Oe, the TDWs are stretched,

but remain coupled at the point of closest separation. Above 60 Oe the TDWs are de-coupled, ejected and the magnetization in each NW forms a single domain. Experimentally it is unlikely that the meta-stable states at larger values of the applied field will be realized due to thermal activation of the switching process. The experimental estimate of the TDW de-coupling field was found to be between ~60% to 80% of the zero temperature simulated values, in agreement with previous reports.<sup>103</sup>

#### **6.4 Conclusion**

In summary we have used TRSKM to directly observe the presence of TDWs in a pair of curved NWs with HH and TT domain structure. From TR Kerr images the value of the static de-coupling field was estimated to be between 38 and 48 Oe in good agreement with a simple micromagnetic model and previous reports<sup>103</sup>. While TRSKM was used to characterise the static de-coupling field in this work, dynamic coupling and microwave assisted de-coupling may be explored by using an in-plane RF magnetic field to couple to the NW resonances<sup>102</sup>. This experimental approach may prove to be a powerful tool for the characterisation of interacting TDWs.

# **Chapter 7 Low temperature time resolved magneto optical Kerr effect study of a wedged CoO/Py bilayer**

The sample studied in this chapter was fabricated in the laboratory of Professor Qiu at the University of California at Berkley. The low temperature MOKE study was carried out by myself at the University of Exeter. XFMR measurements were made by Dr. S. Cavill, Dr. M. K. Marcham, Dr. L. Shelford, and myself at Beamline I06, of the Diamond Light Source.

## **7.1 Introduction**

Chapter 4 is devoted to study the dynamics within a hard disk drive (HDD) writer yoke, which is basically a small electric-magnet. The data stored within a HDD are read back by detecting the media stray field via a magnetic tunnel junction<sup>104</sup> which contains a fixed ferromagnetic layer and a free magnetic layer separated by a non-magnetic insulator. Usually, the fixed layer is fixed by a mechanism called ‘antiferromagnetic/ferromagnetic’ (AFM/FM) exchange bias<sup>26</sup> as has been introduced in Chapter 2. At the same time in the data storage industry, FM/AFM bilayers are also widely used in devices such as magnetic random access memory (MRAM)<sup>105</sup>, which attracts even more attention from the data storage industry, since it doesn’t need power to hold the memory. The exchange bias occurs at the AFM/FM interface, where the hard magnetization of the AFM biases the magnetization of the softer FM<sup>26,106,107</sup>. However, the mechanism of the exchange bias is still not very well understood. Ohldag<sup>108</sup> et al. have confirmed that it is the small percentage of uncompensated spins near the interface that contribute to the exchange bias, while Wu<sup>109</sup> et al. showed that within the CoO/Fe system, only a small number of frozen spins are enough

to generate exchange bias during field cooling, with the frozen and unfrozen spins being distributed uniformly within the CoO layer.

However, since most of the current and emerging devices must operate in the high frequency regime, improved understanding of the magnetization dynamics within the FM/AFM system is needed to optimize device design. Nurmikko<sup>110</sup> et al. have studied magnetizaion dynamics within the NiFe/NiO system by an ultrafast optical pump-probe method and observed a coherent magnetization rotation induced by an ultrafast ‘unpinning’. Kuanr<sup>111</sup> et al. have studied the NiO/NiFe system by VNA-FMR (vector network analyser-FMR) and BLS (Brillouin light scattering). By comparing the results obtained from these two methods they confirmed that the relaxation rate measured by FMR and BLS techniques is different. McCord<sup>112</sup> et al. have studied the dynamics of the NiFe/IrMn system by pulsed inductive microwave magnetometry (PIMM) and observed a transition from superparamagnetic to antiferromagnetic behavior with increasing IrMn thickness. McMichael<sup>113</sup> et al. have studied the NiO/Py system by both hysteresis loop and FMR measurements and found that the exchange bias measured within a hysteresis loop is always larger than that measured by FMR. In addition, they also showed that in this system the FMR resonance field decreases and the linewidth increases as the temperature decreases. However, a systematic study of how the AFM layer thickness and the temperature affect the exchange biased system has not been reported yet. In this chapter, the magnetization dynamics within the FM/AFM system are studied by field cooling a CoO(wedge)/Py film so that the effect of both thickness and temperature can be determined.

The sample stack structure is shown in figure 7.1(a). A mask was made to define the tracks of a CPW shown in figure 7.1(b). This was placed over the top of a 10 mm × 10 mm × 1 mm single crystal MgO(001) substrate. A Ag (50 nm)/CoO (0 – 5 nm)/ Ni<sub>80</sub>Fe<sub>20</sub> (5nm) stack was then deposited onto the the MgO substrate by means of Molecular Beam Epitaxy (MBE). The CoO was wedged and was formed by growing Co in an oxygen atmosphere ( $10^{-6}$  torr). The mask was then removed leaving the sample stack patterned in the form of a CPW structure.

## 7.2 Experimental set up

This study involves two different measurement techniques, namely TRMOKE and XFMR (X-Ray ferromagnetic resonance). The TRMOKE set up has already been introduced in Chapter 3, section 3.2.6.

Phase-resolved XFMR<sup>50</sup> based on detection of XMCD<sup>114</sup> was performed at the Diamond Light Source. As shown in figure 7.1(c), a phase modulated RF excitation of 4 or 6 GHz was supplied to the CPW and used to generate an in-plane microwave magnetic field within the sample. The X-ray pulses from the synchrotron were phase locked with the RF and directed onto the sample at grazing incidence. The incident X-ray energy was tuned to either the Ni or Fe L<sub>3</sub> edge in order to resolve the magnetization dynamics within the Py layer. Measurements were made in fluorescence yield by collecting photons emitted from the decay of excited core electrons by a large area photodiode placed immediately in front of the sample. A static magnetic field of variable strength was applied along the CPW in the plane of the sample.

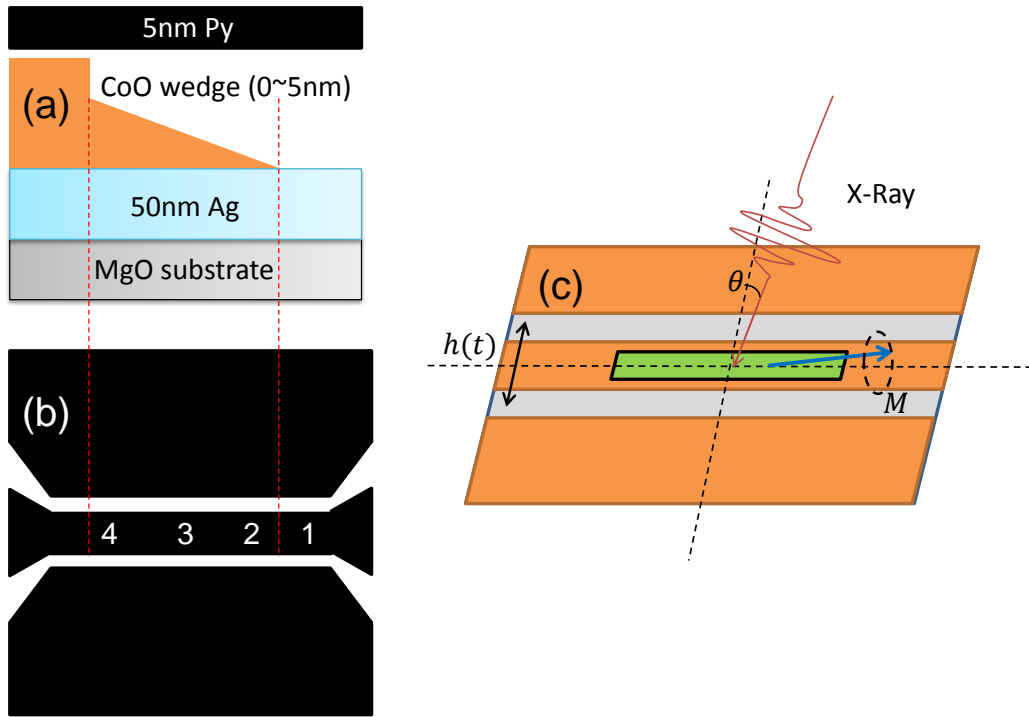


Figure 7.1. (a) The sample stack structure. (b) Positions studied by MOKE. There is no CoO at position 1, 1nm of CoO at position 2, ~3-4nm of CoO at position 3 and ~4-5nm of CoO at position 4. (c) Schematic of the detection scheme.

### 7.3 Results and discussion

Kerr hysteresis loops were acquired first in order to quantify the exchange bias and coercivity occurring at different temperatures and for different thickness of CoO. Figure 7.2 shows the hysteresis loops obtained from different positions on the wedge at different temperatures.

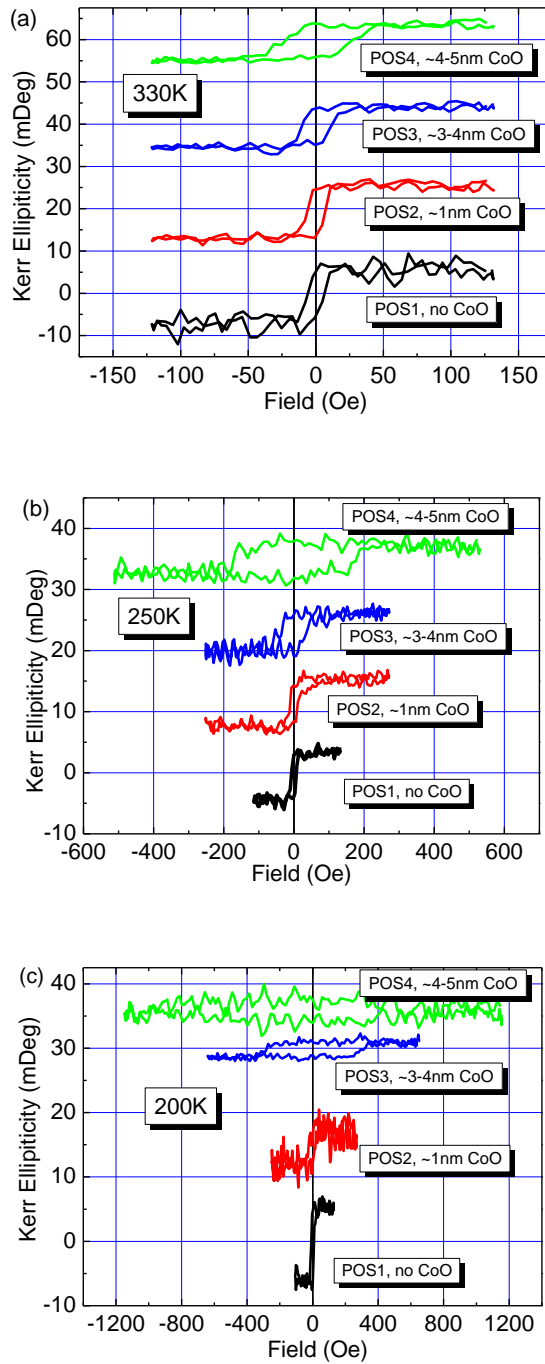


Figure 7.2. Kerr hysteresis loops from different positions on the wedge measured at different temperatures. Loops have been offset vertically for the sake of clarity. POS denotes positions marked in Figure 7.1 (b). There is no CoO at position 1, 1nm of CoO at position 2, ~3-4nm of CoO at position 3 and ~4-5nm of CoO at position 4.

Figure 7.2(a) shows that at 330 K, which is well above the Néel temperature of CoO (291K), the coercivity of the system does not have any obvious dependence on CoO thickness increases until the thick end of the wedge is

reached. Unsurprisingly, no exchange bias was observed, since the CoO layer is expected to have paramagnetic order. Hysteresis loops in figure 7.2(b) and (c) were acquired at 250 K and 200 K. The sample was field cooled from 330 K to 90 K in a bias field of 800 Oe applied along the length of wedge before being warmed to the measurement temperature. The coercivity is seen to increase dramatically as the CoO thickness increases, especially at positions 3 and 4, at both temperatures. Increased coercivity may be expected as AFM order is established within the CoO layer since more energy is needed to reverse the FM layer magnetization due to the exchange interaction with spins at the CoO interface<sup>115</sup>. However, no exchange bias was observed. This suggests that the AFM state is disordered, possibly because the lack of epitaxy between the CoO and Py prevents the field cooling from inducing a net spin polarization at the CoO interface.

Figure 7.3 and 7.4 shows the dynamic response for excitation at 2 and 4 GHz. Field sweeps were made with a fixed phase difference between the probe laser pulse and the RF waveform. Two values of the phase were used that were different by  $\frac{\pi}{2}$  radians. Since the absolute phase of the RF waveform was unknown, the complex signal was plotted in the Argand plane and rotated, using the matrix (7-1), so that the rotated components had dispersive and absorptive character respectively.

$$\Omega = \begin{pmatrix} \cos\theta & -\sin\theta \\ \sin\theta & \cos\theta \end{pmatrix}. \quad (7-1)$$

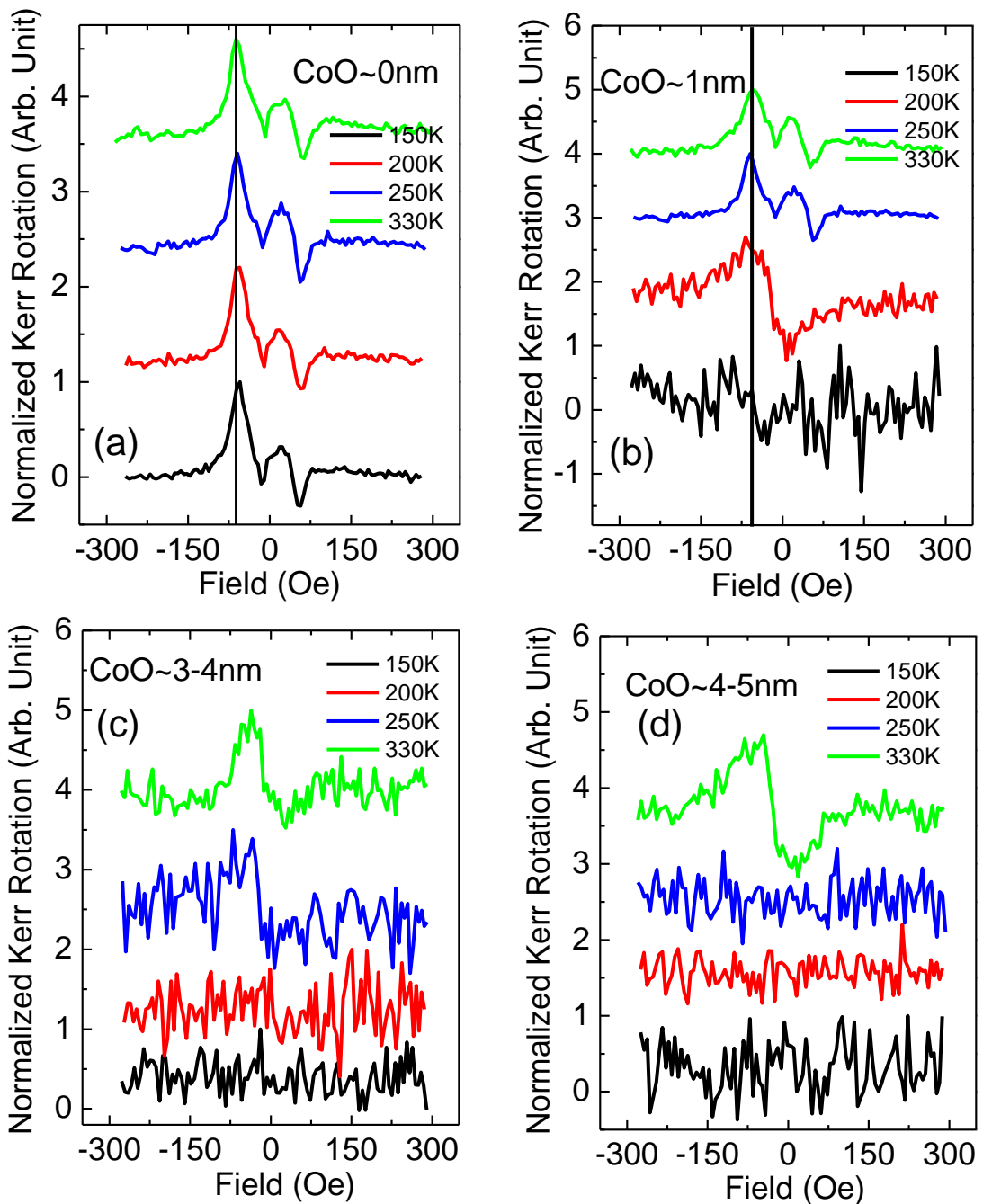


Figure 7.3. Kerr signals proportional to the imaginary part of the magnetic susceptibility for 2 GHz RF excitation. A vertical offset has been introduced for the sake of clarity.

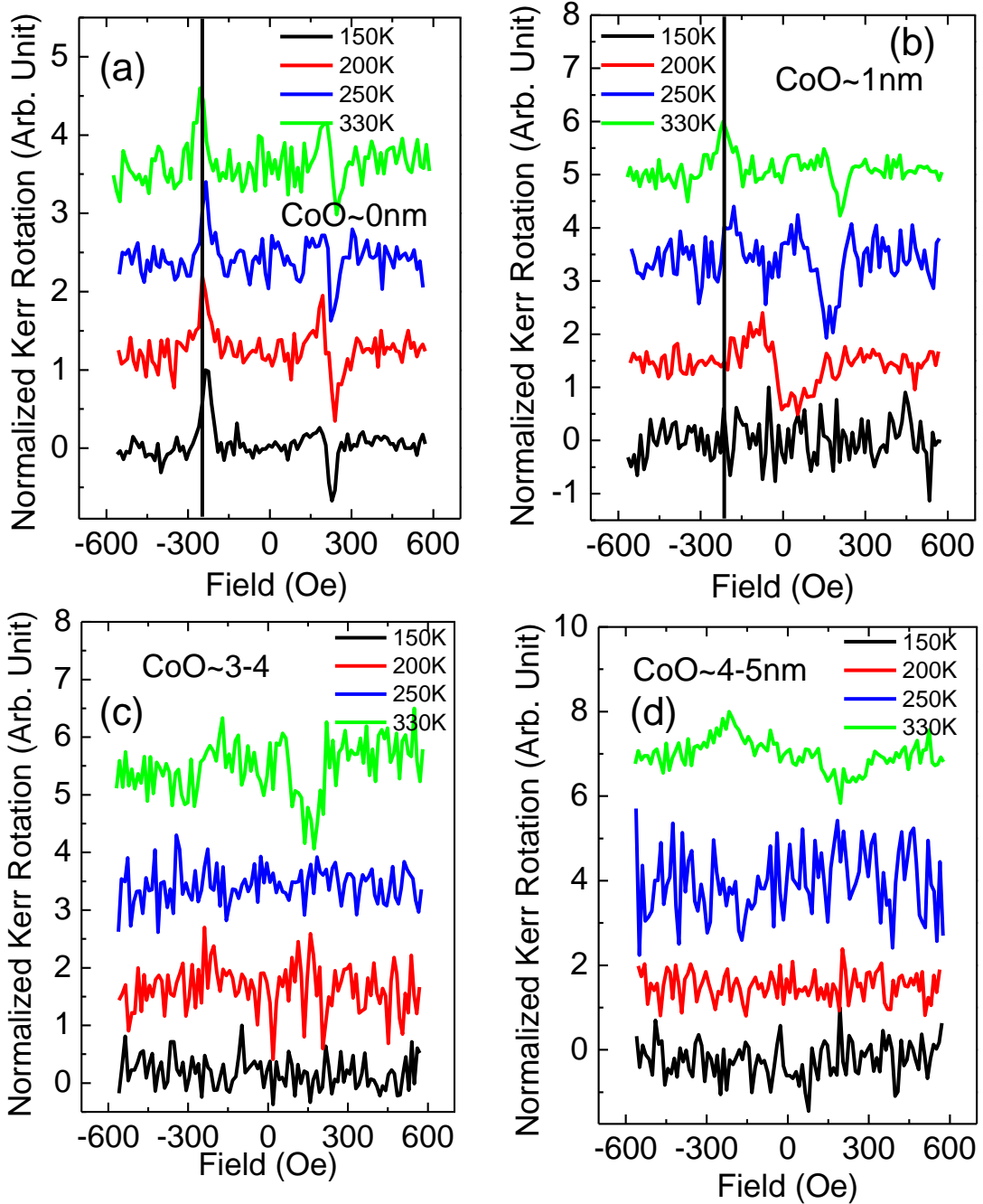


Figure 7.4. Kerr signals proportional to the imaginary part of the magnetic susceptibility for 4 GHz RF excitation. A vertical offset has been introduced for the sake of clarity.

The resonance fields and linewidths were extracted from the absorptive part of the susceptibility by fitting the data acquired with negative bias field to a Lorentz function are shown in Figure 7.5. Position 1 has no CoO under the Py layer. Since the Py has a relatively high Curie temperature (723 K) its magnetization is

effectively constant for the range of temperatures studied here. Therefore no significant change of the resonance field and linewidth is observed with decreasing temperature.

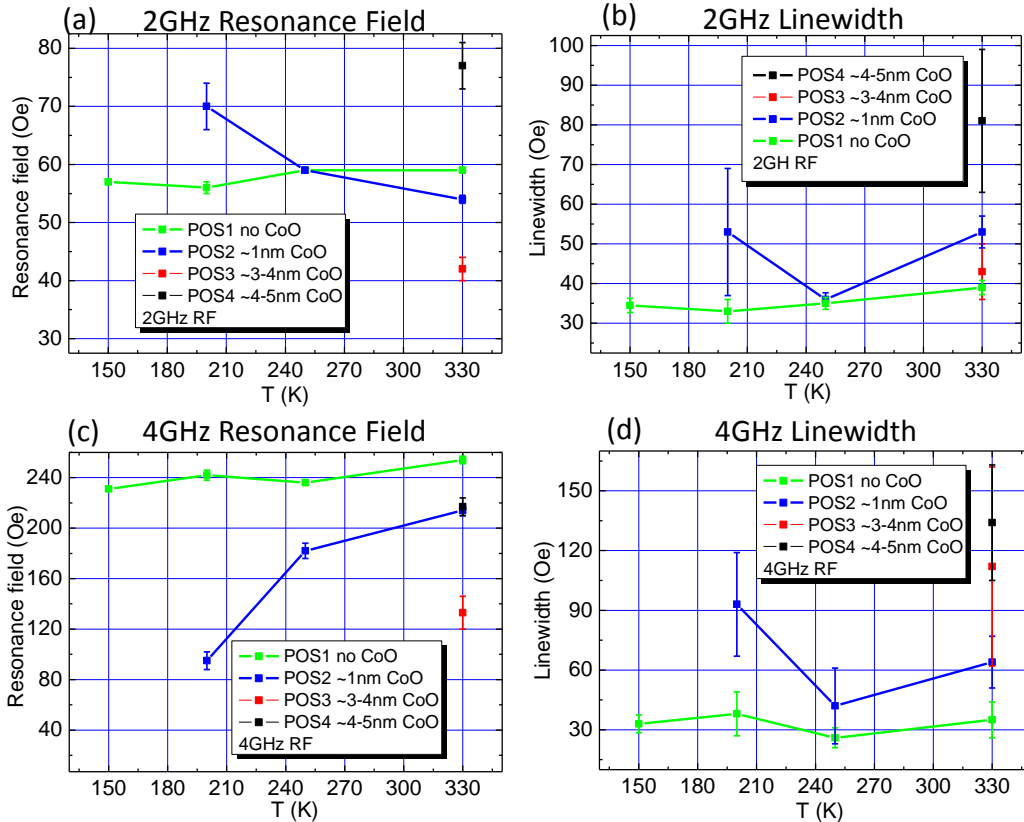


Figure 7.5. (a), (b) temperature dependence of resonance field and linewidth respectively at a frequency of 2 GHz. (c), (d) temperature dependence of resonance field and linewidth respectively at a frequency of 4 GHz.

Interestingly, the resonance field at position 2 (1nm CoO) with 2 GHz RF field seemed to increase slightly as the temperature was decreased to 250 K, but at 4 GHz the resonance field clearly decreases monotonically with temperature. However the linewidth at this position has similar temperature dependence at both 2 and 4 GHz. At positions 3 and 4, the signals are significantly broader at room temperature and disappear once the temperature is reduced below the Néel temperature. The difference between the dynamic behaviour at positions 1

and 2 demonstrates the strong sensitivity to the CoO underlayer. It also appears that most of the traces have no clear symmetry with respect to the sign of the applied bias field. For example, in figure 7.3(a), at negative field the trace has somewhat large amplitude and has shape consistent with the absorptive part of the susceptibility, while at positive field the signal appears to be an admixture of the dispersive and absorptive components. This may occur if the phase difference between the RF field and the laser probe varies during the field scan. Since the sample chip and printed circuit board (PCB) were connected by silver paint, it is possible that the changing magnetic field leads to some mechanical displacement of the sample chip and its connection to the PCB causing a change in impedance and hence a change in the phase of the microwave current.

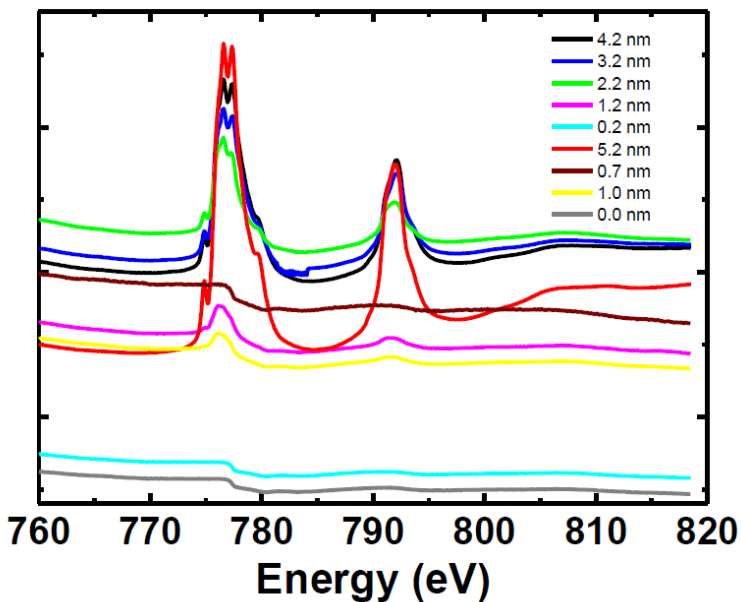


Figure 7.6. XAS scans through the Co  $L_3$  and  $L_2$  edges. The thickness values of the CoO at different positions on the wedge are shown within the legend.

In order to obtain a deeper understanding of the dynamic behaviour of the CoO/Py system, phase resolved X-ray magnetic ferromagnetic resonance was

performed on this sample at the Diamond Light Source. As shown in Figure 7.6, X-Ray absorption spectra (XAS) acquired near the CoO edge at room temperature show a monotonic increase of the CoO signal as the X-ray spot is scanned towards the thick end of the wedge. The thickness values shown in the figure were calculated from the position along the wedge.

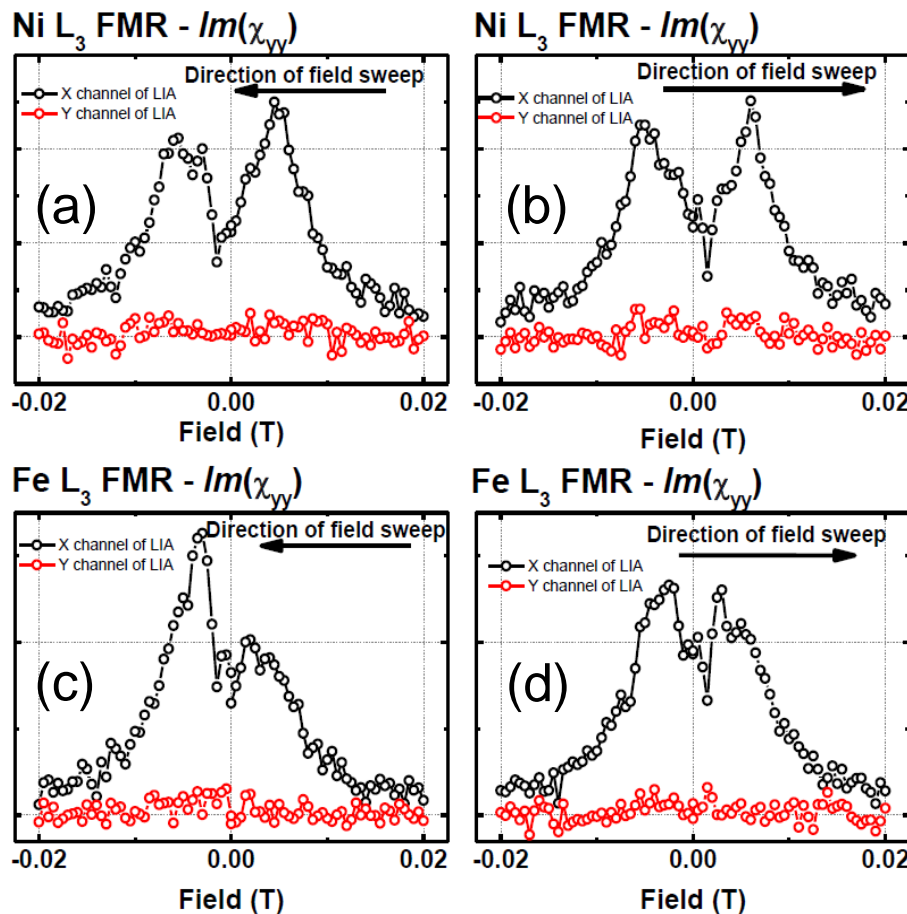


Figure 7.7. XFMR field sweeps at the Ni and Fe  $L_3$  edges at 2 GHz for  $\sim 1\text{nm}$  CoO at room temperature. The output of the X and Y output channels of the lock-in amplifier (LIA) are shown.

Figure 7.7 shows XFMR field sweeps at the Ni and Fe  $L_3$  edges at 2 GHz and room temperature for  $\sim 1\text{nm}$  CoO. The lack of symmetry of the FMR curves seen in Figures 7.3 and 7.4 is also present in figures 7.7(a) and (c). It should be noted that the XFMR field sweeps show absorptive components of the

susceptibility that have the same polarity at both positive and negative fields, while the Kerr field sweeps show the polarity changing as the field direction is reversed. This is because the two techniques sense different components of the magnetization. The magnetization is excited by a torque  $\sim \mathbf{M} \times \mathbf{h}(t)$  within the small amplitude regime. Here  $\mathbf{M}$  is the magnetization of the sample, and  $\mathbf{h}(t)$  is the dynamic field perpendicular to the bias field, which is dominated by the in-plane RF magnetic field. The Kerr signal is dominated by the out-of-plane component of  $\mathbf{M}$ , which oscillates with opposite phase when the polarity of the field and hence the equilibrium direction of  $\mathbf{M}$  is reversed. However, in XFMR, the grazing incidence X-ray, shown in Figure 7.1(c), mainly senses the oscillating in-plane magnetization component perpendicular to the waveguide. The phase of this component remains unchanged when the direction of the static magnetization is reversed.

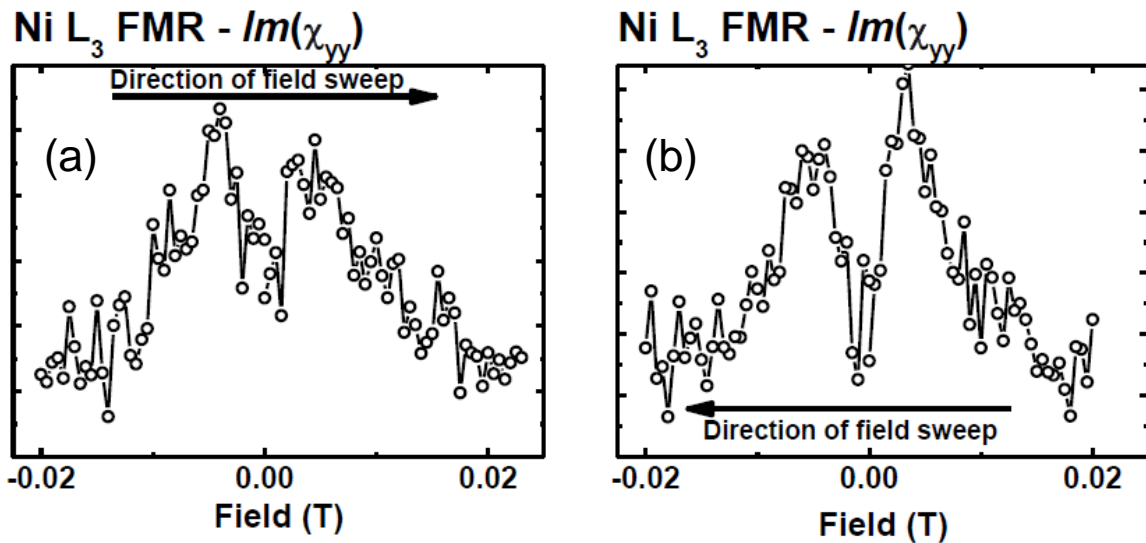


Figure 7.8. XFMR field sweep at the Ni  $L_3$  edges at 2 GHz and 330K for ~1nm CoO thickness.

Figure 7.8 shows XFMR field sweeps at the Ni  $L_3$  edge at 330 K and 2 GHz for 1 nm CoO. The signal is noisier but the lack of symmetry with respect to field

polarity is still observed. No exchange bias was expected since the measurement temperature exceeded the Néel temperature. Both XFMR and MOKE field sweeps show that at 330 K, for 1 nm CoO, the resonance field is ~40-60 Oe.

In order to study the coupling between the AFM and the FM layer, and the dynamics of the AFM/FM interface, dynamic XMLD measurements were performed to study the dynamics of the Co moments. Figure 7.9 shows the Co moments that align perpendicular to the permalloy moments. The electric field of the x-rays is applied along the direction of the permalloy moments. Figure 7.9 (b) shows how during FMR the permalloy magnetization precesses and as a result the interfacial Co moments try to reorient so as to remain at 90° to the magnetization of the permalloy. No XMCD should be observed but a dynamic XMLD signal can in principle be detected.

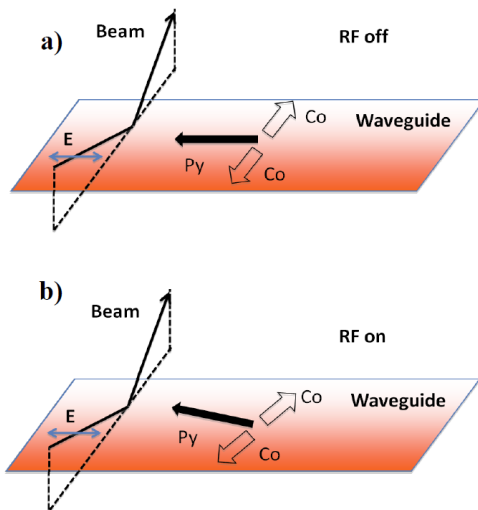


Figure 7.9. Schematic diagrams of the geometry used for the XMLD measurement. (a) The equilibrium configuration (RF off). The cooling field was applied along the waveguide to align the magnetization of the permalloy. The Co moments then align perpendicular to the permalloy moments. The electric field of the x-rays is applied along the direction of the permalloy moments. (b) During FMR the permalloy magnetization precesses and the interfacial Co moments attempt to reorient so as to remain at 90° to the magnetization of the permalloy.

Figure 7.10 shows the dynamic XMCD signals obtained for Ni and XMLD for Co. Prior to measurement the system was field cooled to liquid nitrogen temperatures from 330 K with a 2 kOe field applied along the symmetry axis of the CPW. The Ni response (red curve) has the character of the imaginary component of the susceptibility. The Co data was obtained from the average of 10 scans and so shows reduced noise as compared to the Ni data, where only a single scan was recorded. There is a possible feature in the Co dynamic XMLD at about 0.015 T (150 Oe) but further measurements are required to confirm its existence and explore its character.

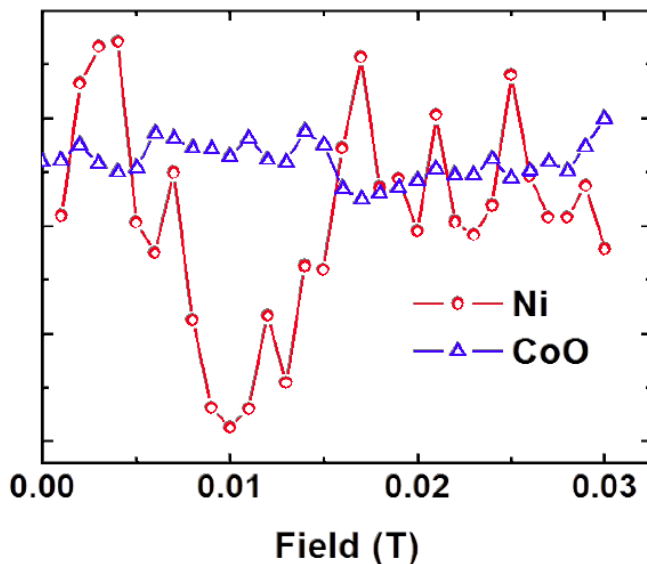


Figure 7.10. Field dependence of dynamic XMLD signals for Co and XMCD signal for Ni recorded at 6 GHz frequency. The dynamic XMLD measurement was made at the Co  $L_3$  edge using the same RF phase as used to record the Ni response. The CoO data represents an average of 10 scans and is therefore less noisy than the Ni data for which only a single scan was acquired.

#### 7.4 Conclusion

Time resolved magneto-optical Kerr effect and phase modulated X-ray ferromagnetic resonance measurements have been performed on the CoO/Py system for different values of temperature, RF frequency, and CoO thickness.

Kerr hysteresis loops did not yield any evidence of exchange bias for temperatures between 200 K and 330 K for any thickness of CoO. However increased coercivity was observed for increasing CoO thickness and decreasing temperature, suggesting the development of antiferromagnetic order within the CoO layer. The absence of exchange bias is attributed to the lack of an epitaxial relationship between the CoO and Py layers which leads to frustration of the AFM order upon field cooling. TRMOKE measurements of FMR show some features that have no clear symmetry with respect to the reversal of the bias field perhaps due mechanical changes in the electric contacts within the cryostat. The Kerr signals disappeared quickly as the temperature was decreased. A limited amount of XFMR data was obtained that confirmed the behaviour observed by TRMOKE. A preliminary measurement of dynamic XMLD establishes a method for studying the dynamics of the antiferromagnet at the AFM/FM interface.

## 7.5 Future works

The preliminary measurements made upon the CoO/Py system revealed two problems. Firstly, no macroscopic exchange bias was observed due to the lack of an epitaxial relationship between the Py and the CoO. Secondly, the signals obtained from the middle and thick end of the CoO wedge became very broad and noisy as the temperature was reduced. Therefore, the effect of inserting of a few monolayers of Fe between the CoO and Py, to obtain an epitaxial relationship between the FM and AFM, will be studied in future.

## Chapter 8 Conclusion

Time resolved scanning Kerr microscopy (TRSKM) has been used to study a number of different magnetic systems, including hard disk drive writer yokes, magnetic vortices arrays, coupled domain walls and AFM/FM systems.

In chapter 4, TRSKM was performed on different hard disk drive writer yokes designs. We have confirmed that the dynamic response of the writer is very sensitive to the driving conditions. For the same yoke stack structure and same driving frequency, flux beaming seems to occur only when the driving amplitude is not too large, in agreement with the previous study of Kasraj<sup>48</sup> et al. The SAF yoke design did not yield good writing dynamics, perhaps because the inter-layer exchange coupling cannot produce a simple antiferromagnetic alignment of layers within a very thick yoke. Since the driving conditions is one of the key factors which affects the writer dynamics, a systematic study of the driving condition within a particular writer design is necessary. The amplitude of the driving pulse should be varied while keeping the same repetition rate and pulse width, and the pulse width should be varied while keeping the amplitude and repetition rate constant. At the same time, higher pulse repetition rates should be considered since the driving frequency within a real hard drive is much higher than 1 MHz.

In chapter 5, we have demonstrated that TRSKM measurements of the polar Kerr effect can be used to detect vortex gyration, excited by a microwave waveform, in individual square nanomagnets with size smaller than the focused spot diameter. TRSKM images revealed differences in the phase of vortex gyration within individual elements of an array for which inter-element dipolar interactions are expected to be weak. These differences arise both from

variations in the gyration frequency of individual elements and also the different possible polarization and circulation of the vortex state. The distribution of equilibrium states within the elements may be influenced by structural imperfections, but thermal effects were also shown to play a role since different equilibriums states were obtained when the same field initialization process was repeated. TRSKM images of an array of closely spaced nanomagnets revealed regions of uniform contrast extending over lengths comparable to that of either one or two elements. Simulations showed that the spatial extent of regions of uniform contrast depends strongly on the equilibrium configuration, including the circulation and polarization within individual elements. For certain equilibrium configurations, dynamic simulations revealed splitting of the gyroscopic mode. The present work demonstrates the rich magnetization dynamics that may be achieved by controlling the circulation and polarization of vortices within an array of nanomagnets. More extensive micromagnetic simulations are required to understand the character of the collective gyroscopic modes that may occur. More experimental works on arrays with smaller dimensions are required as well to explore the interaction between the elements.

In chapter 6, we have used TRSKM to directly observe the presence of TDWs in a pair of curved NWs with HH and TT domain structure. From TR Kerr images the value of the static de-coupling field was estimated to be between 38 and 48 Oe in good agreement with a simple micromagnetic model and previous reports. While TRSKM was used to characterise the static de-coupling field in this work, dynamic coupling and microwave assisted de-coupling may be explored by using an in-plane RF magnetic field to couple to the NW resonances. This experimental approach may prove to be a powerful tool for the characterisation of interacting TDWs.

In chapter 7, time resolved magneto-optical Kerr effect and phase modulated X-ray ferromagnetic resonance measurements have been performed on the CoO/Py system for different values of temperature, RF frequency, and CoO thickness. Kerr hysteresis loops did not yield any evidence of exchange bias for temperatures between 200 K and 330 K for any thickness of CoO. However increased coercivity was observed for increasing CoO thickness and decreasing temperature, suggesting the development of antiferromagnetic order within the CoO layer. The absence of exchange bias is attributed to the lack of an epitaxial relationship between the CoO and Py layers which leads to frustration of the AFM order upon field cooling. TRMOKE measurements of FMR show some features that have no clear symmetry with respect to the reversal of the bias field perhaps due mechanical changes in the electric contacts within the cryostat. The Kerr signals disappeared quickly as the temperature was decreased. A limited amount of XFMR data was obtained that confirmed the behaviour observed by TRMOKE. A preliminary measurement of dynamic XMLD establishes a method for studying the dynamics of the antiferromagnet at the AFM/FM interface. The preliminary measurements made upon the CoO/Py system revealed two problems. Firstly, no macroscopic exchange bias was observed due to the lack of an epitaxial relationship between the Py and the CoO. Secondly, the signals obtained from the middle and thick end of the CoO wedge became very broad and noisy as the temperature was reduced. Therefore, the effect of inserting of a few monolayers of Fe between the CoO and Py, to obtain an epitaxial relationship between the FM and AFM, will be studied in future.

## Appendix 1 Bi-Polar electrical impulse generation

The bi-polar pulses used in the study presented in chapter 4 were generated by an assembly of two power dividers, a pulse polarity reverser and some carefully selected SMA cables. A sketch of the assembly is shown in Figure A1.1.

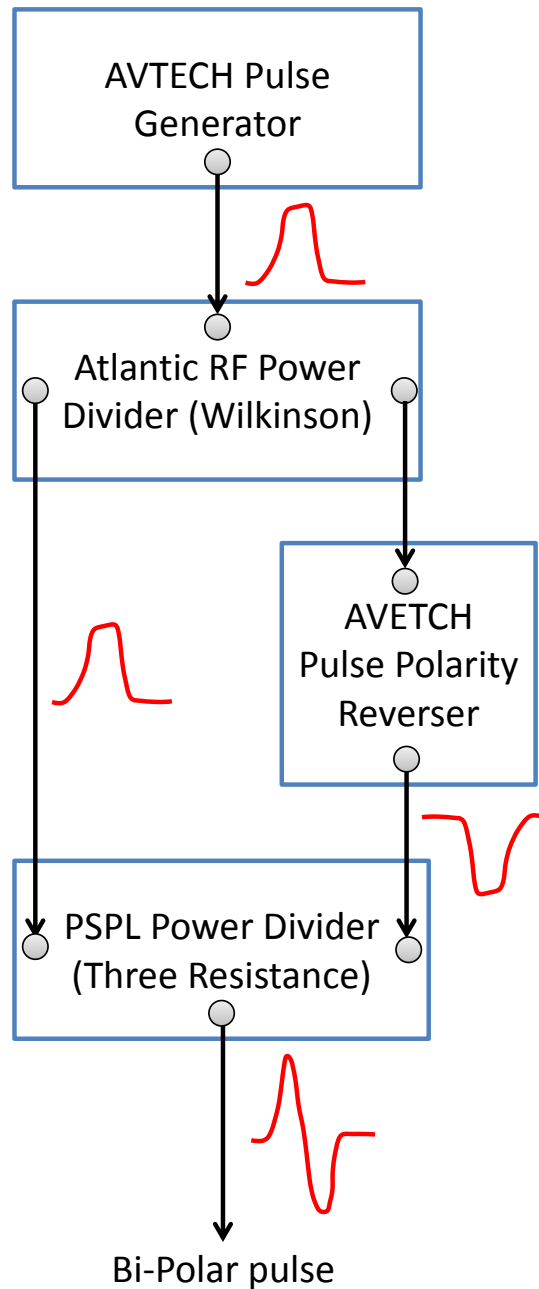


Figure A1.1 Sketch of the assembly used for bi-polar pulse generation, containing an Atlantic RF BPD-005020-2 power divider, an AVTECH AVX-2 pulse polarity reverse, and a PSPL 5333 power divider.

The components should be assembled in the following sequence:

1. Connect the AVTECH pulse generator to the Atlantic power divider (Wilkinson power divider<sup>116</sup>) and send the two output pulses into two channels of a sampling oscilloscope. Adjust the amplitudes of the pulses by adjusting the amplitude control of the AVETCH (the two channels should have the same amplitude).
- 2, Connect the AVTECH pulse polarity reverser to reverse the polarity of one of the pulses. If the connection is well impedance matched, two pulses should now have the same shape with only opposite polarity and slightly different amplitude due to the attenuation of the pulse reverser, as shown in Figure A1.2. Pulse 2 is the reversed pulse and therefore slightly lags pulse 1.

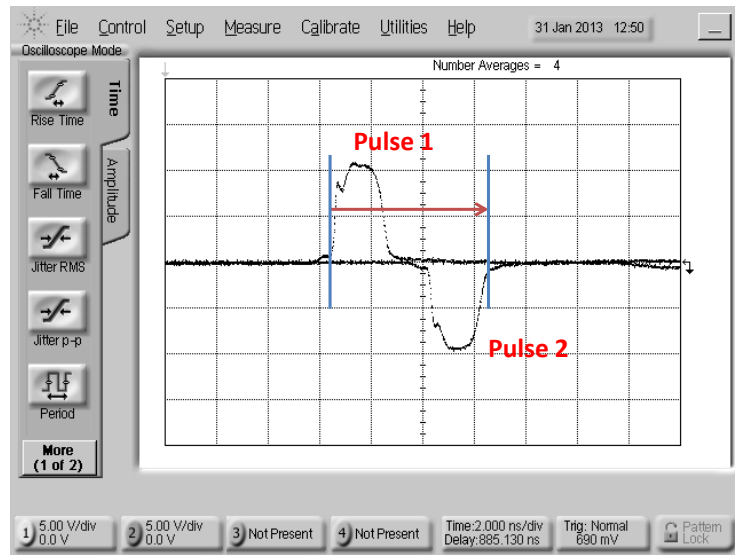


Figure A1.2 Oscilloscope screen shot of the two pulses with opposite polarity.

- 3, Add SMA cables of different length into the path of pulse 1 until it is delayed so as to rise at the second blue line shown in Figure A1.2.
- 4, Combine the two pulses using the PSPL power divider (three resistor power divider). Figure A1.3 shows the resulting bi-polar pulse recorded by the 50 GHz

sampling oscilloscope. It is recommended that the two pulses be viewed separately by removing the PSPL power divider before adjusting the pulse amplitude. The cable length should then be readjusted before re-combining the pulses. This is because the phase of rising edge of the pulse usually changes while adjusting the amplitude of the AVTECH output.

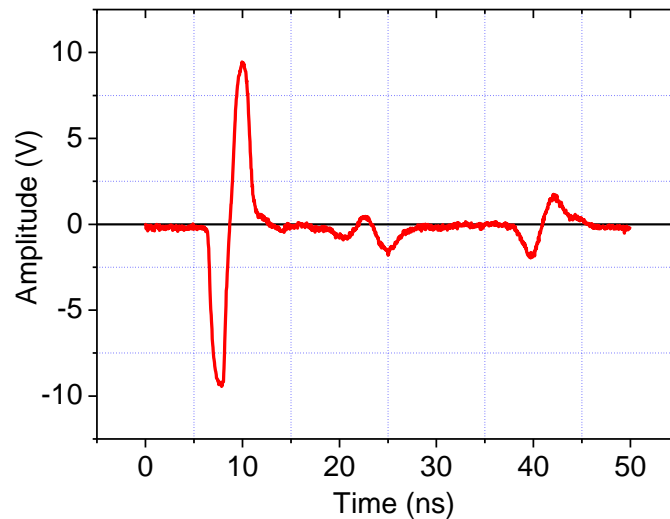


Figure A1.3 Bi-polar pulse recorded by a 50GHz sampling oscilloscope



## Reference

---

- <sup>1</sup> V. Poulsen, *method of recording and producing sounds or signals*, US Patent, No. 661619, (1900).
- <sup>2</sup> <http://www.seagate.com/about/newsroom/press-releases/HMR-demo-ceatec-2013-pr-master/>
- <sup>3</sup> D. A. Allwood, G. Xiong, M. D. Cooke, C. C. Faulkner, D. Atkinson, N. Vernier, R. P. Cowburn, "Submicrometer Ferromagnetic NOT Gate and Shift Register", *Science* **296**, 2003 (2002).
- <sup>4</sup> L. O'Brien, D. Petit, H. T. Zeng, E. R. Lewis, J. Sampaio, A. V. Jausovec, D. E. Read, and R. P. Cowburn, "Near-Field Interaction between Domain Walls in Adjacent Permalloy Nanowires", *Phys. Rev. Lett.* **103**, 077206 (2009).
- <sup>5</sup> M. Laufenberg, D. Bedau, H. Ehrke, M. Kläui, U. Rüdiger, D. Backes, L. J. Heyderman, F. Nolting, C. A. F. Vaz, J. A. C. Bland, T. Kasama, R. E. Dunin-Borkowski, S. Cherifi, A. Locatelli and S. Heun, "Quantitative determination of domain wall coupling energetics", *Appl. Phys. Lett.* **88**, 212510 (2006).
- <sup>6</sup> R. L. Stamps, A. S. Carricchio, and P. E. Wigen, "Domain-wall resonance in exchange-coupled magnetic films", *Phys. Rev. B* **55**, 6473 (1997).
- <sup>7</sup> C. Kittel, *Introduction to Solid State Physics*, 8th Edition, Chapter 11. Wiley (2005).
- <sup>8</sup> A.H. Morrish, "The Physical Principles of Magnetism, Chapter 2", John Wiley & Sons, New York (1965).
- <sup>9</sup> W. Heisenberg, "Zur Theorie des Ferromagnetismus", *Z. Physik* **49**, 619 (1928).
- <sup>10</sup> G. X. Miao, G. Xiao, A. Gupta, "Influence of substrate treatment on the growth morphology and magnetic anisotropy of epitaxial CrO<sub>2</sub> films", *Phys. Stat. Sol.* **203**, 1513(2006).

- 
- <sup>11</sup> H. Barkhausen, “Zwei mit Hilfe der neuen Verstärker entdeckte Erscheinungen”, Z. Phys. **20**, 401 (1919).
- <sup>12</sup> K. J. Sixtus, L. Tonks, “Propagation of Large Barkhausen Discontinuities”, Phys. Rev. **37**, 930 (1931).
- <sup>13</sup> F. Bloch, “Zur Theorie des Austauschproblems und der Remanenzerscheinung der Ferromagnetika”, Z. Phys. **74**, 295 (1932).
- <sup>14</sup> A. Hubert and R. Schäfer, “*Magnetic Domains—The Analysis of Magnetic Microstructures*, Chapter 1”, Springer, Berlin (2009).
- <sup>15</sup> P. S. Keatley, “Time-Resolved Magneto-Optical Investigations of Picosecond Magnetisation Dynamics in Arrays of Non-Ellipsoidal Ferromagnetic Nano-Elements”, PhD thesis, University of Exeter (2008).
- <sup>16</sup> E.E. Huber, Jr., D.O. Smith, J.B. Goodenough, “Domain Wall Structure in Permalloy Films”, J. Appl. Phys. **29**, 294 (1958).
- <sup>17</sup> K. Yamada, S. Kasai, Y. Nakatani, K. Kobayashi, H. Kohno, A. Thiaville and T. Ono, “Electrical switching of the vortex core in a magnetic disk”, Nat. Mat. **6**, 270 (2007).
- <sup>18</sup> S. C. Chae, Y. Horibe, D. Y. Jeong, S. Rodan, N. Lee, and S.-W. Cheong, “Self-organization, condensation, and annihilation of topological vortices and antivortices in a multiferroic”, Proc. Natl. Acad. Sci. USA **107**, 21366 (2010).
- <sup>19</sup> A. Wachowiak, J. Wiebe, M. Bode, O. Pietzsch, M. Morgenstern, and R. Wiesendanger, “Direct Observation of Internal Spin Structure of Magnetic Vortex Cores”, Science **298**, 577 (2002).
- <sup>20</sup> G. Beach, C. Nistor, C. Knutson, M. Tsoi and J. Erskine, “Dynamics of field-driven domain-wall propagation in ferromagnetic nanowires”, Nat. Mat. **4**, 741 (2005).

- 
- <sup>21</sup> G. Tatara and H. Kohno, "Theory of Current-Driven Domain Wall Motion: Spin Transfer versus Momentum Transfer", Phys. Rev. Lett. **92**, 086601 (2004).
- <sup>22</sup> H. Ohno, "Electric-field control of ferromagnetism", Nature **408**, 944 (2000).
- <sup>23</sup> L. Néel, "Magnetic properties of the manganese and chromium in solid solution range", J. Phys. Radium **3**, 160 (1932).
- <sup>24</sup> W. H. Meiklejohn and C. P Bean, "New Magnetic Anisotropy", Phys. Rev. **102**, 1413 (1956).
- <sup>25</sup> W. H. Meiklejohn and C. P Bean, "New Magnetic Anisotropy", Phys. Rev. **105**, 904 (1957).
- <sup>26</sup> J. Nogues and I. K. Schuller, "Exchange bias", J. Magn. Magn. Mater. **192**, 203 (1999).
- <sup>27</sup> T. L. Gilbert, "Largangian Formulation of The Gyromagnetic Equation of The Magnetization Field", Phys. Rev. **100**, 1243(1955).
- <sup>28</sup> F. Bloch, "Zur Theorie des Ferromagnetismus", Z. Physik **61**, 206 (1930).
- <sup>29</sup> T. G. Phillips, H. M. Rosenberg, "Spin waves in ferromagnets", Rep. Prog. Phys. **29**, 285 (1966).
- <sup>30</sup> J. Nemarich, "Contribution of the Two-Magnon Process to Magnetostatic-Mode Relaxation", Phys. Rev. Lett. **136**, A1657(1964).
- <sup>31</sup> C. Kittel, "On the Theory of Ferromagnetic Resonance Absorption", Phys. Rev. **73**, 155 (1948).
- <sup>32</sup> B. Hillebrands, K. Ounadjela, "Spin Damping in Ultrathin Magnetic Films in *Spin Dynamics in Confined Magnetic Structures II*", Springer, Berlin (2003).
- <sup>33</sup> M. Sparks, "Two-Magnon Processes in Ferromagnetic Relaxation", Phys. Rev. Lett. **8**, 54 (1962).

- 
- <sup>34</sup> M. Sparks, R. Loudon, C. Kittel, "Ferromagnetic Relaxation. I. Theory of the Relaxation of the Uniform Precession and the Degenerate Spectrum in Insulators at Low Temperatures", Phys. Rev. **122**, 791 (1961).
- <sup>35</sup> D. C. Ralph, M. D. Stiles, "Spin transfer torques", J. Magn. Magn. Mater. **320**, 1190 (2008).
- <sup>36</sup> J. C. Slonczewski, "Conductance and exchange coupling of two ferromagnets separated by a tunneling barrier", Phys. Rev. B **39**, 6995 (1989).
- <sup>37</sup> J. C. Slonczewski, "Current-driven excitation of magnetic multilayers", J. Magn. Magn. Mater. **159**, L1 (1996).
- <sup>38</sup> J. C. Slonczewski, "Excitation of spin waves by an electric current", J. Magn. Magn. Mater. **195**, L261 (1999).
- <sup>39</sup> Y. Tserkovnyak, A. Brataas and G. E. W. Bauer, "Enhanced Gilbert Damping in Thin Ferromagnetic Films", Phys. Rev. Lett. **88**, 117601 (2002).
- <sup>40</sup> M. K. Marcham, L. R. Shelford, S. A. Cavill, P. S. Keatley, W. Yu, P. Shafer, A. Neudert, J. R. Childress, J. A. Katine, E. Arenholz, N. D. Telling, G. van der Laan, and R. J. Hicken, "Phase-resolved x-ray ferromagnetic resonance measurements of spin pumping in spin valve structures", Phys. Rev. B **87**, 180403(R) (2013).
- <sup>41</sup> Z. Q. Qiu and S. D. Bader, "Surface magneto-optic Kerr effect", Rev. Sci. Instrum. **71**, 1243 (2000).
- <sup>42</sup> Z. Q. Qiu, S. D Bader, "Kerr Effect and Surface Magnetism in *Non-linear Opticals in Metals*", edited by K. H. Bennemann, Clarendon Press, Oxford (1998).
- <sup>43</sup> B. Heinrich, J.A.C.Bland(Eds), "*Ultrathin Magnetic Structure II, Chapter 4*", Springer-Verlag, Berlin Heidelberg, 1994.

- 
- <sup>44</sup> H. R. Hulme, “The Faraday Effect in Ferromagnetics”, Proc. R. Soc. London, Ser. A **135**, 237 (1932).
- <sup>45</sup> J. Wu, J.R. Moore and R.J. Hicken, “Optical pump-probe studies of the rise and damping of ferromagnetic resonance oscillations in a thin Fe film”, J. Magn. Magn. Mater. **222**, 189 (2000).
- <sup>46</sup> P. S. Keatley, V. V. Kruglyak, R. J. Hicken, J. R. Childress, “Acquisition of vector hysteresis loops from micro-arrays of nano-magnets”, J. A. Katine, J. Magn. Magn. Matter. **306**, 298 (2006).
- <sup>47</sup> P. M. W. French, “The generation of ultrashort laser pulses”, Rep. Prog. Phys. **58**, 169 (1995).
- <sup>48</sup> P. Kasiraj, R. M. Sheby, J. S. Best and D. E. Horne, “Magnetic domain imaging with a scanning Kerr effect microscope”, IEEE Trans. Magn. **22**, 837 (1986).
- <sup>49</sup> V. V. Kruglyak, A. Barman, R. J. Hicken, J. R. Childress, and J. A. Katine, “Picosecond magnetization dynamics in nanomagnets: Crossover to nonuniform precession”, Phys. Rev. B **71**, 220409(R) (2005).
- <sup>50</sup> M. K. Marcham, “Phase-Resolved Ferromagnetic Resonance Studies of Thin Film Ferromagnets”, PhD thesis, University of Exeter (2012).
- <sup>51</sup> J. Stohr and H. C. Siegmann, “*magnetism—from fundamentals to nanoscale dynamics*, Chapter 9”, Springer-Verlag, Berlin (2006).
- <sup>52</sup> S. I. Iwasaki, “Perpendicular magnetic recording”, IEEE Trans. Magn. **16**, 71 (1980).
- <sup>53</sup> S. Khizroev and D. Litvinov, “*Perpendicular Magnetic Recording*”, Kluwer Academic Publishers”, New York, 2004.
- <sup>54</sup> O. Heinonen, A. Nazarov and M. L. Plumer, “Dynamics of laminated write elements”, J. Appl. Phys. **99**, 08S302 (2006).

- 
- <sup>55</sup> P. Czoschke, S. Kaka, N. J. Gokemeijer and S. Franzen, “Real-time direct measurement of field rise time and dynamic instability of perpendicular writers”, *Appl. Phys. Lett.* **97**, 242504 (2010).
- <sup>56</sup> M. R. Freeman and J. F. Smyth, “Picosecond time resolved magnetization dynamics of thin film heads”, *J. Appl. Phys.* **79**, 5898 (1996).
- <sup>57</sup> A. Taratorin and K. Klaassen, “Media saturation and overwrite in perpendicular recording”, *IEEE Trans. Magn.* **42**, 157 (2006).
- <sup>58</sup> T. Arnoldusse, C. Vo, M. Burleson, and J.-G. Zhu, “A simple recording head write field rise time measurement”, *IEEE Trans. Magn.* **32**, 3521 (1996).
- <sup>59</sup> K. Klaassen and J. van Peppen, “Magnetic media switching dynamics in thermal equilibrium”, *IEEE Trans. Magn.* **37**, 1537 (2001).
- <sup>60</sup> X. Xing, A. Taratorin, and K. B. Klaassen, “Experimental Study of Perpendicular Write Head Field Rise Time”, *IEEE Trans. Magn.* **43**, 2181(2007).
- <sup>61</sup> Z. Li, D. Z. Bai, E. Lin and S. Mao, “Write field asymmetry in perpendicular magnetic recording”, *J. Appl. Phys.* **111**, 07B713(2012).
- <sup>62</sup> M. Mallary, “Conduction of flux at high frequencies in Permalloy strips by small angle rotations”, *J. Appl. Phys.* **57**, 3952 (1985).
- <sup>63</sup> M. R. Freeman, G. M. Steeves, G. E. Ballentine, and A. Krichevsky, “Noise imaging using magneto-optical sampling techniques (invited)”, *J. Appl. Phys.* **91**, 7326 (2002).
- <sup>64</sup> S. Sugimoto, Y. Fukuma, S. Kasai, T. Kimura, A. Barman and Y. C. Otani, “Dynamics of Coupled Vortices in a Pair of Ferromagnetic Disks”, *Phys. Rev. Lett.* **106**, 197203 (2011).
- <sup>65</sup> A. Vansteenkiste, K.W. Chou, M. Weigand, M. Curcic, V. Sackmann, H. Stoll, T. Tyliszczak, G. Woltersdorf, C. H. Back, G. Schütz and B. VanWaeyenberge,

---

“X-ray imaging of the dynamic magnetic vortex core deformation”, Nat. Phys. **5**, 332 (2009).

<sup>66</sup> S. A. Dzian, A. Yu. Galkin, B. A. Ivanov, V. E. Kireev, and V. M. Muravyov, “Vortex ground state for small arrays of magnetic particles with dipole coupling”, Phys. Rev. B **87**, 184404 (2013).

<sup>67</sup> K. Nakano, D. Chiba, N. Ohshima, S. Kasai, T. Sato, Y. Nakatani, K. Sekiguchi, K. Kobayashi, and T. Ono, “All-electrical operation of magnetic vortex core memory cell”, Appl. Phys. Lett. **99**, 262505 (2011).

<sup>68</sup> A. Dussaux, B. Georges, J. Grollier, V. Cros, A. V. Khvalkovskiy, A. Fukushima, M. Konoto, H. Kubota, K. Yakushiji, S. Yuasa, K. A. Zvezdin, K. Ando and A. Fert, “Large microwave generation from current-driven magnetic vortex oscillators in magnetic tunnel junctions”, Nat. Commun. **1**, 8 (2010).

<sup>69</sup> A. Ruotolo, V. Cros, B. Georges, A. Dussaux, J. Grollier, C. Deranlot, R. Guillemet, K. Bouzehouane, S. Fusil and A. Fert, “Phase-locking of magnetic vortices mediated by antivortices”, Nat. Nanotech. **4**, 528 (2009).

<sup>70</sup> A. Dussaux, A. V. Khvalkovskiy, J. Grollier, V. Cros, A. Fukushima, M. Konoto, H. Kubota, K. Yakushiji, S. Yuasa, K. Ando and A. Fert, “Phase locking of vortex based spin transfer oscillators to a microwave current”, Appl. Phys. Lett. **98**, 132506 (2011).

<sup>71</sup> S. Sugimoto, Y. Fukuma, S. Kasai, T. Kimura, A. Barman and Y. Otani, “Dynamics of Coupled Vortices in a Pair of Ferromagnetic Disks”, Phys. Rev. Lett. **106**, 197203 (2011).

<sup>72</sup> S. Jain, H. Schultheiss, O. Heinonen, F. Y. Fradin, J. E. Pearson, S. D. Bader, and V. Novosad, “Coupled vortex oscillations in mesoscale ferromagnetic double-disk structures”, Phys. Rev. B **86**, 214418 (2012).

- 
- <sup>73</sup> A. Vogel, T. Kamionka, M. Martens, A. Drews, K. W. Chou, T. Tyliszczak, H. Stoll, B. V. Waeyenberge, and G. Meier, “Coupled Vortex Oscillations in Spatially Separated Permalloy Squares”, Phys. Rev. Lett. **106**, 137201 (2011).
- <sup>74</sup> H. Jung, K.-S. Lee, D. Jeong, Y.-S. Choi, Y.-S. Yu, D.-S. Han, A. Voge, L. Bocklage, G. Meier, M.-Y. Im, P. Fischer and S.-K. Kim, “Tunable negligible-loss energy transfer between dipolar-coupled magnetic disks by stimulated vortex gyration”, Sci. Rep. **1**, 59 (2011).
- <sup>75</sup> B. Pigeau, C. Hahn, G. de Loubens, V.V. Naletov, and O. Klein, “Measurement of the Dynamical Dipolar Coupling in a Pair of Magnetic Nanodisks Using a Ferromagnetic Resonance Force Microscope”, Phys. Rev. Lett. **109**, 247602 (2012).
- <sup>76</sup> D. S. Han, A. Vogel, H. Jung, K.-S. Lee, M. Weigand, H. Stoll, G. Schutz, P. Fischer, G. Meier and S.-K. Kim, “Wave Modes of Collective Vortex Gyration in Dipolar-Coupled-Dot-Array Magnoic Crystals”, Sci. Rep. **3**, 2262 (2013)
- <sup>77</sup> A. Vogel, A. Drews, T. Kamionka, M. Bolte and G. Meier, “Influence of Dipolar Interaction on Vortex Dynamics in Arrays of Ferromagnetic Disks”, Phys. Rev. Lett. **105**, 037201 (2010).
- <sup>78</sup> B. Anjan, B. Saswati, T. Kimura, Y. Fukuma and Y. Otani, “Gyration mode splitting in magnetostatically coupled magnetic vortices in an array”, J. Phys. D: Appl. Phys. **43**, 422001 (2010).
- <sup>79</sup> P.S. Keatley, P. Gangmei, M. Dvornik, R.J. Hicken, J. Grollier, C. Ulysse, J.R. Childress, and J.A. Katine, Magnonics, edited by Sergej O. Demokritov and Andrei N. Slavin, “Bottom up Magnonics: Magnetization Dynamics of Individual Nanomagnets in Manonics”, Springer Berlin Heidelberg, 2013.

---

<sup>80</sup> X. Zhu, Z. Liu, V. Metlushko, P. Grütter and M. R. Freeman, "Broadband spin dynamics of the magnetic vortex state: Effect of the pulsed field direction", Phys. Rev. B **71**, 180408 (2005).

<sup>81</sup> The Object Oriented MicroMagnetic Framework (OOMMF):  
<http://math.nist.gov/oommf/>

<sup>82</sup> A. Vansteenkiste, J. De Baerdemaeker, K.W. Chou, H. Stoll, M. Curcic, T. Tyliszczak, G. Woltersdorf, C.H. Back, G. Schütz, and B. Van Waeyenberge, "Influence of domain wall pinning on the dynamic behavior of magnetic vortex structures: Time-resolved scanning x-ray transmission microscopy in NiFe thin film structures", Phys. Rev. B **77**, 144420 (2008).

<sup>83</sup> G. Gubbiotti, M. Madami, S. Tacchi, G. Carlotti, A. O. Adeyeye, S. Goolaup, N. Singh and A. N. Slavin, "Spin wave eigenmodes of square permalloy dots studied by Brillouin light scattering", J. Magn. Magn. Mater. **316**, e338 (2007).

<sup>84</sup> P. S. Keatley, V. V. Kruglyak, A. Neudert, E. A. Galaktionov, R. J. Hicken, J. R. Childress and J. A. Katine, "Time-resolved investigation of magnetization dynamics of arrays of nonellipsoidal nanomagnets with nonuniform ground states", Phys. Rev. B **78**, 214412 (2008).

<sup>85</sup> K.-S. Lee, S.-K. Kim, Y.-S. Yu, Y.-S. Choi, K. Y. Guslienko, H. Jung, and P. Fischer, "Universal Criterion and Phase Diagram for Switching a Magnetic Vortex Core in Soft Magnetic Nanodots", Phys. Rev. Lett. **101**, 267206 (2008).

<sup>86</sup> M. Curcic, B. V. Waeyenberge, A. Vansteenkiste, M. Weigand, V. Sackmann, H. Stoll, M. Fähnle, T. Tyliszczak, G. Woltersdorf, C. H. Back and Gisela Schütz, "Polarization Selective Magnetic Vortex Dynamics and Core Reversal in Rotating Magnetic Fields", Phys. Rev. Lett. **101**, 197204 (2008).

---

<sup>87</sup> J. Donahue and D. G. Porter, OOMMF User's Guide, Version 1.0, NISTIR 6376 (National Institute of Standards and Technology, Gaithersburg, MD, 1999); see <http://math.nist.gov/oommf>.

<sup>88</sup> O. V. Sukhostavets, J. M. Gonzalez and K. Y. Guslienko, "Magnetic Vortex Excitation Frequencies and Eigenmodes in a Pair of Coupled Circular Dots", *Appl. Phys. Expr.* **4**, 065003 (2011).

<sup>89</sup> P. Vavassori, D. Bisero, V. Bonanni, A. Busato, M. Grimsditch, K. M. Lebecki, V. Metlushko, and B. Ilic, "Magnetostatic dipolar domain-wall pinning in chains of permalloy triangular rings", *Phys. Rev. B* **78**, 174403 (2008).

<sup>90</sup> M. Hayashi, L. Thomas, Ya. B. Bazaliy, C. Rettner, R. Moriya, X. Jiang, and S. S. P. Parkin, "Influence of Current on Field-Driven Domain Wall Motion in Permalloy Nanowires from Time Resolved Measurements of Anisotropic Magnetoresistance", *Phys. Rev. Lett.* **96**, 197207 (2006).

<sup>91</sup> G. Tatara and H. Kohno, "Theory of Current-Driven Domain Wall Motion: Spin Transfer versus Momentum Transfer", *Phys. Rev. Lett.* **92**, 086601 (2004).

<sup>92</sup> M Kläui, "Head-to-head domain walls in magnetic nanostructures", *J. Phys.: Condens. Matter* **20**, 313001 (2008).

<sup>93</sup> V.V. Kruglyak, S.O. Demokritov, and D. Grundler, "Magnonics", *J. Phys. D-Appl. Phys.* **43**, 264001 (2010).

<sup>94</sup> S.O. Demokritov and A. Slavin, "Magnonics: From Fundamentals to Applications", Springer, Heidelberg, 2013.

<sup>95</sup> B. Pigeau, C. Hahn, G. de Loubens, V.V. Naletov, O. Klein, K. Mitsuzuka, D. Lacour, M. Hehn, S. Andrieu, and F. Montaigne, "Measurement of the Dynamical Dipolar Coupling in a Pair of Magnetic Nanodisks Using a

---

Ferromagnetic Resonance Force Microscope”, Phys. Rev. Lett. **109**, 247602 (2012).

<sup>96</sup> L. O’Brien, E.R. Lewis, A. Fernández-Pacheco, D. Petit, R.P. Cowburn, J. Sampaio, and D.E. Read, “Dynamic Oscillations of Coupled Domain Walls”, Phys. Rev. Lett. **108**, 187202 (2012).

<sup>97</sup> I. Purnama, M.C. Sekhar, S. Goolaup, and W.S. Lew, “Current-induced coupled domain wall motions in a two-nanowire system”, Appl. Phys. Lett. **99**, 152501 (2011).

<sup>98</sup> D.A. Allwood, G. Xiong, C.C. Faulkner, D. Atkinson, D. Petit, and R.P. Cowburn, “Magnetic Domain-Wall Logic”, Science **309**, 1688 (2005).

<sup>99</sup> S.S.P. Parkin, M. Hayashi, and L. Thomas, “Magnetic Domain-Wall Racetrack Logic”, Science **320**, 190 (2008).

<sup>100</sup> <http://math.nist.gov/oommf/>

<sup>101</sup> E. Saitoh, H. Miyajima, T. Yamaoka, and G. Tatara, “Current-induced resonance and mass determination of a single magnetic domain wall”, Nature **432**, 203 (2004).

<sup>102</sup> A. T. Galkiewicz, L. O’Brien, P. S. Keatley, R. P. Cowburn, and P. A. Crowell, “Resonance in magnetostatically coupled transverse domain walls ”, Phys. Rev. B **90**, 024420 (2014).

<sup>103</sup> L. O’Brien, D. Petit, H.T. Zeng, E.R. Lewis, J. Sampaio, A.V. Jausovec, D.E. Read, and R.P. Cowburn, “Near-Field Interaction between Domain Walls in Adjacent Permalloy Nanowires”, Phys. Rev. Lett. **103**, 077206 (2009).

<sup>104</sup> T. Miyazaki, and N. Tezuka, “Giant magnetic tunneling effect in Fe/Al<sub>2</sub>O<sub>3</sub>/Fe junction”, J. Magn. Magn. Mater. **139**, L231 (1995).

<sup>105</sup> J. Akerman, “Toward a Universal Memory”, Science **308**, 508 (2005).

- 
- <sup>106</sup> Y. Fan, K. J. Smith, G. Lupke<sup>1</sup>, A. T. Hanbicki, R. Goswami, C. H. Li, H. B. Zhao and B. T. Jonker, “Exchange bias of the interface spin system at the Fe/MgO interface”, Nat. Nanotech. **8**, 438 (2013).
- <sup>107</sup> A. E. Berkowitz and K. Takano, “Exchange anisotropy — a review”, J. Magn. Magn. Mater. **200**, 552 (1999).
- <sup>108</sup> H. Ohldag, A. Scholl, F. Nolting, E. Arenholz, S. Maat, A.T. Young, M. Carey, and J. Stohr, “Correlation between Exchange Bias and Pinned Interfacial Spins”, Phys. Rev. Lett. **91**, 017203 (2003).
- <sup>109</sup> J. Wu, J. S. Park, W. Kim, E. Arenholz, M. Liberati, A. Scholl, Y. Z. Wu, C. Hwang and Z. Q. Qiu, “Direct Measurement of Rotatable and Frozen CoO Spins in Exchange Bias System of CoO/Fe/Ag(001)”, Phys. Rev. Lett. **104**, 217204 (2010).
- <sup>110</sup> G. Ju, A. V. Nurmikko, R. F. C. Farrow, R. F. Marks, M. J. Carey and B. A. Gurney, “Ultrafast Time Resolved Photoinduced Magnetization Rotation in a Ferromagnetic/Antiferromagnetic Exchange Coupled System”, Phys. Rev. Lett. **82**, 3705 (1999).
- <sup>111</sup> Bijoy K. Kuanr, R. E. Camley, and Z. Celinski, “Exchange bias of NiO/NiFe: Linewidth broadening and anomalous spin-wave damping”, J. Appl. Phys. **93**, 7723 (2003).
- <sup>112</sup> J. McCord, R. Mattheis, D. Elefant, “Dynamic magnetic anisotropy at the onset of exchange bias:The NiFe/IrMn ferromagnet/antiferromagnet system”, Phys. Rev. B **70**, 094420 (2004).
- <sup>113</sup> R. D. McMichael, M. D. Stiles, P. J. Chen, and W. F. Egelhoff, Jr., “Ferromagnetic resonance studies of NiO-coupled thin films of Ni<sub>80</sub>Fe<sub>20</sub>”, Phys. Rev. B **58**, 8605 (1998).

---

<sup>114</sup> H. Wende and C. Antoniak, “Magnetism and Synchrotron Radiation, Chapter 5”, *Springer, 2010.*

<sup>115</sup> M. D. Stiles and R. D. McMichael, “Coercivity in exchange-bias bilayers”, *Phys. Rev. B* **63**, 064405 (2001).

<sup>116</sup> E.J. Wilkinson, “An N-way Power Divider”, *IEEE Trans. Microw. Theory Tech.* **8**, 116 (1960).